# 國 立 交 通 大 學

## 土 木 工 程 學 系

## 博 士 論 文

# 空載光達生產數值高程模型及其精度評估

# DTM Generation and Error Assessment for Airborne LIDAR Data

研 究 生：彭淼祥

指導教授：史天元 博士

中 華 民 國 九 十 四 年 十 二 月

# 空載光達生產數值高程模型及其精度評估

# DTM Generation and Error Assessment for Airborne LIDAR Data

研 究 生：彭淼祥　　Student: Miao-Hsiang Peng

指導教授：史天元 博士　　Advisor: Dr. Tian-Yuan Shih

國 立 交 通 大 學

土 木 工 程 學 系

博 士 論 文

A Dissertation
Submitted to Department of Civil Engineering
College of Engineering
National Chiao Tung University
in Partial Fulfillment of the Requirements
for the Degree of
Docotor of Philosophy
In
Civil Engineering

December 2005

Hsinchu, Taiwan, Republic of China

中 華 民 國 九 十 四 年 十 二 月

# 空載光達生產數值高程模型及其精度評估

研 究 生：彭淼祥　　指導教授：史天元 博士

國 立 交 通 大 學 土 木 工 程 學 系

## 摘 要

數值地形模型(Digital Terrain Model, DTM)在地理資訊系統應用與分析上是重要的數據，應用空載雷射掃描技術(或稱為空載光達，Airborne Light Detection and Ranging, LIDAR)測量地形的數值高程數據，其相關技術發展迅速，已經達到應用階段。空載雷射掃描儀量測地表的反射回訊，獲得三維座標的量測值，量測點包括了地形面以及非地面的量測點 (如建物、樹木，車輛)，為了生產DTM，地物的雷射量測點需進一步過濾或分類出來，留下地形面的雷射量測點，進而組成DTM。關於過濾非地面點的處理，此課題吸引了多方研究的投入，是重要的研究方向。本研究主要目的，發展出應用多重方式的過濾處理程序，並探討數據的精度評估。

關於濾除空載光達數據中非地面量測點之研究，目前成果指出，處理崎嶇的山區地形或高密度植被覆蓋的地區，仍是挑戰性的課題，諸多演算法為了過濾山區的植被量測點，將地形特徵如地形山脊亦同時被過度平滑濾除，此問題的主要原因是地物點與地面構成的坡度幾何和背景的陡坡地形坡度幾何，二者的可區分特性低，本研究提出自適性的過濾演算法，有效的移除背景陡坡地形所干擾的效應，處理特色在於過濾處理並且能保留地形的特徵。測試區域分別試驗於都市區域，複雜地類覆蓋與建物的濾除，以及山區植被的濾除，本研究比較不同的過濾方法，成果顯示本文的方法與商業軟體所使用的自動製程比較，在山區測試數

據組，本文過濾成果與檢核點比較，誤差絕對值的平均22.2 cm，優於自動化程序25.4 cm，本研究獲得良好的過濾成果。

本研究以山區測試區域(坡度平均26.6°)評估比較兩組光達數據組的特性，應用地面檢核點(906個檢核數據)分析數據精度，本文分析地形特徵包括地形坡度，坡向與土地覆蓋類型等因素對於光達高程精度的影響量。文中提出利用光達數據量化描述土地覆蓋類型的方法，包括植被體積量的估計，局部性地表粗糙度量測，到達地面的雷射測點平均相鄰點距離，以及植被覆蓋地平角度等評估指標，用以量化區別出不同的土地覆蓋類型。應用這些指標推導不同植被型態與光達高程數據的精度關係。分析成果顯示，光達數據高程精度與這幾個植被型態因子當中的「植被覆蓋地平角度」，「植被量的估計值」，「局部性地表粗糙度量測」，「到達地面的雷射測點平均相鄰點距離」等因子有相關聯性，高程精度隨者這四個因子的變化有統計顯著差異性。「植被覆蓋地平角度因子的三角正切值」與「到達地面的雷射測點平均相鄰點距離因子」兩個因子乘積，與高程精度具有高度的線性相關性(迴歸判定係數$r^2 > 0.9$)，高程精度隨不同植被覆蓋型態而變化。關於地形因子與光達數據高程精度的關係，高程精度隨地形坡度角的變化有統計顯著差異性。「坡度角的三角正切值」與「到達地面的雷射測點平均相鄰點距離」兩個因子乘積，與高程精度亦具有高度的線性相關性(迴歸判定係數$r^2 = 0.9$)，乘積的數值越大(地形越陡)，高程誤差越大。另外，有一組數據具有附加的交錯飛行掃描數據，以本文測試數據而言，交錯飛行，能降低坡向因子對於高程精度的影響量。

# DTM Generation and Error Assessment for Airborne LIDAR Data

Student: Miao-Hsiang Peng Advisor: Dr. Tian-Yuan Shih

Department of Civil Engineering
National Chiao Tung University

## ABSTRACT

Airborne light detection and ranging (LIDAR) technology has become a leading method for producing digital terrain models (DTMs) that are important to many GIS-related analyses and applications. In generating a digital terrain model, removing non-terrain measurements from LIDAR datasets has proven to be an important task. In this dissertation, a series of filters are developed to remove non-terrain LIDAR measurements.

It is difficult to accurately extract the terrain surface in areas of rugged relief or discontinuous topography. This research applies adaptive techniques to remove the effects of background relief. The terrain data are preserved, while non-terrain points are removed. The proposed method can discriminate effectively between terrain and non-terrain measurements, and has been tested for urban and mountainous areas. The filtered results from the proposed method are compared to traditional automatic techniques. The results indicate that the proposed method produces a better digital terrain model.

An accuracy assessment of two LIDAR-derived elevation datasets was conducted in areas of rugged terrain (average slope 26.6°). Data from 906 ground checkpoints in various land-cover types were collected in situ as reference points. Analysis of the accuracy of LIDAR-derived elevation as a function of several factors including terrain slope, terrain aspect, and land-cover types were conducted. This paper attempts to characterize vegetation information derived from LIDAR data based on variables such as canopy volume, local roughness of point clouds, point spacing of LIDAR ground returns, and vegetation angle. This information was used to evaluate the accuracy of elevation as a function of vegetation type. The experimental results revealed that the accuracy of elevation was considerably correlated with five factors: terrain slope, vegetation angle, canopy volume, local roughness of point clouds, and point spacing of LIDAR ground returns. The results show a linear relationship between the elevation accuracy and the combination of vegetation angle and the point spacing of ground returns ($r^2 > 0.9$). The combination of vegetation angle and point spacing of ground returns explains a significant amount of the variability in elevation accuracy. Elevation accuracy varied with different vegetation types. The elevation accuracy was also linearly correlated with the product of the point spacing of ground returns and the tangent of the slope ($r^2 = 0.9$). A greater product value implies a greater elevation error. In addition, with regard to terrain aspect, one dense dataset with extra cross-flight data revealed a lesser impact of aspect on elevation accuracy.

# TABLE OF CONTENTS

Abstract in Chinese ..... I

Abstract ..... III

TABLE OF CONTENTS ..... V

LIST OF TABLES ..... VII

LIST OF FIGURES ..... IX

LIST OF ACRONYMS ..... XII

CHAPTER ONE: INTRODUCTION ..... 1

1.1 Background ..... 1

1.2 Statement of the Problem ..... 3

1.3 Contributions ..... 5

1.4 Thesis Outline ..... 6

CHAPTER TWO: LITERATURE REVIEW ..... 7

2.1 Algorithms for DTM Generation ..... 7

2.2 Error Assessment for LIDAR-derived DTM ..... 10

CHAPTER THREE: DIGITAL TERRAIN MODEL GENERATION ..... 14

3.1 Terrain filtering concept ..... 14

3.2 Slope-based filter ..... 18

3.3 Directional steepest-descent filter ..... 21

3.4 Adaptive directional steepest-descent filter ..... 26

3.5 Adaptive directional elevation-difference filter ..... 27

3.6 Determination of search radius ..... 29

3.7 Filtering by multiple filtering procedures ..... 30

3.8 Algorithm implementation ..... 33

3.9 Test datasets ..... 35

3.10 Experiment and Evaluation ..... 45

CHAPTER FOUR: ERROR ASSESSMENT AND DTM VALIDATION ..... 63

4.1 Characterization of vegetation information ..... 63

4.2 Descriptions of land-cover types by vegetation information ..... 67

4.3 Analysis of point spacing of LIDAR ground returns ..... 76

4.4 Analysis of terrain slope ..... 76

4.5 Verifying the distribution of checkpoints ..... 77

4.6 Assessing errors using checkpoints ..... 78

4.7 Elevation error and vegetation type ..... 82

4.8 Elevation error and point spacing of LIDAR ground returns ..... 89

4.9 The combination effect of vegetation angle and point spacing ..... 91

4.10 Elevation error and terrain form ..... 93

4.11 Comparisons between photogrammetry and LIDAR ..... 99

CHAPTER FIVE: CONCLUSIONS AND RECOMMENDATIONS ..... 108

REFERENCES ..... 111

# LIST OF TABLES

Table 3.1 Statistics of terrain slopes of test site ..... 37

Table 3.2 LIDAR collection parameters of high relief site ..... 39

Table 3.3 Land-cover classes and their descriptions ..... 41

Table 3.4 The accuracy of multiple filtering results ..... 52

Table 3.5 Accuracy of DTM in bald earth areas (H = 1100 m, error in cm) ..... 57

Table 3.6 Accuracy of DTM in bald earth areas (H = 1800 m, error in cm) ..... 58

Table 3.7 Accuracy of DTM for automatic processing with manual edits (H = 1100 m, error in cm) ..... 59

Table 3.8 Accuracy of DTM for automatic processing (H = 1800 m, error in cm) .. 60

Table 3.9 Accuracy of DTM for multiple-filter processing (H=1100m, error in cm) ..... 61

Table 3.10 Accuracy of DTM for multiple-filter processing (H=1800m, error in cm) ..... 62

Table 4.1 Summary of 29 tree height measurements from field survey ..... 67

Table 4.2 Summary statistics of results for H = 1100 m dataset ..... 69

Table 4.3 Summary statistics of results for H = 1800 m dataset ..... 70

Table 4.4 Relationship between vegetation information for H = 1100 m dataset ..... 74

Table 4.5 Relationship between vegetation information for H = 1800 m dataset ..... 75

Table 4.6 Number of checkpoints by slope class and vegetation angle ..... 78

Table 4.7 Accuracy of terrain model for H = 1100 m dataset (error in cm) ..... 80

Table 4.8 Accuracy of terrain model for H = 1800 m dataset (error in cm) ..... 81

Table 4.9 Mean signed error ..... 82

Table 4.10 Checking the skewness ..... 82

Table 4.11 Elevation error by land-cover class (error in cm) ..... 83

Table 4.12 Elevation error related to vegetation type by reference canopy volume. 85

Table 4.13 The elevation error and local roughness on checkpoints ..... 87

Table 4.14 Relationship between elevation error and vegetation angle..... 88

Table 4.15 Regression of elevation error and vegetation angle ..... 88

Table 4.16 Elevation error and mean distance to the nearest LIDAR point ..... 90

Table 4.17 Regression of elevation error and mean distance to the nearest LIDAR point ..... 90

Table 4.18 Relationship between elevation error and the product of distance to nearest LIDAR point and the tangent of the elevation angle..... 92

Table 4.19 Regression of elevation error and the product of distance to nearest LIDAR point and the tangent of the elevation angle ..... 92

Table 4.20 Elevation error by reference slope..... 94

Table 4.21 Regression of elevation error and slope..... 94

Table 4.22 Relationship between elevation error and the product of the mean distance to the nearest LIDAR point and the tangent of the slope..... 96

Table 4.23 Regression of elevation error and the product of the mean distance to the nearest LIDAR point and the tangent of the slope..... 96

Table 4.24 Elevation error by aspect class ..... 98

Table 4.25 The differences of DSM in landslide rock (discrepancies between photogrammetry and LIDAR)..... 105

Table 4.26 The accuracy of DTM by manual measurement in stereo-mode environment ..... 106

Table 4.27 The accuracy of DTM using automated digital photogrammetry..... 106

# LIST OF FIGURES

Figure 3.1. An example of gentle terrain relief. ..... 16

Figure 3.2. The profile has gentle terrain relief. ..... 16

Figure 3.3. Filtering examples of global thresholding. ..... 16

Figure 3.4. Filtering by local thresholding technique. ..... 17

Figure 3.5. Filtering example of local thresholding. ..... 18

Figure 3.6. Steepest descent, defined as the minimum angle unobstructed. ..... 19

Figure 3.7. An example of large terrain relief ..... 20

Figure 3.8. Six results of slope-based filtering. ..... 21

Figure 3.9. Azimuth angle *D* is measured clockwise from north. ..... 23

Figure 3.10. Comparison between slope-based and directional steepest-descent filter. ..... 24

Figure 3.11. Comparison of profile between slope-based and directional steepest-descent filter. ..... 26

Figure 3.12. The steepest-descent is revised by removing the background slopes. ..... 27

Figure 3.13. Finding the lowest point progressively. ..... 28

Figure 3.14. Taking *p* as a center, relief spots are further selected and constitute set T. ..... 30

Figure 3.15. Flowchart of the multiple filtering algorithm. ..... 31

Figure 3.16. Sample profile. ..... 32

Figure 3.17. The elevation-differences values of the sample profile. ..... 33

Figure 3.18. The steepest-descent values of the sample profile ..... 33

Figure 3.19. High-relief site is located in central Taiwan affected by the Chi-Chi

Earthquake. .....38

Figure 3.20. Slopes distribution over the test site. .....38

Figure 3.21. Distribution of ground checkpoints in study area.....42

Figure 3.22. Field and aerial photos of the surveyed site. .....45

Figure 3.23. Effect of varying initial radius on errors, .....46

Figure 3.24. Effect of varying initial radius on errors, .....47

Figure 3.25. The DTM generation results for the urban area. .....50

Figure 3.26. The filtering errors for sample sites.....51

Figure 3.27. The comparisons of DTMs for H = 1100 m. .....56

Figure 3.28. The comparisons of DTMs for H = 1800 m. .....56

Figure 4.1. The greatest vegetation angle is defined as the maximum angle of the line-of-sight unobstructed to a specified distance *L*. .....66

Figure 4.2. Azimuth angle *D* is measured clockwise from north.....66

Figure 4.3. Comparison of shaded relief maps for tea farm A.....77

Figure 4.4. MAE error of both datasets, using various types of land-cover. .....84

Figure 4.5. Elevation error as a function of canopy volume.....85

Figure 4.6. Elevation error as a function of local roughness on checkpoints. .....87

Figure 4.7. Elevation error as a function of vegetation angle. .....89

Figure 4.8. Elevation error as a function of the mean distance.....91

Figure 4.9. Elevation error as a function of the product of the mean distance to nearest LIDAR point and the tangent of the vegetation angle. .....93

Figure 4.10. Elevation error as a function of slope.....95

Figure 4.11. Elevation error as a function of product of the mean distance to the nearest LIDAR point and the tangent of the slope.....97

Figure 4.12. Mean absolute error as a function of terrain aspect,.....99

Figure 4.13. Visual comparisons of shaded relief maps. .....102

Figure 4.14. The comparisons of contours.....103

Figure 4.15. The comparisons of DTMs from LIDAR-derived vs.

photogrammetry-derived.....107

# LIST OF ACRONYMS

| | |
|---|---|
| DEM | Digital Elevation Model |
| DSM | Digital Surface Model |
| DTM | Digital Terrain Model |
| FEMA | Federal Emergency and Management Agency |
| GIS | Geographic Information Systems |
| GPS | Global Positioning System |
| IDW | Inverse Distance Weighting |
| LIDAR | Light Detection And Ranging |
| MAE | Mean Absolute Error |
| RMSE | Root Mean Square Error |
| RTK | Real-Time-Kinematics |
| TIN | Triangulated Irregular Network |
| WGS84 | World Geodetic System of 1984 |

# CHAPTER ONE: INTRODUCTION

## 1.1 Background

Airborne LIght Detection And Ranging (LIDAR) is an active sensor that captures topographic data rapidly, economically and accurately. Consisting of a laser distance measurement, a scanning mirror, and an integrated GPS/INS system, airborne LIDAR has recently become a leading method for producing Digital Terrain Models (DTMs), (Ackermanm, 1999; Huising and Gomes Pereira, 1998; Kraus and Pfeifer, 1998; Baltsavias, 1999a; Wehr and Lohr, 1999; Maas, 2002).

Commercial LIDAR system designs have been based on the work done by NASA. Generally, there are two types of LIDAR systems: bathymetric systems work over water and topographic systems work over land. The wavelength for topographic LIDAR sensor is between 1.053 and 1.064 $\mu$m (the infrared portion of the spectrum), while airborne bathymetric LIDAR sensors use the blue/green portion of the spectrum. The pulse rates have increased with development of technology. The pulse rate, (measured in kilohertz, kHz) is the number of bursts of light per second; a 2 kHz system generates 2,000 pulses of laser energy in one second. Early systems offered pulse rates on 2 kHz to 7 kHz, while modern systems come with pulse rates of 25 kHz to 83 kHz. Higher pulse rates mean increased resolution. The spatial resolution varies depending on the pulse rate, flying altitude, and aircraft speed (Baltsavias, 1999b). Two distinct techniques of LIDAR have been developed: small footprint, time-of-flight laser altimetry and large footprint, waveform-digitizing techniques that analyze the full return waveform to capture a complete elevation profile within the target footprint (Flood, 2001). A typical laser beam used in a

small footprint LIDAR sensor has divergences of 0.2-to 0.33-mrad.

Airborne LIDAR can operate at night and is less affected by weather conditions than aerial photography, making it suitable for emergent mapping. The US Federal Emergency and Management Agency (FEMA) utilized airborne LIDAR to create digital terrain models for hydraulic modeling of floodplains, digital terrain maps, and other National Flood Insurance Program products for flood mitigation applications.

Most LIDAR sensors collect both range and intensity of the returned signal and information of multiple returns for each pulse. The multiple returns may be useful to categorize vegetation. Pfeifer *et al*. (2001) observed that 85% of the first and last pulses showed no difference in a sample case of building areas, whereas for the wooded areas only 20% of the two returns were identical. Some overviews of airborne LIDAR technology can be found (Maune, 2001; Baltsavias, 1999b; Hu, 2003; Wehr and Lohr, 1999).

The Netherlands is the first country to utilize airborne LIDAR to establish a nationwide digital elevation model with a density of 1 point per 16 $m^2$ (Huising and Gomes Pereira, 1998; Crombaghs *et al*., 2000). In addition to terrain mapping, airborne LIDAR can also be applied in the reconstruction of 3-D building models (Haala *et al*., 1998, 1999; Maas and Vosselman, 1999; Brenner, 2000; Vosselman and Dijkman, 2001). Hyyppä *et al*. (2001) reported on the use of small-footprint LIDAR in Finland to detect characteristics of individual trees such as their height, location, and crown dimensions. In the sparse boreal forest, where more than 30% of pulses reach the ground, a segmentation-based method retrieved stem volume estimates of the mean height, basal area, and stem volume with standard errors of 9.9%, 10.2%, and 10.5%, respectively. A few papers have used small-footprint LIDAR to infer vegetation characteristics and have achieved prediction of tree height and stem volume (Means *et al*., 2000; Næsset, 1997a; Næsset, 1997b).

Even though this technology is accepted as a tool for terrain mapping, the processing of LIDAR data is still in the situation of development. The two major problems of data processing are the elimination of systematic errors and the processing to remove non-terrain points from LIDAR datasets (Huising and Gomes Pereira, 1998). Determining whether a returned pulse is a terrain point or non-terrain cover is still an intense research topic. Most algorithms have difficulty accurately extracting the terrain surface, especially in areas of dense wooded cover, rugged relief or discontinuous topography.

## 1.2 Statement of the Problem

The most common use of LIDAR data is to generate DTMs, which are important for many GIS-related analysis and applications. To generate a DTM, the terrain points need to be identified, and the non-terrain points (trees, buildings, and vehicles, etc.) removed from the LIDAR measurements. Many algorithms have been developed to remove non-terrain points and generate DTMs (Kraus and Pfeifer, 1998; Pfeifer *et al*., 1999; Vosselman, 2000; Axelsson, 2000; Elmqvist, 2001; Briese *et al*., 2002; Brovelli *et al*., 2002; Wack and Wimmer, 2002; Hu, 2003; Zhang *et al*., 2003; Sithole and Vosselman, 2004). However, the filtering processing of LIDAR data is still in a phase of development.

There are two basic errors in filtering LIDAR measurements. A Type I error is one that removes bare-Earth points mistakenly; Type II errors involve accepting non-terrain points as terrain measurements. While filtering processing, a trade-off is involved between making Type I and Type II errors. Variety of terrain type and land-cover type may influence the performance of filtering algorithms (Sithole, 2001; Sithole and Vosselman, 2003). Determining filtering parameters in terms of terrain

information is somewhat subjective. The choice of proper parameters may be problematic. It is difficult to detect all non-terrain objects of various sizes using a fixed parameter.

The focus of this research is on developing and implementing algorithms for automatic extraction of topographic surface. The robustness of performance and feature preservation of filtering result are emphasized.

Though a general understanding of the accuracy of LIDAR is known, too few empirical studies exist for assessing the accuracy of DTMs derived from LIDAR data. Gomes Pereira and Janssen (1999) used a low-flight-altitude (240 m) dataset to evaluate LIDAR-derived Digital Elevation Models (DEMs) and found that root-mean-square error (RMSE) varied from 8 to 15 cm in flat regions, and from 25 to 35 cm in sloped terrain. Typical elevation accuracies of LIDAR-derived DEMs have 15 cm RMSE over non-forested flat surfaces (Hodgson and Bresnahan, 2004). Hodgson *et al*. (2003) showed that land-cover types and terrain slope substantially affected the elevation accuracy determined from leaf-on LIDAR data in North Carolina. Accordingly, evaluating LIDAR accuracy based on both land-cover types and terrain characteristics is necessary.

The vegetation types for collecting reference points are commonly divided into basic land-cover categories such as tall weeds, brush/low trees, and forests. Raber *et al*. (2002) developed an adaptive LIDAR vegetation point removal process. They used an algorithm adaptively adjusting the parameters based on a vegetation map.

There is a need for research efforts in quantifying the accuracy of LIDAR data collected under various collection parameters, filtering processes, and geography conditions. This study evaluated a method to identify vegetation characteristics based on LIDAR data. The derived vegetation information was factored into the evaluation of the impact of vegetation types on the accuracy of LIDAR-derived

elevation. This research considers some quantitative descriptors such as vegetation angle, canopy volumes and LIDAR-derived tree height, to characterize the relationship between elevation accuracy and the types of vegetation. One distinctive aspect of this study is its use of LIDAR data points to derive information about vegetation types in terms of descriptors.

## 1.3 Contributions

The following novel contributions were developed to achieve the research objectives:

* This research developed a multiple-filtering framework to remove non-terrain LIDAR measurements to generate DTMs. An adaptive directional steepest-descent filter is proposed. The proposed algorithm is suited to efficiently separate terrain and non-terrain LIDAR data in both urban and mountain areas. This work also proposed an adaptive directional elevation-difference filter to remove large objects such as very large buildings. The selections of the filtering parameters are very important. The proposed multiple-filtering framework is highly automatic to adaptively adjust the parameters.
* The research proposed to characterize vegetation information derived from LIDAR data base on variables such as canopy volume, local roughness of point clouds, point spacing of LIDAR ground returns, and vegetation angle. This information was used to evaluate the accuracy of elevation as a function of vegetation type. Two sets of LIDAR-derived elevation were used to evaluate the impact of terrain slope, terrain aspect, and land-cover type on elevation accuracy.

The framework of accuracy assessment is also presented.

## 1.4 Thesis Outline

In Chapter 2, a literature review on related filtering processes and quality assessment is reported. Chapter 3 describes the development of a multiple-filtering procedure for DTM generation. In Chapter 4, the error factors of the DTM are discussed. Conclusions are presented in Chapter 5, followed by suggestions for future research.

# CHAPTER TWO: LITERATURE REVIEW

## 2.1 Algorithms for DTM Generation

LIDAR acquires a three-dimensional cloud of points with irregular sampling. The measurements hit on objects such as buildings, vehicles, vegetation, and bald terrain. To generate a DTM, the core task involves the separation of non-terrain points from LIDAR datasets. This task is referred to as filtering, classification, non-ground measurements removal. The filtering task dominates the topic of DTM generation. A number of algorithms have been reported in the literature, but there are a number of conditions that make filtering a very difficult problem. DTM generation from LIDAR data has proven to be a challenging task.

Kraus and Pfeifer (1998, 2001) utilized linear least squares interpolation iteratively to remove tree measurements and generate DTMs in forest areas. The least squares interpolation is based mainly on calculating the residuals, i.e., the distance from the surface to the measurement points. It is assumed that terrain points are likely to have negative residuals, whereas non-terrain points are more likely to have positive residuals. These residuals are used to compute weights. Points with large negative residuals have maximal weights and they attract the surface. Similar methods have been adopted by Lohmann *et al*. (2000). Pfeifer *et al*. (2001) extended this method by a hierarchical strategy to assemble data from coarse to fine. Lee and Younan (2003) used a modified linear prediction technique, followed by adaptive processing and refinement. However, this method fails to model terrain with steep slopes and large variability. In addition, extreme low points can be easily misclassified as terrain points as a result of the negative errors.

Kilian *et al*. (1996) used morphological filters to eliminate non-terrain points. Typically these filters need to predefine a search window size. These filters may have problems with dense forest canopy or large buildings. If a small window size is used, large-sized buildings cannot be removed. On the other hand, larger window size causes the filter to over-remove terrain points or chop off hills. Kilian *et al*. (1996) suggested using a series of windows to progressively filter the terrain.

Petzold *et al*. (1999) proposed a filtering algorithm. A rough terrain model is calculated by the lowest points found in a moving window of a rather large size. All points with a height difference exceeding a given threshold are filtered out, and a more precise DTM is calculated. This step is repeated several times by reducing the window size. The final window size and the final threshold have great influence on the results: small window size leads to points on large buildings remaining, while a high threshold in the final step leads to non-terrain points being classified as terrain points. Therefore, the parameters depend on the terrain variation and have to be adjusted for flat, hilly and mountainous regions.

The concept of resizing window size was adopted by Zhang *et al*. (2003, 2005); they proposed a progressive morphological filter. By gradually increasing the window size of the filter and using elevation difference thresholds, the non-terrain points are removed, while terrain points are preserved.

Lohmann *et al*. (2000) compared two algorithms, namely the use of linear prediction and the use of dual rank filters. The use of linear prediction showed satisfactory results in forest areas, whereas areas with steep terrain showed problems. The linear prediction filter needs to be improved by being locally adapted to the shape of the terrain (Lee and Younan, 2003). The dual rank filter is a mathematical morphology filter which is applied to a grayscale image. Dual rank filters need to be improved through interactive control and some pre-knowledge to properly set the

necessary parameters.

Vosselman (2000) proposed a slope-based filter. This method was commonly applied for DTM generation from LIDAR data. A measurement is classified as a terrain point if the height differences of this measurement point and any other point within a given circle are smaller than a predefined threshold. Choosing a threshold of too small height results in removing some detail of the terrain or cutting hill peaks; too large a threshold results in preservation of non-terrain points. Furthermore, the fixed threshold procedure limits the use of slope-based filter to terrain with gentle slopes. This technique will give satisfactory results only when non-ground objects (trees, buildings, etc.) and background terrain slopes are distinct and are uniform throughout the full coverage.

The next parameter of the filter is the radius of search region. The region size should be large enough to enclose the larger non-ground objects, such as buildings, but not so large as to cover different terrain aspects (i.e., ridges should not be crossed). Small search regions tend to cover uniform background slopes. Large regions tend to have larger topographical undulations than smaller regions. Adaptive techniques are required to overcome the effects of nonuniformities in background slopes. Slope-based filter has been shown to be equivalent to the erosion operator in morphology. Sithole (2001) has attempted to improve this filter.

Axelsson (1999, 2000) described an adaptive TIN (Triangulated Irregular Network) model to process ground points in dense urban areas where discontinuities may occur. A course TIN is formed based on seed points selected from low points. The course TIN iteratively adds more points if their parameters are below threshold values. The problem with adaptive TIN is that it is difficult to detect various sizes of non-ground objects by using a fixed parameter. Raber *et al*. (2002) showed an adaptive vegetation removal process. The different thresholds were adaptively given

based on a vegetation map for various land cover types.

## 2.2 Error Assessment for LIDAR-derived DTM

The elevation accuracy of LIDAR-derived DTM is routinely quoted as 15 cm. The quality of the final DTMs was influenced by the following components:

* elevation error from the system measurement,
* horizontal error from the system measurement,
* misclassification of terrain points as non-terrain points,
* misclassification of non-terrain points as terrain points, and
* interpolation error introduced into DTM derived from clouds of points.

### 1. Sources of X-Y-Z error

The sources of positional (X-Y-Z) error in the collection processing can be grouped according to (1) the laser instrument, INS and GPS, (2) the process of measuring from the air, and (3) the target surface causing measurement to be influenced by the type of ground coverage and the terrain slope. A discussion of sources of systematic and random errors can be found in Huising and Gomes Pereira (1998).

Factors that affect the accuracy of LIDAR measurements include the following: (1) instrument-related factors such as the measurement accuracy of the laser range finder, the GPS receiver, the INS and the scanner (Wehr and Lohr, 1999); (2) calibration errors caused by misalignment between instrument components; (3) data collection parameters, such as the flying height and the width of the field of view of the scanner, which can both be reduced to improve the accuracy of LIDAR measurements (Baltsavias, 1999b); (4) GPS data quality, such as GPS PDOP value,

satellite phase RMSE and the base station distance separation, and (5) atmospheric refraction error.

## 2. Mapping sources error

A characteristic of elevation error for terrain mapping is the relationship with terrain slope (Hodgson and Bresnahan, 2004). Typically, planimetric accuracy is lower than height accuracy of LIDAR measurement. A horizontal error on a flat surface will have no influence on vertical errors, while for inclined slopes the horizontal error in the observation may introduce extra error in the elevation value. The amount of elevation error introduced is a function of terrain slope (Hodgson and Bresnahan, 2004):

$$\text{Elevation Error} = \tan(\text{slope}) \times \text{Horizontal error} \qquad (2.1)$$

## 3. LIDAR point classification error

Sithole and Vosselman (2003) evaluated the performance of eight filtering algorithms. Twelve datasets were processed to test these filters, and it was found that all the filters performed well in smooth rural landscape. However, complex urban areas and rough terrain with vegetation still pose challenges to automating the process of generating DTMs.

Pfeifer *et al*. (2001) presented an iterative robust filtering approach (using linear prediction based on the software SCOP++). With the OEEPE test data sets the suitability of the algorithm demonstrated the vertical accuracies of three areas in RMSE of 11 cm and one area in RMSE of 48 cm.

Raber *et al*. (2002) conducted an adaptive technique to create DTMs through LIDAR-derived vegetation type information. The adaptive technique creates a superior DTM compared to DTMs created by automatic processes. They

demonstrated the vertical accuracies of using the adaptive optimized method in RMSE of 29 cm and using automatic with human edits in RMSE of 45 cm.

## 4. Interpolation Error

Interpolation error is semi-systematic. It is related to the density of mass points, the use of extra data such as breaklines, the use of data structure, and interpolation techniques. Point spacing between LIDAR returns is the result of collection parameters, including (1) flying altitude and speed of the aircraft, (2) the pulse rate, and (3) the scan angle. Lloyd and Atkinson (2002) compared the Inverse Distance Weighting and kriging interpolation techniques. They showed that the advantages of kriging with a trend model were more accurate when the number of data points decreases. It should be noted that the significant differences between varies of the interpolation of gridded DTMs were suspected because standard deviation in elevation error ranged from only 10.9 cm to 12.8 cm (decrease less than 2 cm) in their study. The interpolation methods of Inverse Distance Weighting and kriging can be found in Peng and Shih (2002). Smith *et al*., (2004) showed that the increase in errors at rough resolutions (4 m grid comparison on a 1 m grid) were of the order of 50–80 cm. These two studies did not reveal the interaction impact of terrain slope and the density of mass points on the accuracy of LIDAR-derived elevation. Hu (2003) used a variety of data structures to compose DTMs resulting in non-significant differences in quality. Hodgson and Bresnahan (2004) also found that additional error introduced by interpolation is low and does not have a major impact on the total error budget (adding up to 3.3 cm to any land-cover class).

## 5. Quality Control Checkpoints

FEMA provides guidelines for the selection, survey and documentation of

checkpoints. At lease 20 three-dimensional QC checkpoints are collected in each of five land-cover categories. The examples of land-cover categories: (1) grass (sand, rock, lawns, golf courses), (2) weeds and crops, (3) scrub (brush land and low trees), (4) forest, (5) built-up areas with dense man-made structures.

## 6. Empirical Study of LIDAR Error

Kraus and Pfeifer (1998) assess a dataset collected at 1000 m flying altitude. In flat terrain, comparing 466 ground checkpoints with LIDAR data showed that the RMSE was 25 cm. After further improvements in the data processing, an accuracy of 10 cm was achieved.

Ahokas *et al.* (2003) evaluated height errors of LIDAR datasets collected at different flying altitudes, and found that the higher the flying altitude, the larger the height error. For asphalt surfaces a standard deviation of 10 cm is obtainable from H = 550 m.

Hodgson *et al*. (2003) reported accuracy from 3.4-m post spacing dataset collected in leaf-on conditions. This study found an elevation error of 33 cm in low grass and 153 cm in scrub. Errors in low grass and high grass were much smaller than those in heavily vegetated canopies.

The comparisons between LIDAR and photogrammetry can be found in Baltsavias (1999c); Kraus and Pfeifer (1998); Adams and Chandler (2002). Other studies regarding estimating relative LIDAR accuracy by comparing overlapping datasets include Behan (2000), Burman (2000), Vosselman and Maas (2001), Latypov (2002), Maas (2002), and Crombaghs *et al*. (2000, 2002), Liu (2005).

# CHAPTER THREE: DIGITAL TERRAIN MODEL GENERATION

To generate a digital terrain model of the bare Earth, the non-terrain points must be filtered out from LIDAR datasets, a process sometimes referred as vegetation removal, classification, filtering, or DTM generation. It is difficult to extract the terrain surface completely with complex land-cover solely using a single algorithm. The multiple-filtering approaches developed for DTM generation are described below. The quality assessment of the filtering results for several datasets was conducted.

## 3.1 Terrain filtering concept

In order to eliminate non-terrain points, every filter needs to make an assumption to mathematically define what a terrain point is. I developed algorithms to analyze the geometric characteristics, such as slopes and differences, of a point relative to its neighboring points. The concepts adopted in this research include the following:

* The lowest point is more likely to be a ground measurement. The lower the point, the larger probability to be a terrain point (Petzold et al., 1999; Axelsson, 2000).
* Variation of the slope at the edge of non-terrain objects is significant than terrain points of flat ground (Vosselman ,2000; Sithole, 2001).
* Since terrain points have lower elevations than non-terrain points, it is able to separate terrain points with other objects by using elevation differences.

Local lower points are usually the candidate terrain points, and local higher points are likely building roof or tree points. This idea was commonly applied for filtering algorithm. Petzold *et al*. (1999) proposed a filtering algorithm based on finding local low points in moving filtering windows of varying sizes. Kraus and Pfeifer (1998) developed algorithm based on the linear prediction. Low points have maximal weights and they attract the prediction surface. High points with minimal weights are eliminated. Another commonly used algorithm to find minimum values is a mathematical morphology filter which is applied to a raster image.

Figure 3.1 and 3.2 show a cross section of LIDAR points. The dashed line in Figure 3.2 indicates the elevation of the threshold. High points should be filtered and low points should be kept. Thresholding is a synonymous term for filtering. The most important task in performing filtering is the choice of an appropriate threshold level. I distinguish two approaches of thresholding techniques. Global thresholding use the fixed threshold value. Local thresholding examine relationships between elevations of neighboring points to adapt the threshold according to the terrain variation for different terrain regions. The approach of fixed global thresholding may be satisfactory when the elevation has relatively gentle variations throughout the full coverage. Figure 3.3 (a) and (b) show examples of the results of poorly chosen thresholds. In Figure 3.3 (a), the elevation threshold is chosen too high, resulting in some non-terrain points such as trees remaining. In Figure 3.3 (b), the elevation threshold is chosen too low, resulting in some terrain details unwanted filtered.

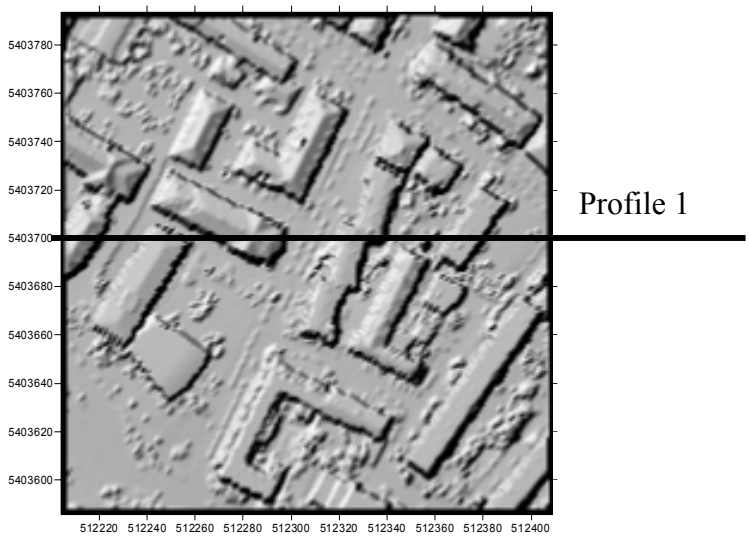


Figure 3.1. An example of gentle terrain relief.

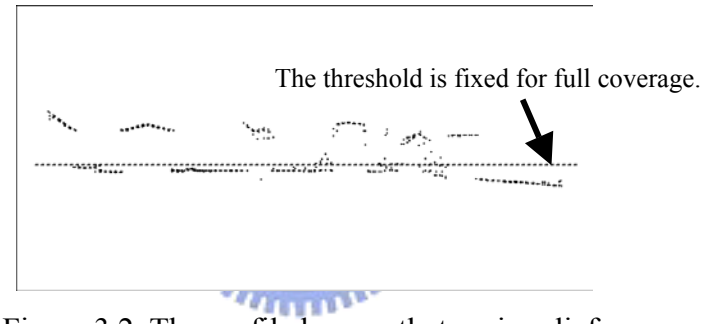


Figure 3.2. The profile has gentle terrain relief.

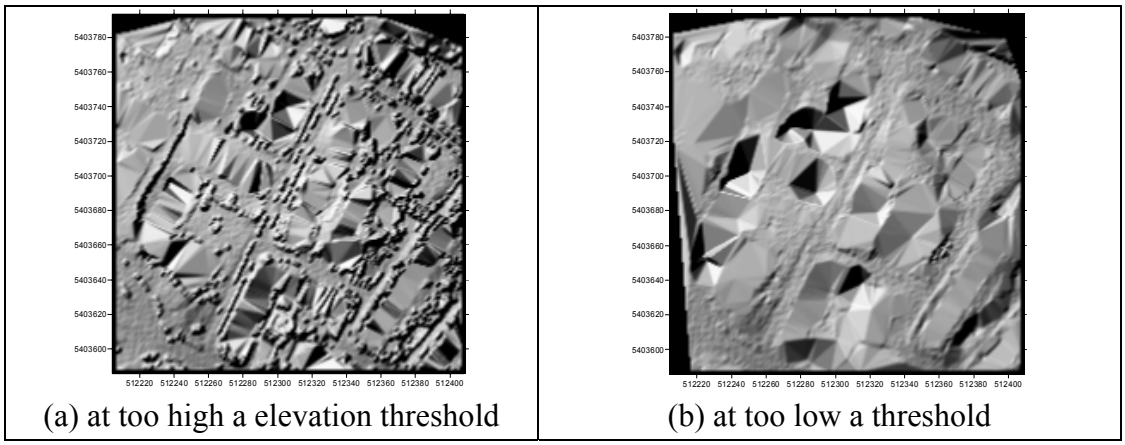


Figure 3.3. Filtering examples of global thresholding.

One approach to local thresholding is to subtract a local trend surface from the original elevation data. We may implement this by using erosion operation of morphological processing to calculate a moving region minimum. For a LIDAR measurement $p(x,y,z)$, the erosion of elevation z at x and y is defined as

$$e_p = \min_{(x_p,y_p)\in w} (z_p). \tag{3.1}$$

The erosion output $e_p$ is the minimum elevation value in the neighborhood of point $p$. By comparing each elevation value to its eroded trend surface, remove non-terrain objects if it is much above (or above a given threshold such as 0.3 m) the eroded surface.

Figure 3.4 shows the eroded surface by applying an erosion operation with a window size of 10 m. The windows size in erosion operation should be large enough to enclose an object such as a large building completely. Note large building objects large than the window size are remained by erosion (Figure 3.5). This choice of proper size for the window may be problematic when coverage contains large buildings of variable size.

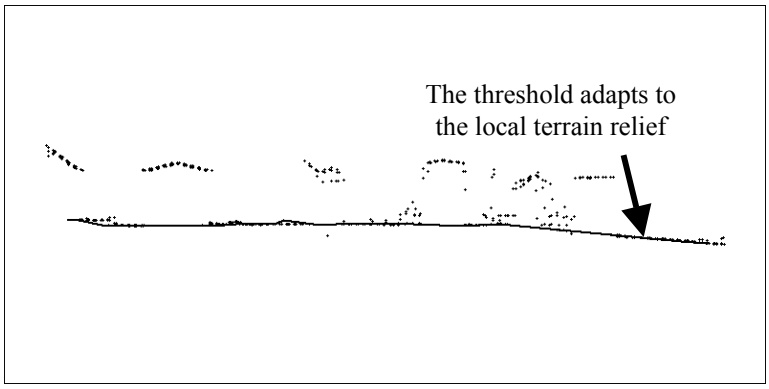


Figure 3.4. Filtering by local thresholding technique.

The eroded trend surface was calculated from a moving window minimum. The window size is set to 10 meters.

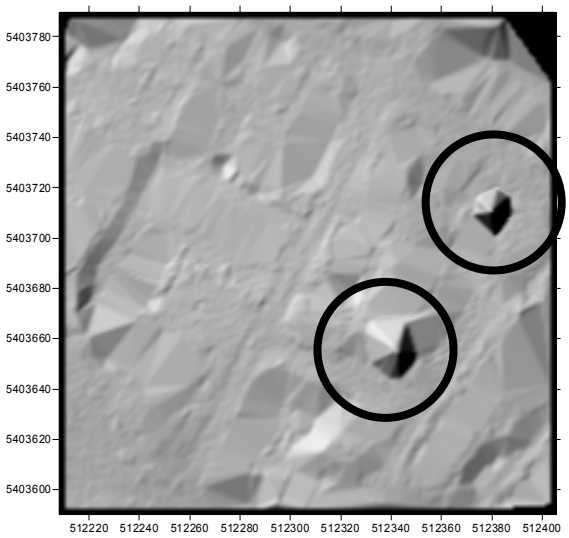


Figure 3.5. Filtering example of local thresholding.

The window size must be set with respect to the objects size: otherwise, large building objects large than the window size are remained.

The variety of landscapes to be performed filtering requires different approaches. There is not a single optimal method of filtering for all conditions till today. I developed a series of filtering techniques: (1) Directional steepest-descent filter examine the steepest slope in the different directions to counter the directional effects and improve the slope-based filter; (2) Adaptive techniques examine relationships between slopes (or height differences) of neighboring points to adapt the threshold according to the examined slopes (or height differences) statistics; (3) Automatically determination of search size, it may match for different terrain.

## 3.2 Slope-based filter

Slope change and elevation difference are frequently used to characterize

non-ground objects. Assuming that the slope in natural terrain should change gradually. Whereas on the edge of non-ground objects, the slopes and elevation differences between the ground and non-ground points should be larger than those between ground points.

A measurement is classified as a terrain point if the steepest slope of this measurement point and any other point within a given circle are smaller than a predefined threshold. In words: a point $p$ is classified as a terrain point if there is no other point $i$ such that the slope between these points is larger than the allowed maximum slope (Figure 3.6). To find the steepest slope by a search distance from the measurement point $p$ is in the form

$$Slope_p = \max_{i=1\sim n} \left\{ \frac{z_p - z_i}{\sqrt{(x_p - x_i)^2 + (y_p - y_i)^2}} \right\} \tag{3.2}$$

where points $(x_i,y_i,z_i)$ represent point $p$'s neighbors within a radial distance $L$ of a given circle, and $n$ is the total number of $p$'s neighbors.

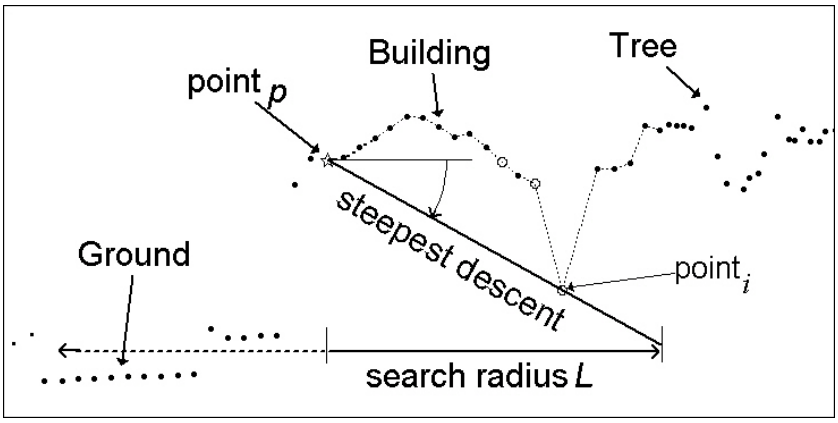


Figure 3.6. Steepest descent, defined as the minimum angle unobstructed.

The selection of the searching window size $L$ is important when using this filter. If a small window size is used, large-sized buildings cannot be removed. On the

other hand, larger window size causes the filter to over-remove terrain points or chop off hills. Figure 3.7 shows an example of large terrain relief. Figure 3.8 shows the results of slope-based filtering for six cases, and their parameters including search window and slope threshold. The larger search windows the terrain feature is more eroded.

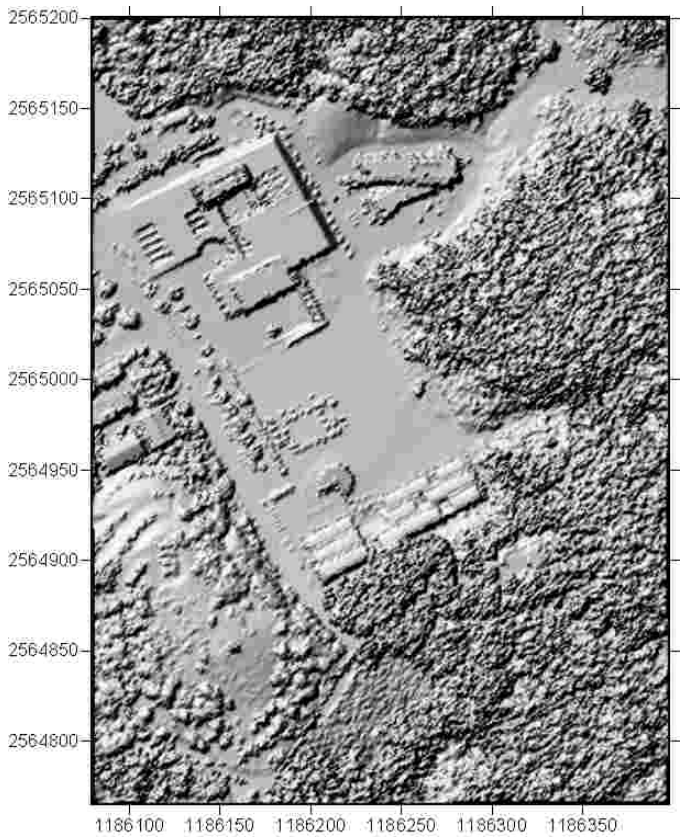


Figure 3.7. An example of large terrain relief

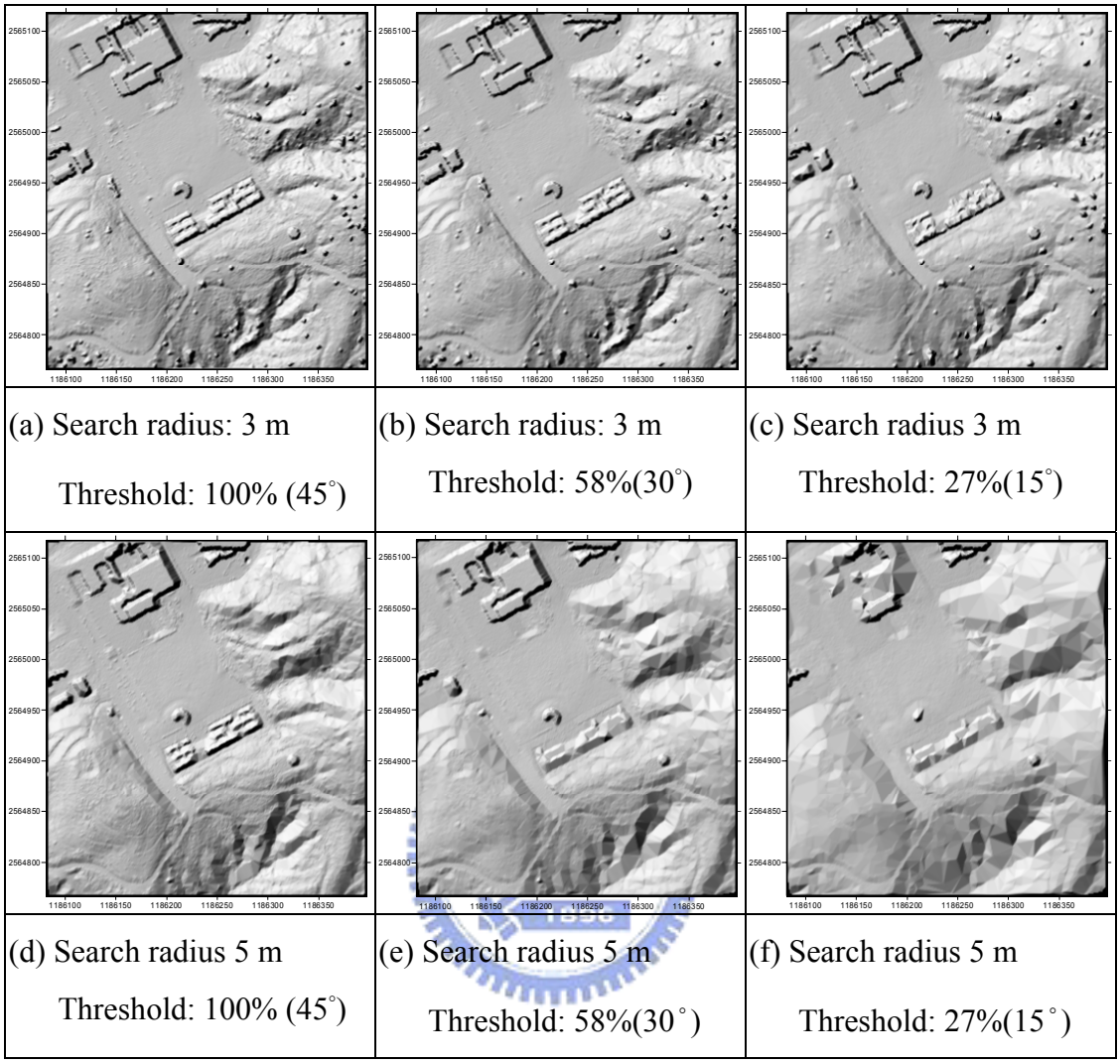


(a) Search radius: 3 m Threshold: 100% (45°)

(b) Search radius: 3 m Threshold: 58%(30°)

(c) Search radius 3 m Threshold: 27%(15°)

(d) Search radius 5 m Threshold: 100% (45°)

(e) Search radius 5 m Threshold: 58%(30°)

(f) Search radius 5 m Threshold: 27%(15°)

Figure 3.8. Six results of slope-based filtering.

## 3.3 Directional steepest-descent filter

Based on the idea of slope-based filter, this paper develops an algorithm to improve the directional effect of slope-based filter. The directional steepest descent filter relies on the steepest slope in the four directions (the same rule as in eight directions or sixteen directions) within a radial distance from a point (Figure 3.9). The steepest descent is similar to equation 3.2.

$$\tan(\alpha_D) = \max_{i=1\sim n} \left\{ \frac{z_p - z_i}{\sqrt{(x_p - x_i)^2 + (y_p - y_i)^2}} \right\} \tag{3.3}$$

where points $(x_i, y_i, z_i)$ represent point $p$'s neighbors along an azimuth $D$ within a radial distance $L$, and $n$ is the total number of $p$'s neighbors in the direction $D$. Figure 3.9 shows the two-dimensional search-space spanned by two specific azimuthal angles and a distance.

The algorithm is to take $p$ as a center and calculate the steepest descent to any other points reached within the four areas. The areas of directions 45 and 225 degrees are taken as a group and 135 and 345 degrees another. The features of central point $p$ are as follows:

(1) point $p$ is located on a peak or point $p$ is a non-terrain point when

the values $\alpha_{45}$, $\alpha_{45+180}$, $\alpha_{135}$, $\alpha_{135+180}$

in the four directions are positive at the same time, for example, being more than 15°.

(2) point $p$ is located on a pit when

the values $\alpha_{45}$, $\alpha_{45+180}$, $\alpha_{135}$, $\alpha_{135+180}$

in four directions are negative and smaller than a given threshold such as -15°.

(3) point $p$ is located on a saddle when

the two slopes $\alpha_{45}$, $\alpha_{45+180}$

in a group are smaller than -15° simultaneously and also the other two slopes $\alpha_{135}$, $\alpha_{135+180}$ in another group are more than +15° at the same time (and vice versa).

(4) $p$ is on a slope in all other cases.

According to the condition (1) mentioned above, taking the minimum of steepest descent:

$$\alpha = \min \{\alpha_{45}, \alpha_{135}, \alpha_{225}, \alpha_{315}\}$$

If $\alpha$ is positive and larger than the threshold value, then point $p$ is identified as a non-terrain point or a terrain point on a peak.

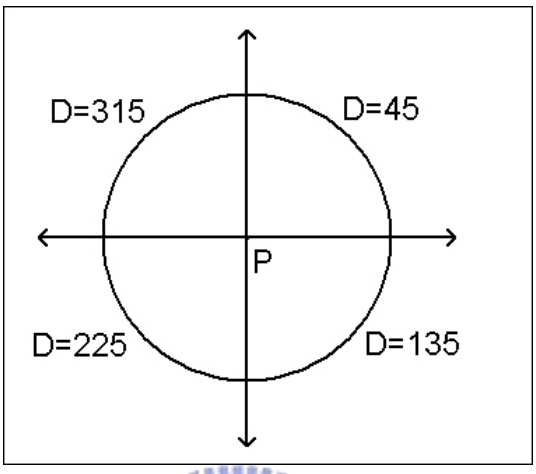


Figure 3.9. Azimuth angle $D$ is measured clockwise from north.

Figure 3.10 and 3.11 show the difference between the slope-based filter and directional steepest-descent filter. The filtering parameters were set at the same values: the search radius as 10 m and the threshold as gradient 0.58 (30° in degree). The slope-based filter removes terrain discontinuities. On the other hand, directional steepest-descent filter preserves terrain features in sloped terrain. However, using a small search radius leads to points on large buildings remaining in both filters.

In Figure 3.11, the profile is delineated along the positions as indicated by a solid line on Figure 3.10 showing the elevations and the calculated steepest slopes (equation 3.2) are labeled on the top of the profile. The steepest slopes of terrain points vary from 0.01 to 0.79 on the flat region and vary from 0.23 to 1.91 on relief region respectively. The steepest slopes of non-terrain points vary from 0.73 to 9.05 on the flat region and vary from 1.9 to 9.7 on relief region. The fact that the steepest

slopes for terrain points and non-terrain points could not be accurately classified.

On the other hand, the directional steepest descents tan($\alpha$) of terrain points vary from 0.01 to 0.5 on the flat region and vary from 0.01 to 0.5 on relief region. The directional steepest descents of non-terrain points vary from 0.25 to 5.92 on the flat region and vary from 0.82 to 9.73 on relief region in Figure 3.11(d).

Directional steepest descent is appropriate for filtering ground objects of smaller sizes. That is, the parameter for the size of a searching window should be small. In order to preserve the terrain points in sloped terrain, the window sizes need to be restricted (Vosselman, 2000). However, a small window size leads to points on large buildings remaining.

When the radius of a searching window size is longer (such as 10 meters), then the terrain points on a peak are illustrated as condition (1). There is no distinction between the steepest-descent values of a terrain point on the peak and a non-ground object. How to determine the threshold value and window size will be solved later.

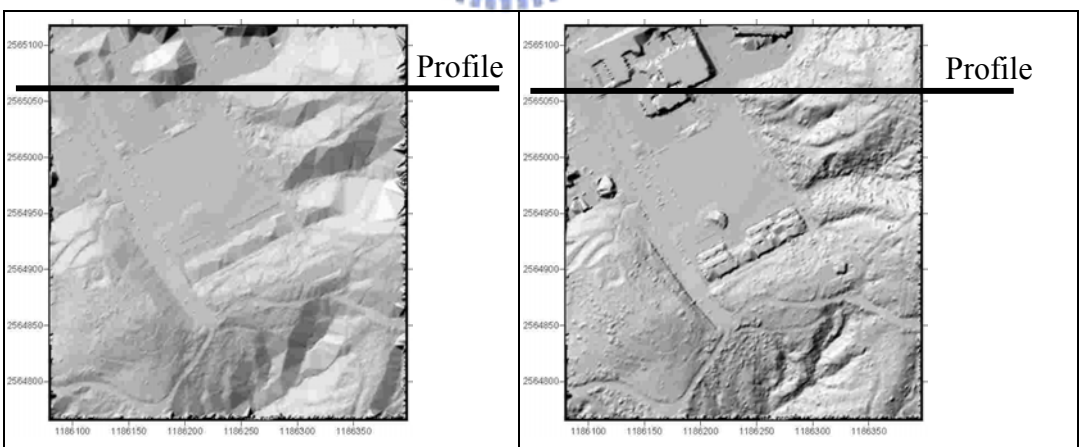


(a) Result of slope-based filter
search radius: 10 m
threshold: 0.58 (58%)

(b) Result of directional steepest-descent filter
search radius: 10 m
threshold: 0.58 (58%)

Figure 3.10. Comparison between slope-based and directional steepest-descent filter.

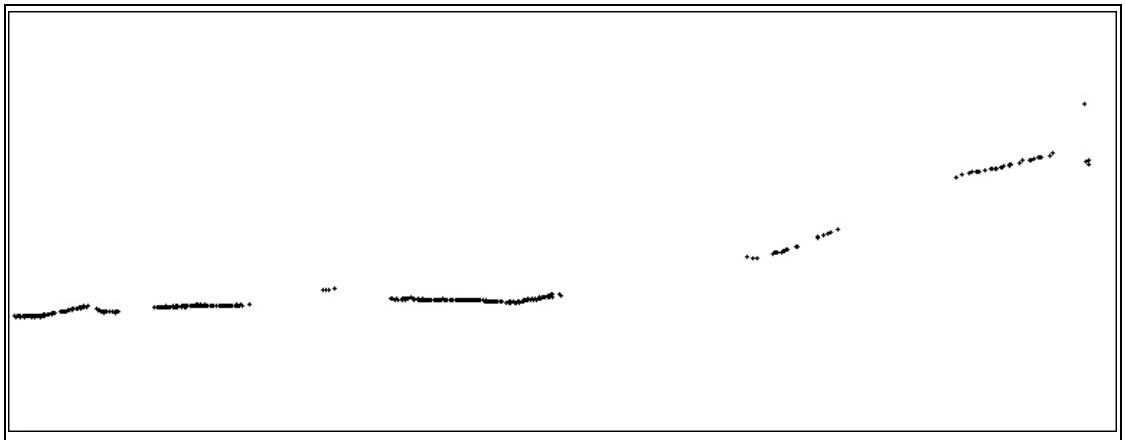

(a) Profile of filtering result using slope-based filter

search radius: 10 m

threshold: 0.58 (58%)

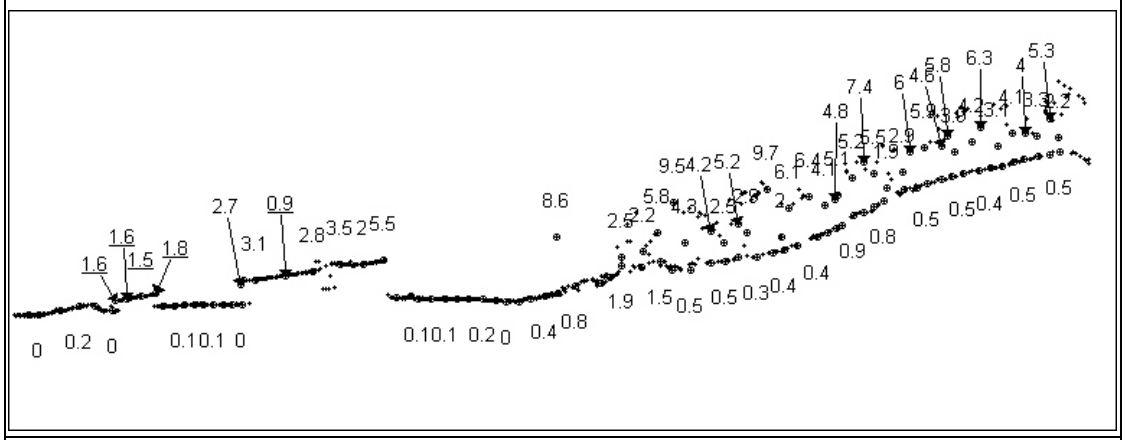


(b) Calculated steepest slopes (gradient) of terrain points are labeled on the button of the profile and of non-terrain points are labeled on the top of the profile.

Figure 3.11. Comparison of profile between slope-based and directional steepest-descent filter.

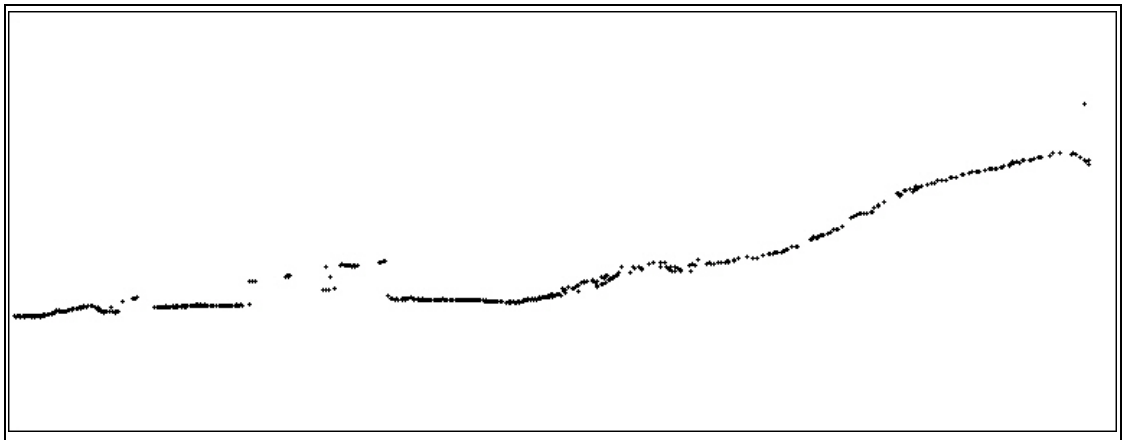

(c) Profile of filtering result using directional steepest descent filter

search radius: 10 m

threshold: 0.58 (58%)

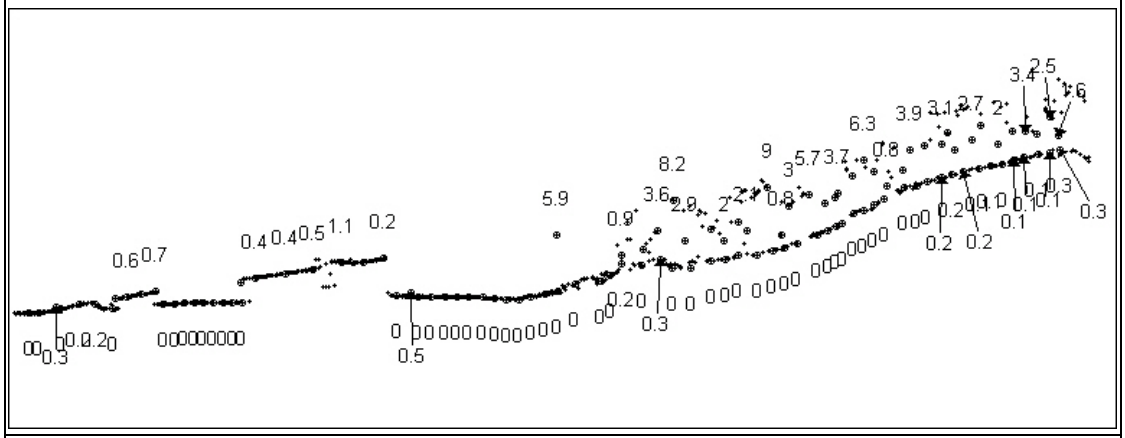

(d) Calculated directional steepest descents of terrain points are labeled on the button of the profile and of non-terrain points are labeled on the top of the profile.

Figure 3.11. Comparison of profile between slope-based and directional steepest-descent filter.

## 3.4 Adaptive directional steepest-descent filter

In order to filter a large ground object, a searching window must be large enough to completely cover the object. When the searching window size is large,

the background terrain may include complex features. One approach to adaptive thresholding is to subtract background slope from the calculated steepest slope and to perform thresholding as uniform slope result. If the slope value of a given point is much larger than its local background slope, we may classify it as a non-terrain point.

Taking $p$ as a center, point $i$ is found in the direction $D$ and the steepest decent $\alpha$ is obtained. Restarting the process by taking $i$ as a center, and along the azimuth $D$ within $L$ radial distance, searching for the steepest descent again, the steepest descent $\beta$ is obtained (Figure 3.12). If $\beta$ is positive gradient, then the original steepest descent $\gamma$ is revised by subtracting $\beta$ from $\alpha$, $\gamma = \alpha - \beta$. Thereby, the goal of removing the background slopes is achieved.

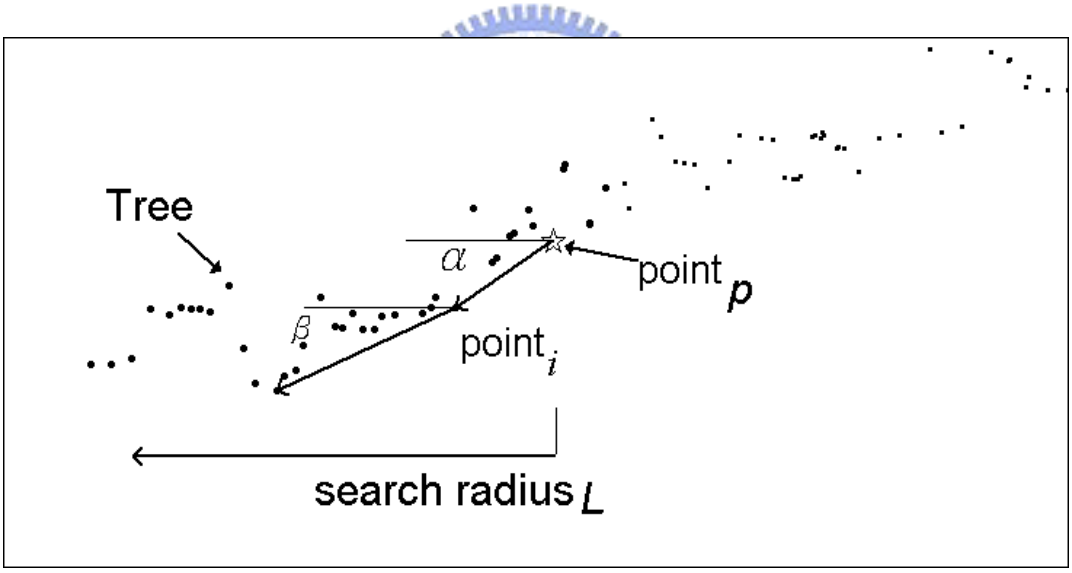


Figure 3.12. The steepest-descent is revised by removing the background slopes.

## 3.5 Adaptive directional elevation-difference filter

The choice of proper window size may be problematic. It is difficult to detect all non-ground objects of various sizes using a fixed window size. For example, in order to remove the measurements of large non-ground objects such as buildings, a larger window size is needed. However, a larger window size may cover complex

terrain or cross a mountain ridge. In this research, for the adoption of a large window size, a different method — directional elevation-difference filter — was developed, as shown in Figure 3.13. First, an initial search radius is used in direction $D$ to search for a lowest point among the neighbors. Then the search radius is reduced by one meter, so that the lowest point in each research radius is gradually calculated and selected. The selected lowest points constitute Set G, as illustrated in Figure 3.13, $G_1$ to $G_6$. The lowest point $G_1$ is found with search radius of $L_1$, and $G_k$ is found with new search radius of $L_k$, and so forth. Subsequently, elevation differences among the sequential lists of Set G are calculated in order, using the formula $dhZ_{D[k]} = Z_{G[k]} - Z_{G[k+1]}$, where $k$ stands for the $k^{th}$ time of reducing the research radius, and $dh$(k) constitutes the set dG of elevation differences. In the set dG of elevation differences, the steepest descent $\delta$ (maximum value) of elevation difference is therefore selected. Once the calculation in direction $D$ is completed, we can start calculating the $\delta$ value in the next direction. The $\delta$ values in the four directions are calculated separately, and the minimum will be selected as $\lambda = \min\{\delta_{45}, \delta_{135}, \delta_{225}, \delta_{315}\}$. If $\lambda$ is lower than the predetermined threshold $dh_{Th}$, then this point will be classified as an object point.

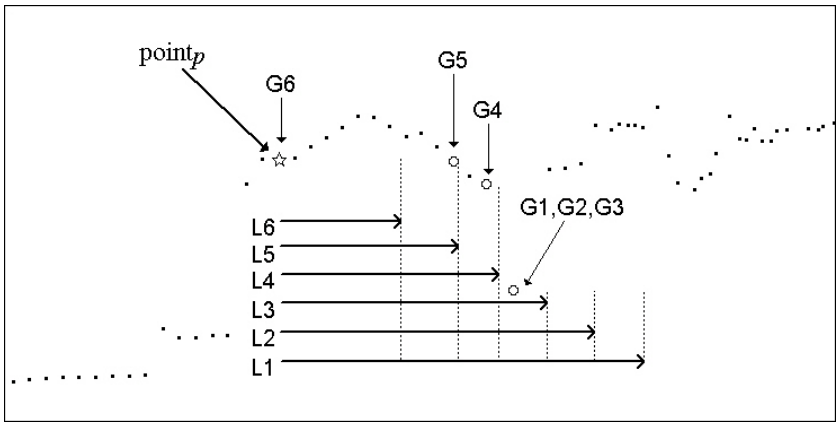


Figure 3.13. Finding the lowest point progressively.

Taking $p$ as a center, the lowest point $G_1$ is found with search radius of $L_1$, the

search radius is reduced, and $G_2$ ($G_2$=$G_1$ in this case) is found with search radius of $L_2$, and so forth.

## 3.6 Determination of search radius

The value of the search radius is a parameter. In this paper, it was proposed that the best search radius for each object point of terrain surface could be calculated automatically. The method of calculation is as follows. First, a larger fixed value is selected as the initial search radius in direction $D$ to search for the lowest spot height among neighboring points. The search radius is then successively reduced, just as with the *directional elevation-difference filter* described above. The lowest points within each radius are selected and constitute set G. Then the elevation differences among each spot height in set G are calculated, which constitutes the elevation differences set dG. An elevation difference threshold $slope_{Th}$ is predetermined. If the elevation differences (negative value) in the sequential list dG are smaller than $slope_{Th}$, these points are identified as relief spots (less smaller negative value indicates larger relief). Accordingly, the points in set G are further selected and constitute set T. In set T, the steepest descent between the relief points and the center $p$ are calculated: $Slope_k = \frac{z_p - z_{T[k]}}{\sqrt{(x_p - x_{T[k]})^2 + (y_p - y_{T[k]})^2}}$ (the calculation of slopes between relief points and the center $p$). The steepest descent is therefore found, as illustrated in Figure 3.14, point $T_1$. In Figure 3.14, the points in set T constitute the profile, where the line of sight from point $p$ to $T_1$ is the steepest descent. The horizontal distance from $p$ to $T_1$ determines the best search radius for the search of object point $p$.

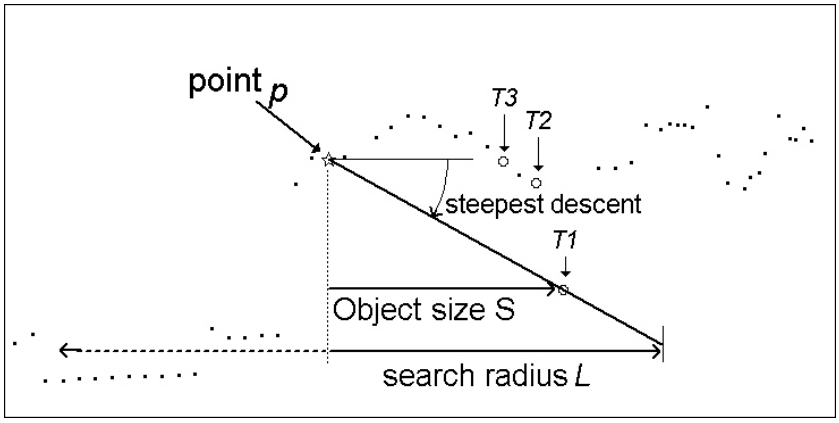


Figure 3.14. Taking *p* as a center, relief spots are further selected and constitute set T.

## 3.7 Filtering by multiple filtering procedures

There are two kinds of errors that can be made in quantitative assessment. A Type I error misclassifies bare-Earth points as object points, meaning details of terrain features are lost. Type II errors misclassify object points as bare-Earth points. Since Type II errors will lead to worse results than Type I error in the application of DTM recovering, most filtering tasks tend to produce many more Type I errors than Type II errors (Sithole and Vosselman, 2004). This paper applies the opposite strategy, emphasizing the reduction of Type I errors because Type II errors are easier to fix by multiple filtering procedures.

The procedures of multiple filtering include three stages. In the large objects removal stage (1), an adaptive elevation-difference filter is used to remove large non-ground objects such as buildings. In the medium object removal stage (2), an adaptive steepest-descent filter removes medium non-ground objects such as dense trees. In the final filtering stage (3), a directional steepest-descent filter removes small non-ground objects such as cars and single trees (Figure 3.15).

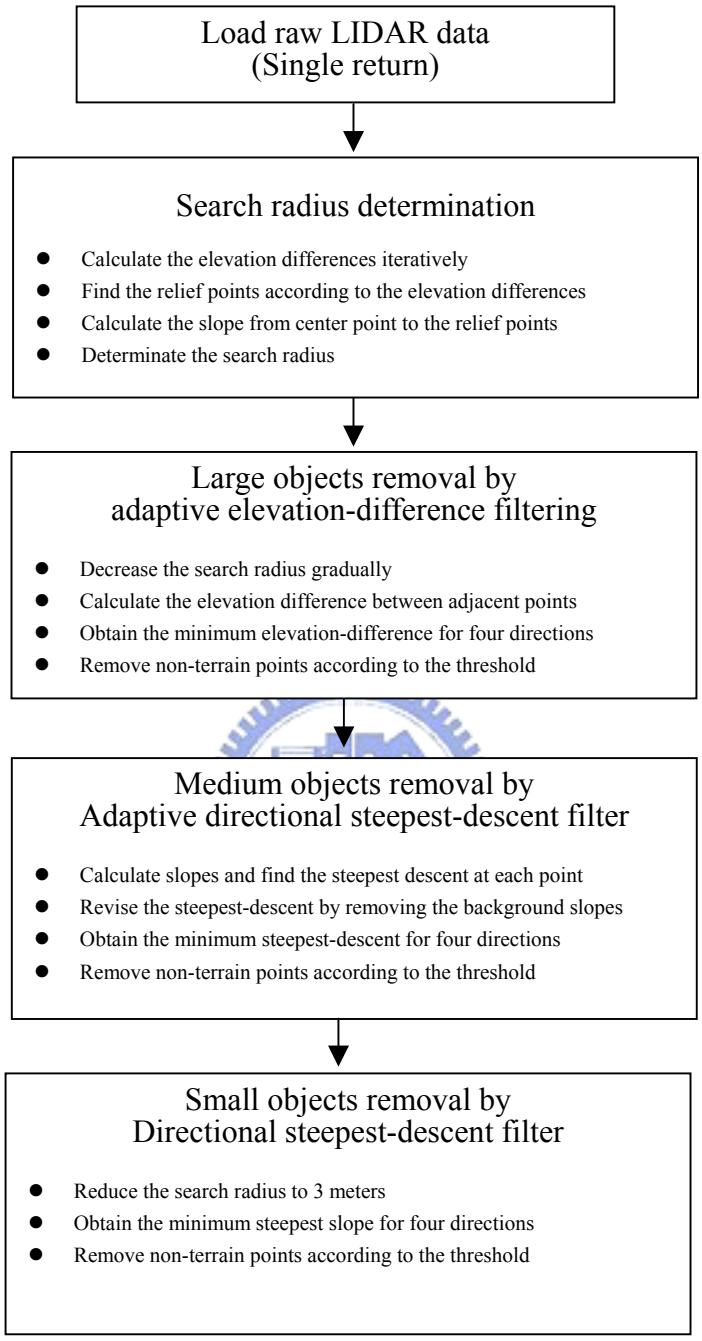


Figure 3.15. Flowchart of the multiple filtering algorithm.

Figure 3.16 delineates a profile with gentle relief that crosses a building and trees. The elevation-difference values are derived along this profile and shown in Figure 3.17. Figure 3.18 shows the steepest-descent values along this profile. Figure 3.17 and 3.18 shows the same phenomenon: these two filters were effective in reducing background nonuniformity.

The values are obtained by subtracting a locally nonuniform background value from the original data and then are suitable to perform a fixed threshold procedure. Before the filtering processes, the point clouds were preprocessed to remove outliers such as birds and low flying aircrafts first. Because high outliers are so far elevated above neighboring points, the filtering process can remove such extreme data easily.

In urban areas, some LIDAR data may contain a few extreme low outliers. These negative blunders are often happened as individual points. When a shaded-relief map was derived, low outliers can be found easily as conical pits. Therefore, extreme low points can be filtered by interactive editing.

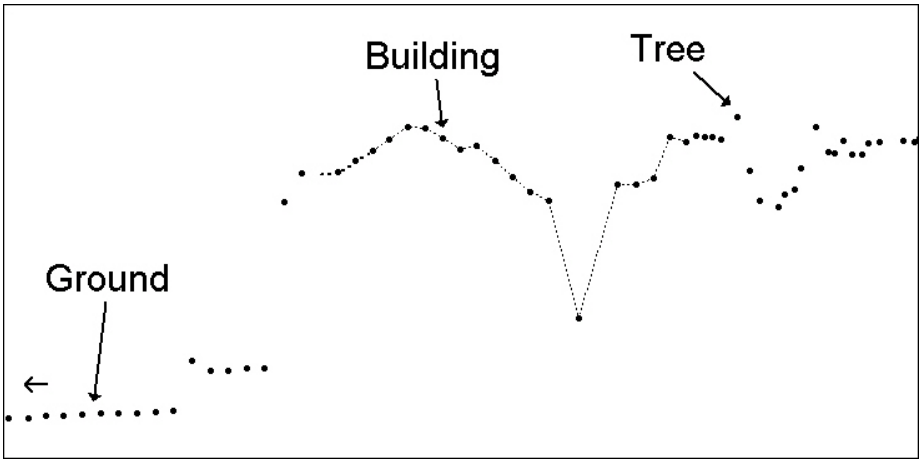


Figure 3.16. Sample profile.

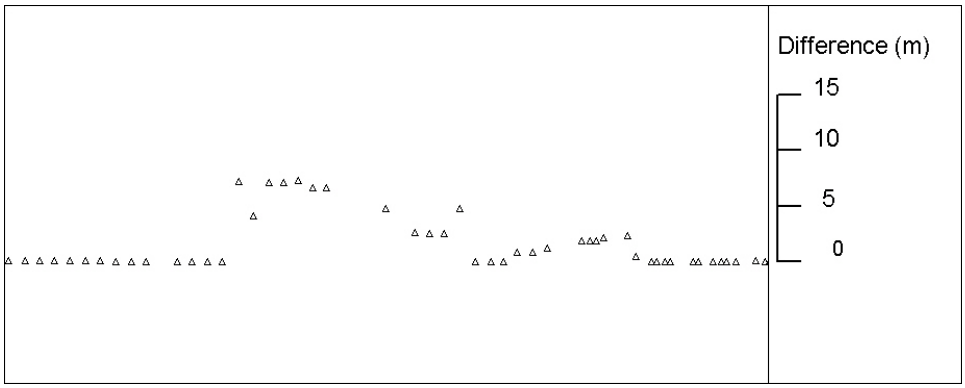


Figure 3.17. The elevation-differences values of the sample profile.

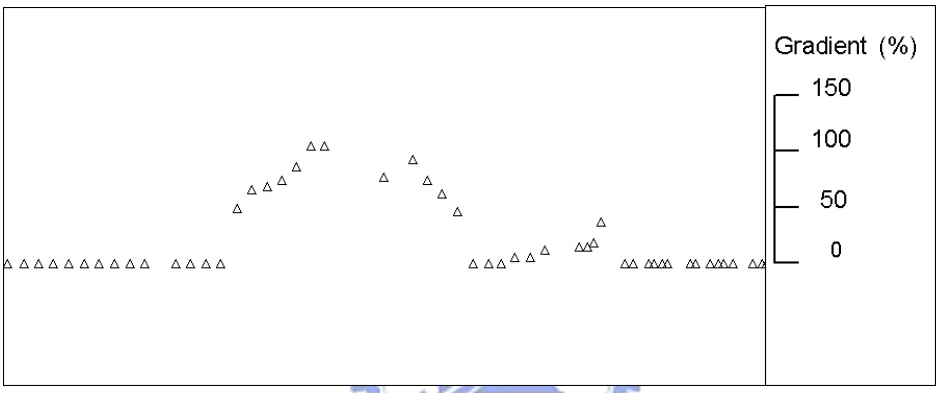


Figure 3.18. The steepest-descent values of the sample profile.

## 3.8 Algorithm implementation

Some algorithms such as morphological operators require the data to be in a grid structure. Interpolating the raw data to a grid causes the height differences in the interpolated data reduced. This research worked with original, irregularly point data.

### Determination of search radius

1. Take an initial size of search window $L_1$.

2. In azimuth $D$, within the $L_1$, load raw data of LIDAR.

3. Decrease the size of window gradually, and calculate the lowest points as set G.

4. Within set G, calculate elevation differences between two adjacent points iteratively, which constitutes set dG.

5. Analyze set dG and set G. If the elevation difference between two adjacent points is smaller than the relief threshold $slope_{Th}$ (negative of the gradient), then it is categorized into set T.

6. Within set T, calculate the slope from the center to each point as set SP, and find the steepest descent point U.

7. The size of this object point $R_D$ is determined by the distance between point U and center point $p$.

8. Go back to step 2. Recalculate the values in the next direction and analyze $R_{D+180}$.

9. The revised size of initial search radius R on center point $p$ is determined by the maximum of $R_D$ in four directions.

## Adaptive directional steepest-descent filter

1. Calculate the initial search radius R by the algorithm described above.

2. In azimuth $D$, within the R, load raw data of airborne LIDAR.

3. Calculate slope set SP.

4.Within SP, find the steepest descent $\alpha$ at point $s$.

5. Use site $s$ as the center with a radius of R, obtaining the background steepest descent $\beta$.

6. If $\alpha$ and $\beta$ are negative values at the same time, then subtract the background slope $\beta$ from $\alpha$ : $\gamma = \alpha - \beta$.

7. Go back to step 2. Calculate $\gamma$ in the next azimuth, $\gamma_{D+180}$.

8. The minimum Min_$\gamma$ is selected among $\gamma_D$ in the four directions.

9. If Min_$\gamma$ < threshold $slope_{Th}$, then this point is a ground point; if not it is a

non-ground object.

### Adaptive directional elevation-difference filter

1. Calculate the size of window R.
2. In azimuth *D*, within the R, load raw data of airborne LIDAR.
3. Decrease the size of window gradually, and calculate the lowest points, which constitute set G.
4. Within set G, calculate the elevation difference between each two adjacent points, which constitute set dG.
5. Within set dG, find the steepest dh.
6. Go back to step 2. Calculate the values in the next direction, and analyze steepest $dh_{D+180}$
7. Obtain the minimum Min_dh among four steepest $dh_D$
8. If Min_dh < $dh_{Th}$, then this point is identified as a ground point; if not, as a non-ground objects

## 3.9 Test datasets

In this study, the developed filters were tested on two LIDAR datasets: an urban area and an area of rugged terrain with dense vegetation. The test dataset for urban area is downloaded from the website of ISPRS Commission III, WG III/3 (http://www.commission3.isprs.org/wg3/). The Csiter1_orig.txt and Csiter2_orig.txt are adopted for this study because of the complexity of feature contents. The features of urban test site are steep slopes, mixture of vegetation and buildings on hillside. The point spacing of laser data is around 1.0 – 1.5 meter. The reference datasets include six samples, namely sample 11, sample 12, sample 21, sample 22,

sample 23, and sample 24. The dataset is described in detail in Sithole and Vosselman (2004).

## High-relief test site

The high-relief test site is located in central Taiwan. The area is the Jeou-Fen-Er-Shan, a hilly area located in the damaged region of central Taiwan (Figure 3.19). The Chi-Chi earthquake caused a large-scale landslide (1100 m by 1910 m) in this area. The test site is 3 km by 3 km and the elevation ranges from 420 to 1100 m; the slope varies between 0 degree and 70.3 degrees. The 75$^{th}$ percentile of the slope is 35.8 degrees, and the average is 26.6 degrees, as given in Table 3.1. Figure 3.20 reveals that the study area is in steep terrain and 70% of the slope is greater than 20 degrees. Land-cover types in the study area are dense woods, tea plants, orchard, low grass and sliding rock.

Two datasets were collected in the high-relief test area. The first dataset was collected using an Optech ALTM 2033 system between March 20 and April 3, 2002. The flying height was at a median altitude of 1100 m above ground level. The second dataset was obtained using an LH ALS 40 between April 10 and April 16, 2002, with flying height of 1800 m above ground level. Both datasets were acquired during leaf-on conditions. The H = 1100 m (ALTM 2033) was intended to collect spatially dense (1-m nominal post spacing) LIDAR data, while the mission of the H = 1800 m (ALS 40) was to collect data over a wider area. Table 3.2 compares the parameters of both sets. It shows that the H = 1100 m data involved narrower FOV (30°) than the H = 1800 m data (40°), and that the H = 1100 m was obtained at a higher laser data rate (33 kHz) than the H = 1800 m (25 kHz). Flight directions for both datasets were North-South, oriented parallel to the hills. There are three strips in the H = 1800 m data set, and ten parallel strips for the H = 1100 m data set. The

H = 1100 m data contains an extra East-West flight strip across the study area.

Table 3.1 Statistics of terrain slopes of test site

| Statistics | Slope (in degree) |
|---|---|
| Average | 26.64 |
| Median | 26.59 |
| Std. Deviation | 13.03 |
| Minimum | 0.01 |
| Maximum | 70.38 |
| $25^{th}$ percentile | 17.55 |
| $75^{th}$ percentile | 35.77 |

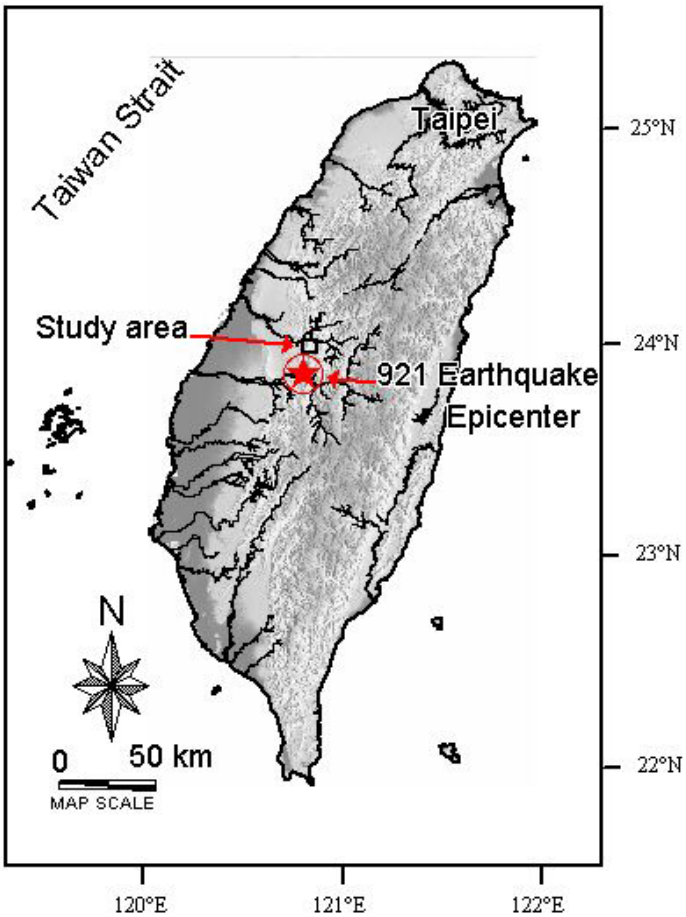


Figure 3.19. High-relief site is located in central Taiwan affected by the Chi-Chi Earthquake.

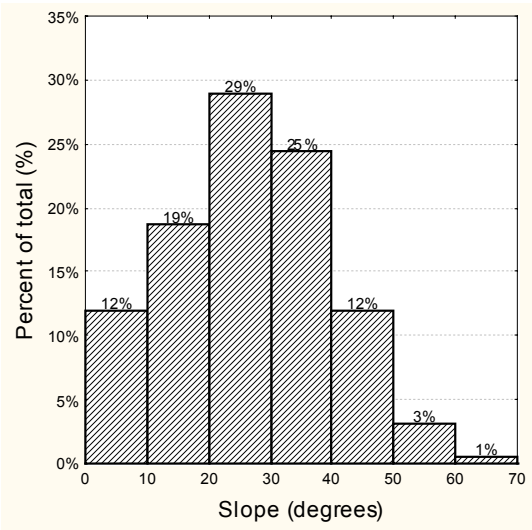


Figure 3.20. Slopes distribution over the test site.

Table 3.2 LIDAR collection parameters of high relief site

| Parameters | Altitude H = 1100 m | Altitude H = 1800 m |
|---|---|---|
| Instrument | Optech ALTM 2033 | LH ALS 40 |
| Max. terrain height | 1154 m | 1154 m |
| Min. terrain height | 396 m | 396 m |
| Airplane speed | 150 knots (77.17 m/s) | 150 knots (77.17 m/s) |
| Flying altitude (above ground) | 900 – 1500 m | 1200 – 2200 m |
| Flight line spacing | 400 m | 500 m |
| Pulse rate | 33 kHz | 25 kHz |
| Scan rate | 38 Hz | 27 Hz |
| Field of view | 30° | 40° |
| Swath width | 482 – 804 m | 870 – 1600 m |
| Point spacing | 1 – 2 m | 2 – 3 m |

## Reference Data of High-relief Area

Data from 906 ground checkpoints, obtained in seven areas with different land-cover, were collected to assess the accuracy of the LIDAR measurement. The measurement incorporates Real-Time-Kinematics (RTK) GPS and the total station technique. The horizontal accuracy of reference data was verified to be about 0.018 m and vertical accuracy 0.020 m, in terms of RMSE. Both the coordinate system of ground checkpoints and the control coordinate system with laser scanning coincided with the same World Geodetic System 1984 (WGS 84) coordinates. Table 3.3 presents the seven evaluation sites:

(1) Pavement area used to assess accuracy on open terrain.

(2) Occlusion path used to assess the accuracy of the occlusion area.

(3) Landslide rock area with homogeneous slopes, with emphasis on the accuracy of the steeper terrain.

(4) Wet soil, covering soft piling and wet soil, with emphasis on the accuracy of wet environment.

(5) Orchard, where only H = 1100 m dataset is available.

(6) Tea farm A with 22 degrees average slope.

(7) Tea farm B with 14 degrees average slop.

This test site does not include built-up areas. Figure 3.21 shows the distribution of the surveyed 906 ground checkpoints. Figure 3.22 depicts field and aerial photographs of these evaluation sites.

Table 3.3 Land-cover classes and their descriptions

| Class | Descriptions |
|---|---|
| Pavement | 9° slopes |
| | Open and flat path |
| Wet soil | 8° slopes |
| | Piling wet soil |
| | Open fields |
| Occlusion path | 8° slopes |
| | High trees on both sides of the 5-m-width path |
| Landslide rock | 25° slopes |
| | Homogeneous steep slope |
| | Open fields |
| Orchard | 9° slopes |
| | Low trees (< 3 meters) |
| Tea farm A | 22° slopes |
| Tea farm B | 14° slopes |

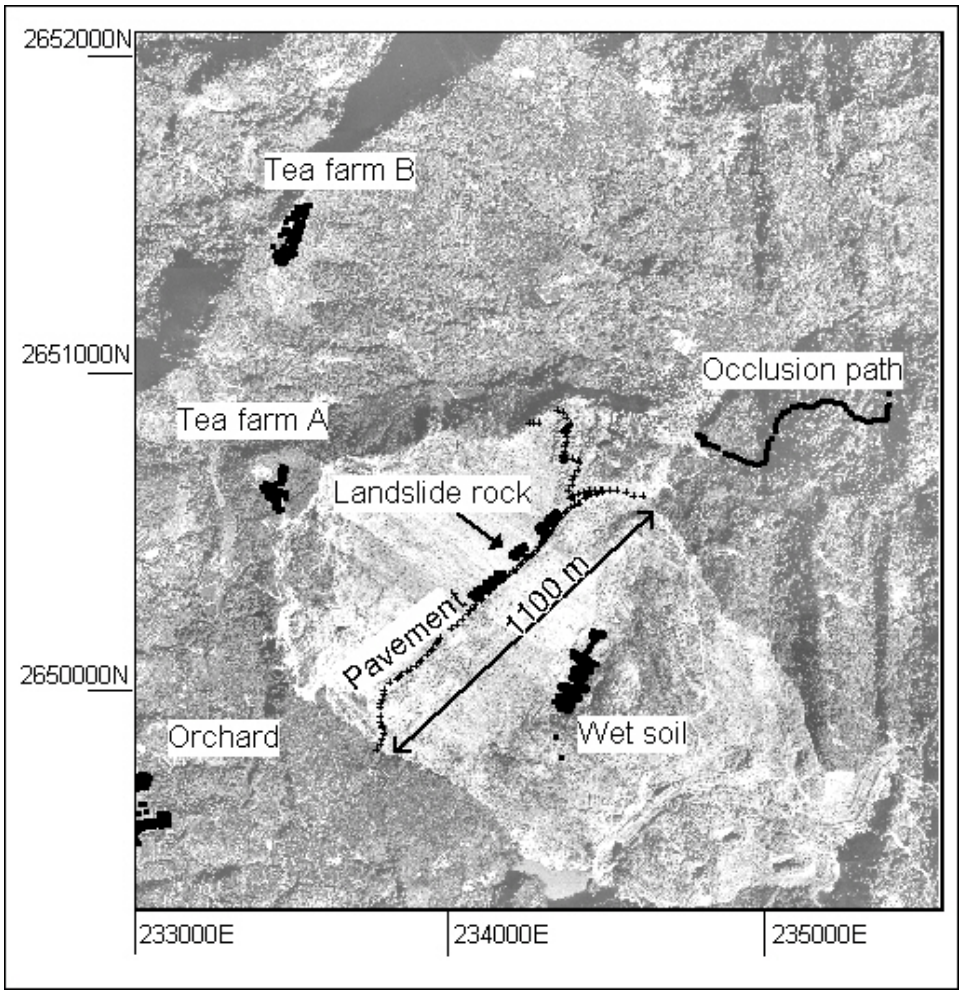


Figure 3.21. Distribution of ground checkpoints in study area.

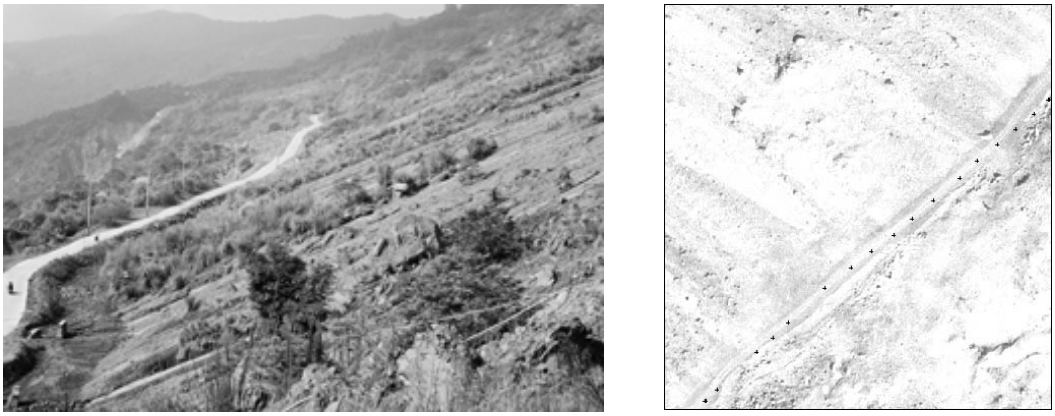

(a) Pavement

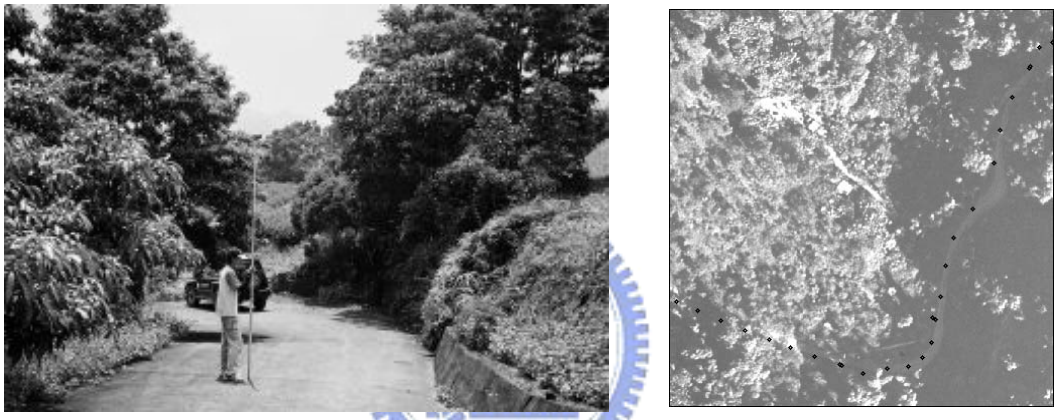

(b) Occlusion path

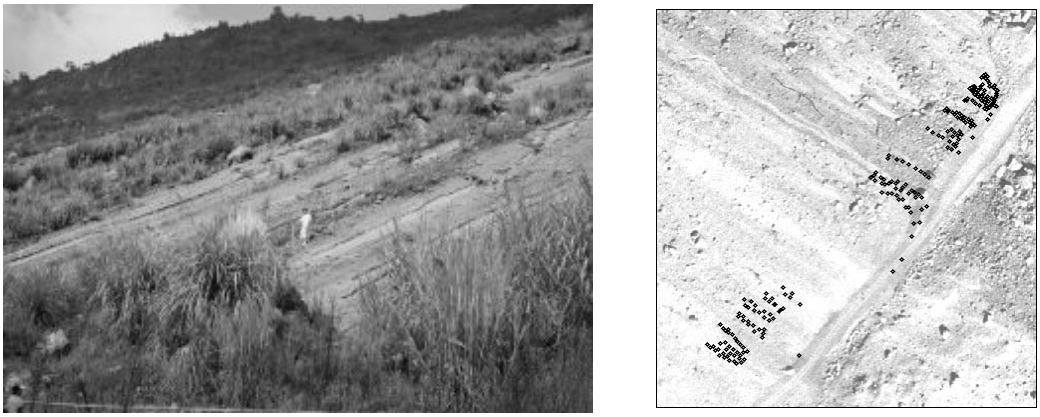

(c) Landslide rock

Figure 3.22. Field and aerial photos of the surveyed site.

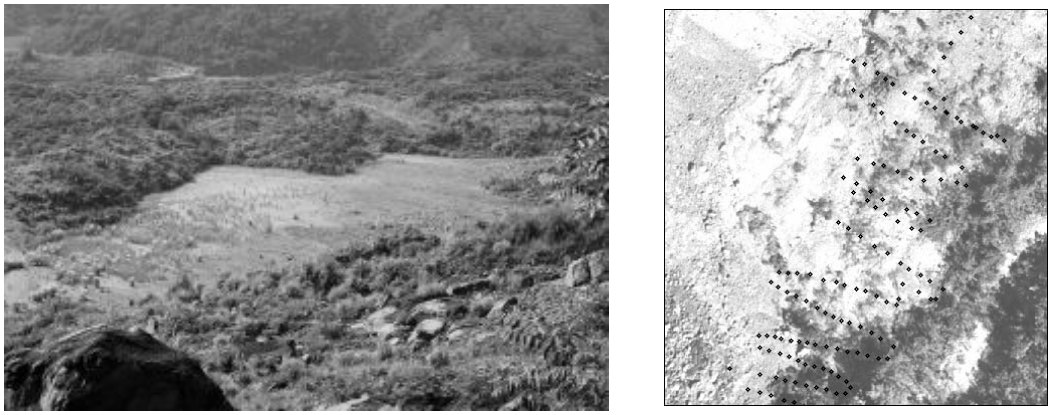

(d) Wet soil

(e) Orchard

(f) Tea farm A

Figure 3.22. Field and aerial photos of the surveyed site.

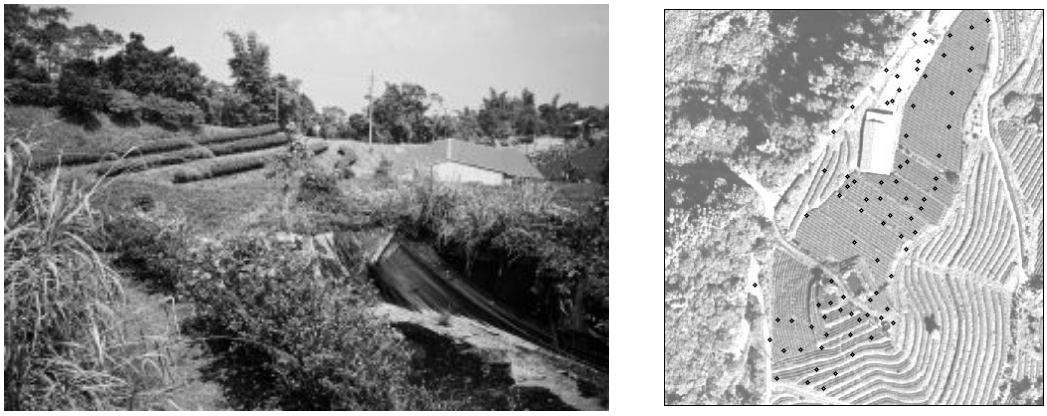

(g) Tea farm B

Figure 3.22. Field and aerial photos of the surveyed site.

## 3.10 Experiment and Evaluation

Two datasets were processed to examine the algorithm's performance. For the urban area dataset, we first focus on the subsite sample 11. The elevation difference threshold $dh_{Th}$ of filtering parameter was set as 1.5 m. The initial search radius was set at 60 m so as to be large enough to remove buildings.

### 1. Sensitivity of Varying Search Radius

Figure 3.23 shows the difference of filtering results by adaptive directional elevation-difference filter with varying search radius. With increasing search radius, Type I errors increased from 11.1% to 11.7%, and Type II error decreased from 11.7% to 11.3%. The filtering result with large search radius (120 m) did not tend to over-filter the ground points. As search radius increased from 60 m to 120 m, the Total error increased from 11.3% to 11.5%, a difference of only 0.2%.

Figure 3.24 shows the difference of filtering results by adaptive directional steepest-descent filter with varying search radius. The steepest-descent threshold $\gamma_{Th}$ of filtering parameter was set as 12%. Similar to the result of adaptive directional elevation-difference filter, the filtering result with large search radius (120 m) did not over-filter the ground points. As search radius increased from 60 m to 120 m, the Total error increased from 11.3% to 11.4%, a difference of only 0.1%.

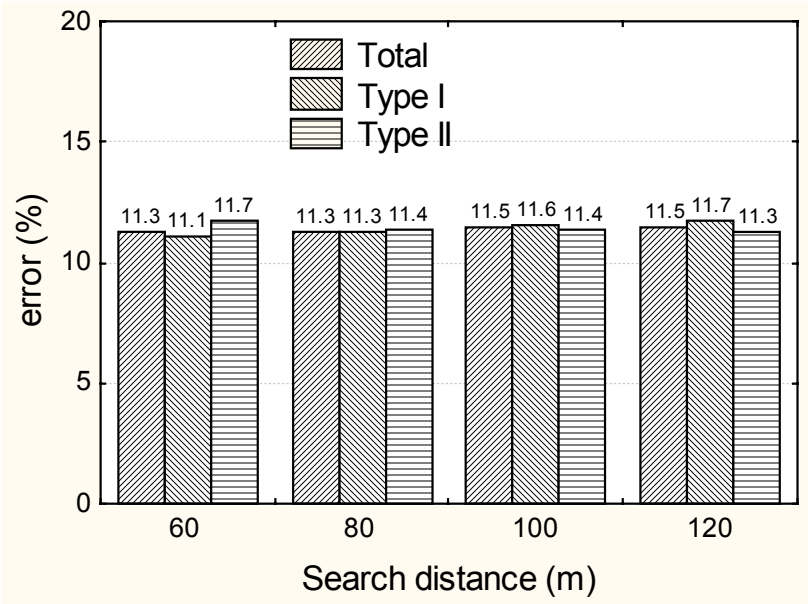


Figure 3.23. Effect of varying initial radius on errors, filtered by directional elevation-difference algorithm.

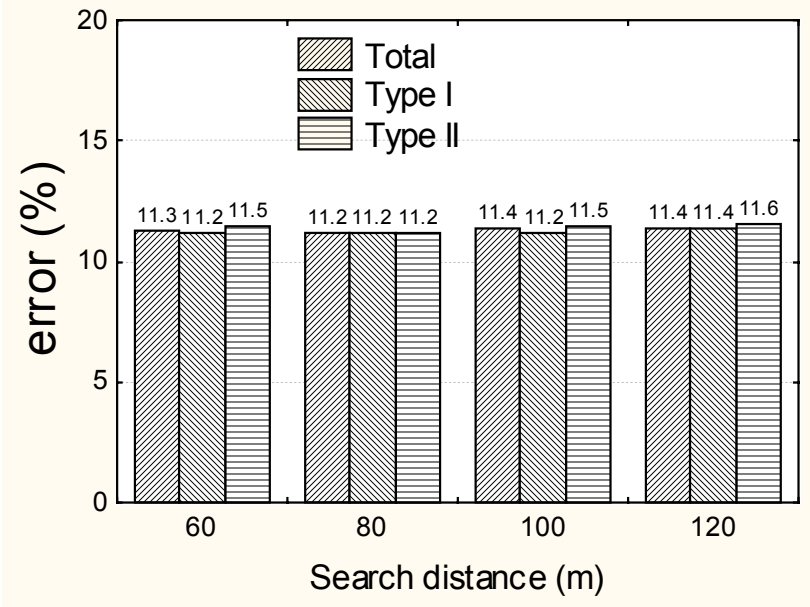


Figure 3.24. Effect of varying initial radius on errors, filtered by adaptive steepest-descent algorithm.

## 2. DTM Generation Results on Urban Area

Figure 3.25 shows the shaded relief maps of six subsites within the urban area for visual inspection. The filtering result of Figure 3.25 was processed by multiple filtering procedures. The parameters used are listed in Table 3.4.

In the large objects removal stage (1), with the adaptive elevation-difference filter, the initial search radius was set at 100 m. A 1.0 m to 2.4 m elevation-difference threshold was used. The elevation-difference thresholds were determined by visual inspection. In the medium object removal stage (2), using adaptive steepest-descent filter, a 15% steepest-descent threshold was used. In the final filtering stage (3), using directional steepest-descent filter, the search radius was set at 3 m and a 3% steepest-descent threshold was used. Comparing the filtered result with reference from Figure 3.25, most non-ground objects were filtered successfully. Low buildings were left in mistakenly surrounding **A** [Figure 3.25(a)]

and **B** [Figure 3.25 (b)]. A few measurements below the bridge were mistakenly removed [**C** in Figure 3.25 (d)]. A few measurements surrounding a complex plaza were chopped off mistakenly [**D** in Figure 3.25 (e)].

The quantitative error examinations of Type I, Type II and the Total errors for the six DTMs are displayed in Figure 3.26 and Table 3.4. The computed errors over six subsites ranged from 0.1% to 10.1%, 4.7% to 9.4% and 3.5% to 9.2% for Type I, Type II and the Total errors respectively. The filtering strategy of this research is trying to minimize Type I errors. Except sample 23, Type I errors of most filtering results are smaller than Type II errors. This is because some measurements in sample 23 (complex scene) were removed mistakenly.

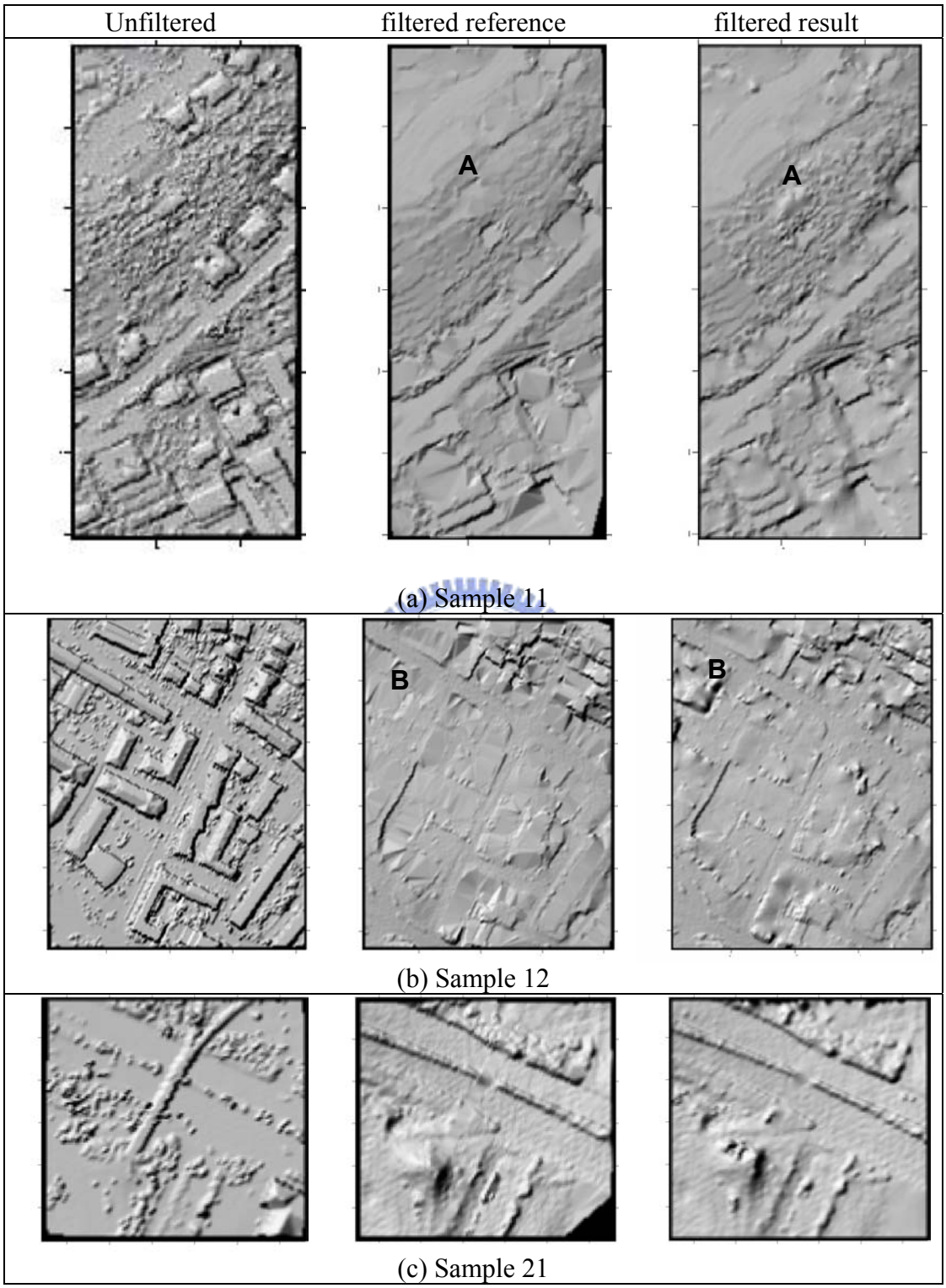


Figure 3.25. The DTM generation results for the urban area.

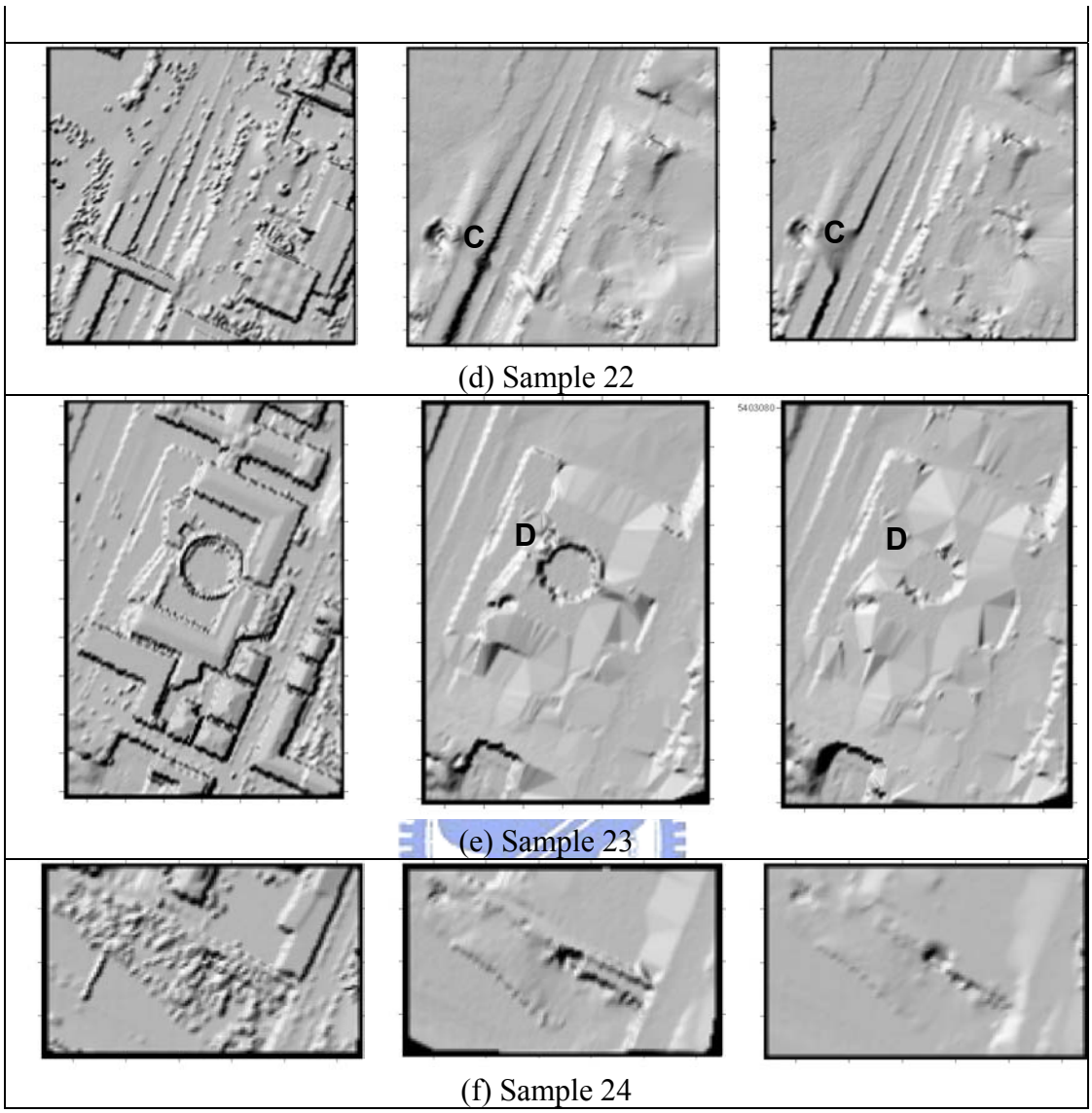


Figure 3.25. The DTM generation results for the urban area.

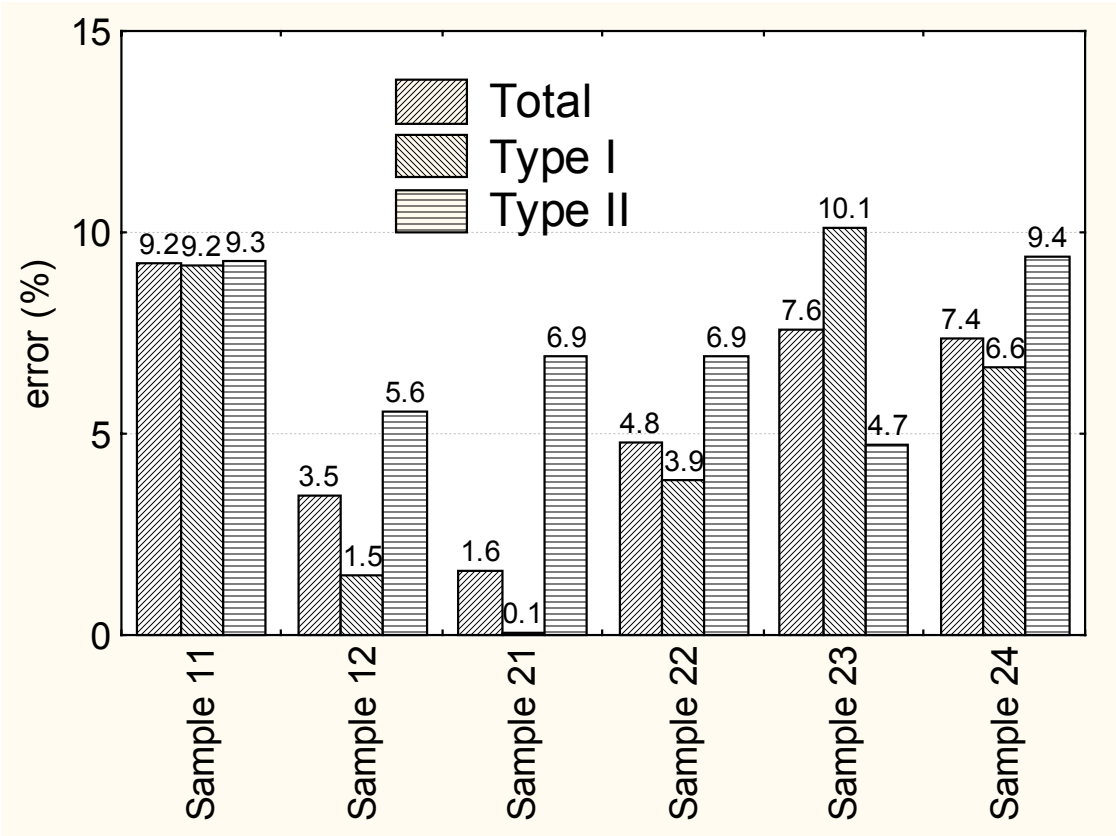


Figure 3.26. The filtering errors for sample sites.

Table 3.4 The accuracy of multiple filtering results

| Sample 11 | | | Filtered | | Error | | Parameters | |
|---|---|---|---|---|---|---|---|---|
| | | | Ground | Non-ground | Type I (%) | 9.16 | Initial radius (m) | 100 |
| Reference | Ground | 21786 | 19791 | 1995 | Type II (%) | 9.28 | Elevation difference (m) | 2.4 |
| | Non-ground | 16224 | 1505 | 14719 | Total (%) | 9.21 | Steepest descent (%) | 15 |
| | Total | 38010 | | | | | | |
| Sample 12 | | | Filtered | | Error | | Parameters | |
| | | | Ground | Non-ground | Type I (%) | 1.48 | Initial radius (m) | 100 |
| Reference | Ground | 26691 | 26295 | 396 | Type II (%) | 5.56 | Elevation difference (m) | 1.2 |
| | Non-ground | 25428 | 1413 | 24015 | Total (%) | 3.47 | Steepest descent (%) | 15 |
| | Total | 52119 | | | | | | |
| Sample 21 | | | Filtered | | Error | | Parameters | |
| | | | Ground | Non-ground | Type I (%) | 0.08 | Initial radius (m) | 100 |
| Reference | Ground | 10085 | 10077 | 8 | Type II (%) | 6.92 | Elevation difference (m) | 1.0 |
| | Non-ground | 2875 | 199 | 2676 | Total (%) | 1.60 | Steepest descent (%) | 15 |
| | Total | 12960 | | | | | | |
| Sample 22 | | | Filtered | | Error | | Parameters | |
| | | | Ground | Non-ground | Type I (%) | 3.85 | Initial radius (m) | 100 |
| Reference | Ground | 22504 | 21637 | 867 | Type II (%) | 6.90 | Elevation difference (m) | 1.0 |
| | Non-ground | 10202 | 704 | 9498 | Total (%) | 4.80 | Steepest descent (%) | 15 |
| | Total | 32706 | | | | | | |
| Sample 23 | | | Filtered | | Error | | Parameters | |
| | | | Ground | Non-ground | Type I (%) | 10.13 | Initial radius (m) | 100 |
| Reference | Ground | 13223 | 11884 | 1339 | Type II (%) | 4.73 | Elevation difference (m) | 1.0 |
| | Non-ground | 11872 | 562 | 11310 | Total (%) | 7.58 | Steepest descent (%) | 15 |
| | Total | 25095 | | | | | | |
| Sample 24 | | | Filtered | | Error | | Parameters | |
| | | | Ground | Non-ground | Type I (%) | 6.64 | Initial radius (m) | 100 |
| Reference | Ground | 5434 | 5073 | 361 | Type II (%) | 9.38 | Elevation difference (m) | 1.0 |
| | Non-ground | 2058 | 193 | 1765 | Total (%) | 7.39 | Steepest descent (%) | 15 |
| | Total | 7492 | | | | | | |

## 3. **DTM Generation Results on High-relief Area**

For the high-relief dataset, ground checkpoints in the area of pavement and of wet soil were used to assess the accuracy of LIDAR observations on open terrain.

The 'difference' or elevation error for each checkpoint is computed by subtracting the surveyed elevation of the checkpoint from the LIDAR dataset elevation interpolated at the x/y coordinate of the checkpoint. The interpolation method is the Delaunay triangulation with linear interpolation. LIDAR-derived elevation was converted into triangulated irregular networks. Differences were obtained by subtracting the reference elevation from the LIDAR elevation.

Table 3.5 shows that RMSE error of pavement area is 9.2 cm and of wet soil is 14.5 cm for H = 1100 m dataset. Table 3.6 shows that RMSE error of pavement area is 14.0 cm and of wet soil is greater than 15 cm (RMSE 20.7 cm) for H = 1800 m dataset.

This study adopted the Terrascan software for the automated filtering of LIDAR points. The software's algorithm uses the single-return range data, that is, the last return for the multi-echo. There are four steps involved in the filtering procedure. In the inspecting stage (1), the analyst chooses a series of representative profiles, especially cross-sections of ridges and cross-sections of dense vegetation. In the analyzing stage (2), each profile is measured for the terrain slope, vegetation density, and the largest size of buildings. The coverage was manually divided into multiple overlapping subsets according to terrain slope and vegetation so that each subset has homogenous terrain and vegetation type. After this, the parameter thresholds are determined for each subset. A small height threshold or a large window size removes some detail of the terrain or cuts some hill peaks. A large height threshold or a small window size tends to preserve non-terrain points. After the dataset has

been filtered, a preliminary DTM is derived from the ground points. In the checking stage (3), the chosen representative profiles are then viewed individually to check if the summit has been cut wrongly or the vegetation points were still retained in wooded area. It is an iterative procedure in which the analyst revises the parameter thresholds until the ground points and non-ground points are separated. Finally, in the manual editing stage (4), the shaded relief map is plotted from the DEM to check the filtering results and to manually edit the artifacts.

Two different working schemes are adopted for automatic filtering process. The filtering for H = 1800 m used an automated procedure. In the case of H = 1100 m, the automated procedure was followed by a manual editing to refine the ground points. While processing H = 1800 m data by the automated procedures, the strategy of choosing the parameter thresholds tended to remove as many vegetation points as possible (minimizing the error of classifying non-ground points as ground measurements). On the other hand, processing the H = 1100 m data tends to incorrectly leave ground points (minimizing the error of filtering ground points mistakenly (Sithole and Vosselman, 2003). The reason is that during the manual editing process it is thought to be easier to remove unwanted points than to detect the absence of ground points and add them back in, with the working environment of this study.

Checkpoints in the area of occlusion path, landslide rock, orchard, sloped tea farm A and tea farm B were used for quantitative analysis of filtering accuracy. A 2.0 m elevation-difference threshold and a 15% steepest-descent threshold were used.

* For H = 1100 m dataset, the differences in MAE using multiple-filtering process and automatic removal technique with manual editing are displayed in Figure 3.27. The MAEs of multiple-filtering processing are smaller than those of automatic processing with manual edits for area of occlusion path and sloped tea farm A (H

= 1100 m dataset). On the other hand, the MAEs of multiple-filtering processing are larger than those of automatic processing with manual edits for area of landslide rock, orchard and tea farm B. The total differences in MAE of automatic processing with manual edits (15.4 cm) were smaller than those of multiple-filtering processing (16.6 cm). The *t*-test was significant at the 0.078 level (>0.05 level).

* For H = 1800 m dataset, the MAE of multiple-filtering processing are smaller than those of automatic processing for all areas (Figure 3.28, Table 3.8, Table 3.10). The total differences in MAE of multiple-filtering processing (22.2 cm) were smaller than those of automatic processing (25.4 cm). The *t*-test of total differences in MAE was significant at the 0.004 level (<0.05 level).
* Note that for H = 1100 m, in the area of sloped tea farm A (dense tea tree and sloped relief), the results of proposed algorithms obtain less mean errors (-12.6 cm vs. -26.5 cm) and less MAE (24.6 cm vs. 27.2 cm) than automatic processing with manual edits scheme (Table 3.7, Table 3.9).
* For H = 1800 m, in the area of sloped tea farm A, the results of proposed algorithms also have better performance (19.2 cm vs. 26.3 cm mean error and 26.1 cm vs. 29.0 cm MAE).

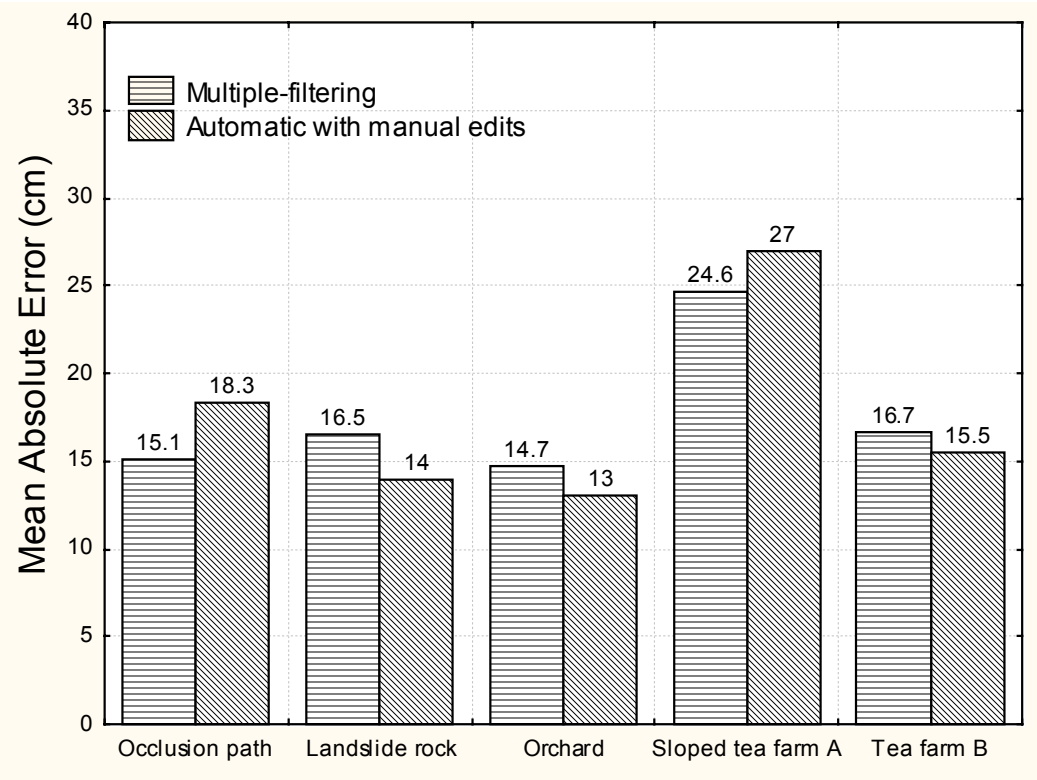


Figure 3.27. The comparisons of DTMs for H = 1100 m.

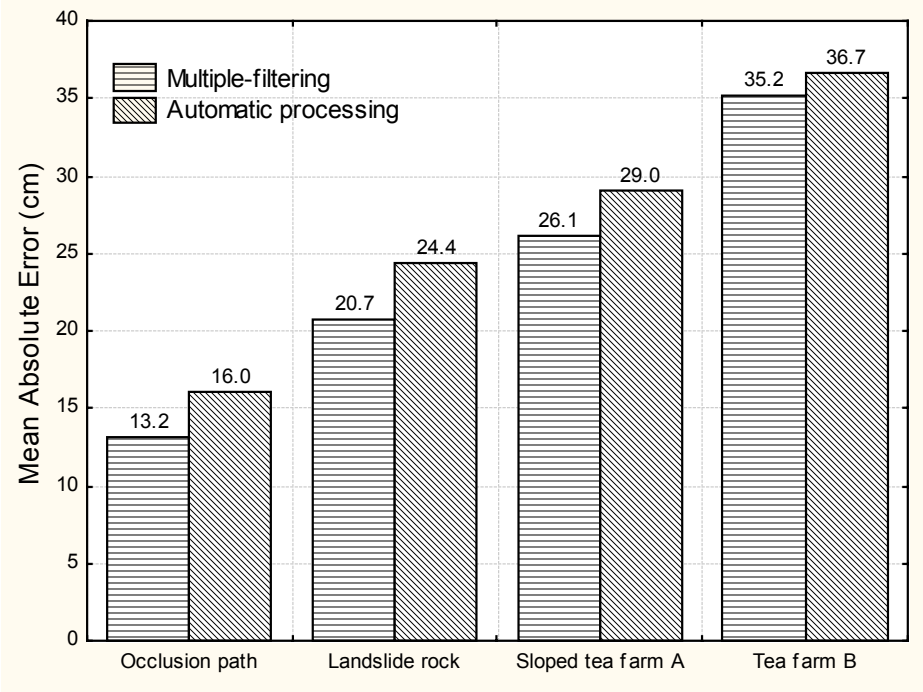


Figure 3.28. The comparisons of DTMs for H = 1800 m.

Table 3.5 Accuracy of DTM in bald earth areas (H = 1100 m, error in cm)

| | Pavement | Wet soil |
|---|---|---|
| 95% # of points | 130 | 82 |
| 95% RMSE | 8.2 | 13.9 |
| 95% MAE | 6.4 | 11.8 |
| 95% Mean error | -1.4 | -10.2 |
| 95% Median | -0.6 | -11.6 |
| 95% Skew | -0.310 | +0.272 |
| 95% Std Dev | 8.1 | 9.5 |
| 95% Min | -20.1 | -26.2 |
| 95% Max | 14.1 | 9.9 |
| | | |
| 100% # of points | 137 | 86 |
| 100% RMSE | 9.2 | 14.5 |
| 100% MAE | 7.1 | 12.2 |
| 100% Mean error | -1.7 | -10.2 |
| 100% Skew | -0.428 | +0.173 |
| 100% Std Dev | 9.1 | 10.4 |
| 100% Min | -28.4 | -36.3 |
| 100% Max | 14.8 | 11.6 |

Table 3.6 Accuracy of DTM in bald earth areas (H = 1800 m, error in cm)

| | Pavement | Wet soil |
|---|---|---|
| 95% # of points | 130 | 82 |
| 95% RMSE | 11.7 | 20.3 |
| 95% MAE | 9.9 | 18.4 |
| 95% Mean error | -4.6 | -18.4 |
| 95% Median | -5.7 | -17.2 |
| 95% Skew | +0.119 | -0.463 |
| 95% Std Dev | 10.8 | 8.6 |
| 95% Min | -36.3 | -37.9 |
| 95% Max | 17.3 | -4.9 |
| | | |
| 100% # of points | 137 | 86 |
| 100% RMSE | 14.0 | 20.7 |
| 100% MAE | 11.2 | 18.5 |
| 100% Mean error | -5.3 | -18.5 |
| 100% Skew | +0.553 | -0.411 |
| 100% Std Dev | 13.0 | 9.4 |
| 100% Min | -50.4 | -40.4 |
| 100% Max | 21.2 | 1.0 |

Table 3.7 Accuracy of DTM for automatic processing with manual edits (H = 1100 m, error in cm)

| | Occlusion path | Landslide rock | Orchard | Sloped tea farm A | Tea farm B | Total |
|---|---|---|---|---|---|---|
| 95% # of points | 78 | 330 | 119 | 44 | 78 | 649 |
| 95% RMSE | 19.4 | 15.5 | 15.2 | 31.3 | 15.9 | 16.7 |
| 95% MAE | 17.9 | 12.7 | 12.0 | 26.4 | 13.6 | 13.8 |
| 95% Mean error | -17.9 | 11.3 | 4.4 | -26.3 | -4.8 | -9.4 |
| 95% Median | -17.4 | 10.8 | 1.1 | -26.0 | -7.7 | -10.4 |
| 95% Skew | -0.299 | 0.069 | 0.477 | -0.253 | 0.871 | 0.443 |
| 95% Std Dev | 7.5 | 10.7 | 14.6 | 17.2 | 15.2 | 13.7 |
| 95% Min | -34.6 | -17.5 | -19.3 | -59.8 | -32.3 | -43.5 |
| 95% Max | -4.2 | 36.5 | 36.4 | 1.4 | 34.5 | 29.9 |
| | | | | | | |
| 100% # of points | 82 | 348 | 125 | 46 | 82 | 683 |
| 100% RMSE | 20.2 | 17.7 | 16.4 | 32.7 | 19.9 | 19.4 |
| 100% MAE | 18.3 | 14.0 | 13.0 | 27.2 | 15.5 | 15.4 |
| 100% Mean error | -18.1 | 11.1 | 4.5 | -26.5 | -4.0 | -9.3 |
| 100% Median | -17.4 | 10.8 | 1.1 | -26.0 | -7.7 | -10.4 |
| 100% Skew | -0.330 | -0.451 | 0.437 | -0.303 | 1.516 | 0.541 |
| 100% Std Dev | 9.0 | 13.8 | 15.9 | 19.4 | 19.6 | 17.1 |
| 100% Min | -45.1 | -66.5 | -25.9 | -75.9 | -43.5 | -75.9 |
| 100% Max | 8.7 | 54.8 | 40.7 | 15.2 | 85.1 | 85.1 |

Table 3.8 Accuracy of DTM for automatic processing (H = 1800 m, error in cm)

| | Occlusion path | Landslide rock | Sloped tea farm A | Tea farm B | Total |
|---|---|---|---|---|---|
| 95% # of points | 78 | 330 | 44 | 78 | 530 |
| 95% RMSE | 18.3 | 25.8 | 37.6 | 40.0 | 26.6 |
| 95% MAE | 14.3 | 22.6 | 27.2 | 32.7 | 22.5 |
| 95% Mean error | -6.8 | -15.7 | 25.8 | 29.3 | -5.0 |
| 95% Median | -4.7 | -19.4 | 18.5 | 29.2 | -9.4 |
| 95% Skew | -0.140 | 0.650 | 1.072 | 0.555 | 0.541 |
| 95% Std Dev | 17.1 | 20.4 | 27.7 | 27.5 | 26.1 |
| 95% Min | -40.6 | -54.6 | -16.2 | -43.4 | -52.5 |
| 95% Max | 31.3 | 37.7 | 93.5 | 123.5 | 66.3 |
| | | | | | |
| 100% # of points | 82 | 348 | 46 | 82 | 558 |
| 100% RMSE | 21.0 | 28.4 | 40.2 | 47.0 | 32.1 |
| 100% MAE | 16.0 | 24.4 | 29.0 | 36.7 | 25.4 |
| 100% Mean error | -6.3 | -15.1 | 26.3 | 29.2 | -3.9 |
| 100% Median | -4.7 | -19.4 | 18.5 | 29.2 | -9.4 |
| 100% Skew | 0.339 | 0.804 | 0.974 | 0.179 | 0.986 |
| 100% Std Dev | 20.2 | 24.1 | 30.8 | 37.1 | 31.8 |
| 100% Min | -47.5 | -76.1 | -29.6 | -88.5 | -88.5 |
| 100% Max | 60.7 | 82.5 | 106.4 | 157.0 | 157.0 |

Table 3.9 Accuracy of DTM for multiple-filter processing (H=1100m, error in cm)

| | Occlusion path | Landslide rock | Orchard | Sloped tea farm A | Tea farm B | Total |
|---|---|---|---|---|---|---|
| 95% # of points | 78 | 330 | 119 | 44 | 78 | 649 |
| 95% RMSE | 16.5 | 18.4 | 17.8 | 27.9 | 17.9 | 17.8 |
| 95% MAE | 14.6 | 15.4 | 13.8 | 22.8 | 14.0 | 14.8 |
| 95% Mean error | -14.6 | 14.7 | 8.3 | -13.6 | -3.8 | 6.2 |
| 95% Median | -14.2 | 13.8 | 3.1 | -10.8 | -4.9 | 7.5 |
| 95% Skew | -0.329 | 0.158 | 0.415 | 0.260 | -0.235 | -0.170 |
| 95% Std Dev | 7.8 | 11.1 | 15.9 | 24.6 | 17.6 | 16.8 |
| 95% Min | -33.6 | -11.4 | -19.3 | -52.9 | -66.9 | -39.6 |
| 95% Max | -1.2 | 42.8 | 39.9 | 45.1 | 34.1 | 40.0 |
| | | | | | | |
| 100% # of points | 82 | 348 | 125 | 46 | 82 | 683 |
| 100% RMSE | 17.5 | 20.0 | 18.9 | 30.4 | 23.6 | 20.9 |
| 100% MAE | 15.1 | 16.5 | 14.7 | 24.6 | 16.7 | 16.6 |
| 100% Mean error | -14.8 | 14.5 | 8.4 | -12.6 | -3.8 | 5.8 |
| 100% Median | -14.2 | 13.8 | 3.1 | -10.8 | -4.9 | 7.5 |
| 100% Skew | -0.506 | -0.468 | 0.359 | 0.680 | 0.067 | -0.376 |
| 100% Std Dev | 9.3 | 13.9 | 17.0 | 28.0 | 23.4 | 20.1 |
| 100% Min | -43.7 | -61.6 | -23.8 | -55.0 | -74.7 | -74.7 |
| 100% Max | 10.1 | 50.6 | 44.3 | 73.4 | 86.7 | 86.7 |

Table 3.10 Accuracy of DTM for multiple-filter processing (H=1800m, error in cm)

| | Occlusion path | Landslide rock | Sloped tea farm A | Tea farm B | Total |
|---|---|---|---|---|---|
| 95% # of points | 78 | 330 | 44 | 78 | 530 |
| 95% RMSE | 14.8 | 22.5 | 31.6 | 38.3 | 24.4 |
| 95% MAE | 11.5 | 18.7 | 24.3 | 33.6 | 19.8 |
| 95% Mean error | -32.6 | -11.0 | 19.0 | 33.4 | -0.5 |
| 95% Median | -30.3 | -12.0 | 14.6 | 33.8 | -3.1 |
| 95% Skew | -0.160 | 0.221 | 0.349 | 0.155 | 0.370 |
| 95% Std Dev | 14.9 | 19.6 | 25.5 | 18.9 | 24.4 |
| 95% Min | -33.3 | -49.9 | -37.9 | -8.2 | -47.0 |
| 95% Max | 27.6 | 43.3 | 76.5 | 79.4 | 61.7 |
| | | | | | |
| 100% # of points | 82 | 348 | 46 | 82 | 558 |
| 100% RMSE | 18.1 | 25.4 | 34.0 | 42.4 | 28.5 |
| 100% MAE | 13.2 | 20.7 | 26.1 | 35.2 | 22.2 |
| 100% Mean error | -5.8 | -10.5 | 19.2 | 34.4 | 0.1 |
| 100% Median | -30.3 | -12.0 | 14.6 | 33.8 | -3.1 |
| 100% Skew | 0.480 | 0.488 | 0.348 | 1.573 | 0.714 |
| 100% Std Dev | 18.2 | 23.2 | 28.4 | 25.0 | 28.5 |
| 100% Min | -46.7 | -73.5 | -40.0 | -13.7 | -73.5 |
| 100% Max | 74.0 | 70.9 | 88.5 | 161.5 | 161.5 |

# CHAPTER FOUR: ERROR ASSESSMENT AND DTM VALIDATION

Evaluating LIDAR accuracy based on both land-cover types and terrain characteristics is important. The vegetation types for collecting reference points are commonly divided into basic land-cover categories such as tall weeds, brush/low trees, and forests. This chapter considers some quantitative descriptors such as vegetation angle, canopy volumes and LIDAR-derived tree height, to characterize the relationship between elevation accuracy and the types of vegetation. In this chapter, an approach was proposed to identify vegetation characteristics based on LIDAR data. The derived vegetation information was factored into the evaluation of the impact of vegetation types on the accuracy of LIDAR-derived elevation.

This investigation compared two overlapping datasets in high-relief test site in central Taiwan. The test sites are of different type topography, with slopes ranging from 0° to 70.3°. These two datasets were obtained from different flying altitudes under leaf-on conditions. LIDAR-derived elevation was compared with in situ measurements. The procedure for evaluation of LIDAR data quality was also assessed.

## 4.1 Characterization of vegetation information

The method to determine tree heights was straightforward. The maximum height surface was calculated from the point clouds of the all-point data set by selecting the maximum elevation values within a 2-m sided square. The maximum height surface represents treetops or ground when there is no tree cover above the

ground. After this process, a grid DSM with 2-meter resolution is formed. A grid DEM with the same resolution is also linearly interpolated with TIN structure from the point clouds of the ground points. The difference between the grid DSM and grid DEM is used to obtain the vegetation height. If the cell value of vegetation height model is less than a threshold (0.3 m), the cell is assumed to refer to a small object or to be on the ground and is eliminated from the vegetation height model. The threshold 0.3 m represents two times the standard deviation of the elevation error (nominal accuracies 0.15 m).

The descriptors for characterization of vegetation information are based on the checkpoints. These descriptors include:

(1) Average tree height: calculated from the vegetation height model by find the mean of the vegetation cells reached by a search distance (15 m) from the checkpoint.

(2) Canopy cover (%): counting the number of vegetation cells reached by a search distance (15 m) from the checkpoint, dividing by the number of total cells reached.

(3) Average canopy volume ($m^3$/sq m): the stem volume ($m^3$/ sq m) in the area reached, in which volume is estimated from cell area and the height of the vegetation pixel. The average canopy volume is close to the mean tree height multiplied by the canopy cover. For similar canopy volumes, low mean tree heights indicate a dense canopy while tall mean tree heights indicate a sparse canopy. To characterize the interaction effect of tree height and canopy cover (%), the view-shed concept of calculating the line-of-sight of vegetation (i.e. vegetation angle) is adopted.

(4) Vegetation angle

Yokoyama *et al*. (2002) proposed the application of digital elevation models based on terrain openness to visualize topographic character. This index is computed

with the all-point data set. Figure 4.1 defines the geometric relationship in the profile between the ground checkpoint A ($n_A$, $e_A$, $h_A$) and the laser data point B ($n_B$,$e_B$,$h_B$). The horizontal distance $P$ between A and B is

$$P = \sqrt{(n_A - n_B)^2 + (e_A - e_B)^2} \tag{4.1}$$

and the vegetation angle $\theta_B$ of line AB is

$$\theta_B = \tan^{-1}\left(\frac{h_B - h_A}{p}\right) \tag{4.2}$$

The set of all vegetation angles $\theta$ between checkpoint A and each laser measurement point (filled dots in Figure 4.1) are on a profile along an azimuth $D$ within a radial distance $L$ from the checkpoint. The greatest vegetation angle along an azimuth $D$, shown in Figure 4.1, is defined as directional vegetation angle $\beta_D$, for which the line-of-sight is unobstructed to a specified range $L$.

$$\beta_D = \max_{(n_B, e_B) \in L} (\theta_B) \tag{4.3}$$

Where points ($n_B$, $e_B$, $h_B$) represent B's neighbors along an azimuth $D$ within a radial distance $L$. The range of $\beta_D$ is 0 to 90 degrees and $\beta_D$ is 0 degree when $H_B < H_A$.

The vegetation angle of canopy is obtained as the mean of the greatest vegetation angles in all eight compass directions from the central checkpoint A (Figure 4.2).

$$\beta = (\beta_0 + \beta_{45} + \ldots + \beta_{315})/8 \tag{4.4}$$

Shorter $L$-values emphasize fine canopy features and a longer $L$ emphasizes coarse-scale terrain features. The maximum $L$ should be shorter than half of the

swath width. This study uses $L$ = 20 m. Low vegetation angle of canopy indicates good openness to the sky. For similar tree heights, higher vegetation angles indicate a dense canopy. Similarly, for similar canopy densities, higher elevation angles indicate taller canopies.

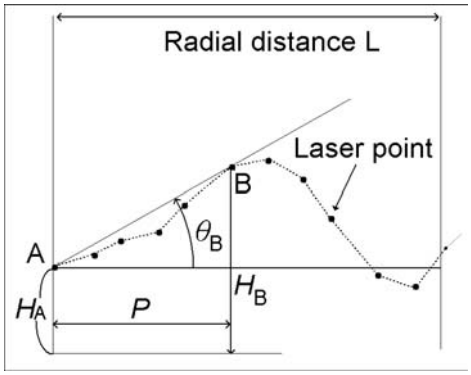


Figure 4.1. The greatest vegetation angle is defined as the maximum angle of the line-of-sight unobstructed to a specified distance $L$.

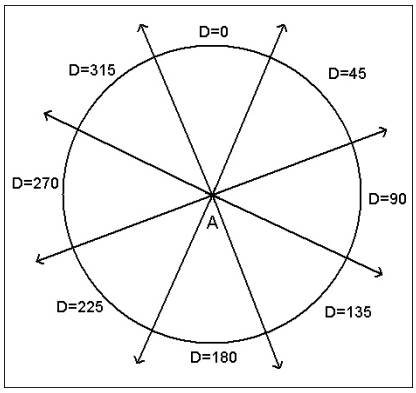


Figure 4.2. Azimuth angle $D$ is measured clockwise from north.

(5) Local roughness of point clouds

To distinguish different vegetation types, the roughness value is computed for each point in the all-point data set. The roughness is defined as the difference between the actual LIDAR measured height and the one interpolated from the enclosing triangle of the point under investigation. For the sake of simplicity, linear interpolation is used. After the roughness model is constructed, the roughness value for each checkpoint is obtained by linear interpolation with TIN from the roughness model.

(6) Determination of point spacing of LIDAR ground returns

The basic concept in evaluating the point spacing of ground returns would be calculating the point spacing of ground points. This study used the distance

between a ground checkpoint and the nearest LIDAR mass point to evaluate the distance between LIDAR ground returns (Hodgson *et al*., 2003). The distance between LIDAR pulses and the canopy penetration may affect the mean distance to the nearest LIDAR point. In non-vegetated areas, the mean distance to the nearest LIDAR point is proportional to the average distance between LIDAR pulses. In vegetated areas, the mean distance to the nearest LIDAR point can be used as an indicator whether the laser points can reach the ground surface (Hodgson *et al*, 2003).

## 4.2 Descriptions of land-cover types by vegetation information

Table 4.1 lists the 29 tree heights measured from a field survey. Analysis of H = 1100 m dataset (Table 4.2) revealed an average tree height of 1.48 meters in the orchard, 1.07 meters in tea farm A, and 1.65 meters in the tea farm B. The differences between surveyed tree height and LIDAR-derived tree height for each area were as follows: orchard (–9 cm), tea farm A (4 cm) and tea farm B (90 cm). The tree height derived from LIDAR is correlated with that measured in the field.

Table 4.1 Summary of 29 tree height measurements from field survey

| Area | # of points | Average (m) | Median (m) | Std. Dev. (m) | Min (m) | Max (m) | 25th Percentile (m) | 75th Percentile (m) |
|---|---|---|---|---|---|---|---|---|
| Orchard | 5 | 1.57 | 2.15 | 0.98 | 0.50 | 2.40 | 0.50 | 2.30 |
| Tea farm A | 12 | 1.03 | 1.10 | 0.29 | 0.20 | 1.20 | 1.05 | 1.20 |
| Tea farm B | 12 | 0.75 | 0.60 | 0.28 | 0.50 | 1.10 | 0.50 | 1.05 |

The vegetated areas in ascending order of the vegetation angle were as follows: orchard, tea farm A, tea farm B, and occlusion path. The ranking order of vegetation

angle is identical to that of canopy volume and local roughness of point clouds for both datasets (Table 4.2, Table 4.3).

Table 4.2 Summary statistics of results for H = 1100 m dataset

| | Evaluation area | | | | | | | |
|---|---|---|---|---|---|---|---|---|
| | Pavement | Landslide rock | Wet soil | Orchard | Tea farm A | Tea farm B | Occlusion path | |
| Number of checkpoints | 137 | 348 | 86 | 125 | 46 | 82 | 82 | *p*-value |
| Tree height (m) | 1.08 | 0.67 | 0.69 | 1.48 | 1.07 | 1.65 | 4.29 | <0.001 |
| Canopy volume ($m^3$/sq m) | 0.20 | 0.07 | 0.04 | 0.30 | 0.40 | 0.50 | 2.44 | <0.001 |
| Canopy cover (%) | 15.2 | 9.0 | 2.1 | 13.1 | 33.1 | 24.0 | 51.5 | <0.001 |
| Vegetation angle (degree) | 15.3 | 21.2 | 5.8 | 20.2 | 23.9 | 26.0 | 43.0 | <0.001 |
| Average local roughness (cm) | 8.3 | 13.8 | 7.3 | 11.7 | 21.7 | 31.8 | 79.2 | <0.001 |
| Mean distance to nearest LIDAR Point (m) | 0.43 | 0.46 | 0.40 | 0.48 | 0.48 | 0.50 | 0.53 | 0.123 |
| Slope (degree) | 8.87 | 25.04 | 8.34 | 8.74 | 21.89 | 13.62 | 7.64 | <0.001 |

Table 4.3 Summary statistics of results for H = 1800 m dataset

| | Evaluation area | | | | | | |
|---|---|---|---|---|---|---|---|
| | Pavement | Landslide rock | Wet soil | Tea farm A | Tea farm B | Occlusion path | |
| Number of checkpoints | 137 | 348 | 86 | 46 | 82 | 82 | *p*-value |
| Tree height (m) | 0.79 | 0.63 | 0.59 | 1.30 | 1.61 | 3.63 | <0.001 |
| Canopy volume ($m^3$/sq m) | 0.25 | 0.25 | 0.03 | 0.38 | 0.54 | 2.35 | <0.001 |
| Canopy cover (%) | 37.1 | 37.5 | 2.5 | 24.0 | 25.8 | 58.5 | <0.001 |
| Vegetation angle (degree) | 14.0 | 19.7 | 3.4 | 20.8 | 24.5 | 48.2 | <0.001 |
| Average local roughness (cm) | 12.9 | 36.6 | 12.0 | 29.8 | 39.9 | 86.8 | <0.001 |
| Mean distance to nearest LIDAR point (m) | 0.53 | 0.63 | 0.57 | 0.79 | 0.77 | 0.62 | 0.008 |
| Slope (degree) | 6.75 | 24.21 | 3.51 | 12.58 | 11.02 | 8.82 | <0.001 |

Table 4.4 shows the relationship between tangent of the vegetation angle and other vegetation information for H = 1100 m dataset. Vegetation angle appears to vary with canopy volume, local roughness of point clouds, and the mean distance to the nearest LIDAR point, i.e., they are measuring the same land-cover phenomenon for H = 1100 m dataset. The tangent of the vegetation angle is exponentially related to the canopy volume [correlation coefficient $r$ = 0.98, $p$-value 0.02 < 0.05 level of significance, $p$-value is the probability of obtaining an $F$ statistic, (Berenson, *et al.*, 2004)]. The tangent of the vegetation angle is significantly linearly correlated with the local roughness of point clouds ($r$ = 0.96, determination coefficient $r^2$ = 0.92, $p$-value 0.04 < 0.05 level of significance). The determination coefficient $r^2$ measures the proportion of variation in Y that is explained by the independent variable X in the regression model (Berenson, *et al.*, 2004).

$$r^2 = \frac{regression\ sum\ of\ squares}{total\ sum\ of\ squares} = \frac{SSR}{SST} \qquad (4.5)$$

$SSR = \sum_{i=1}^{n} (\hat{Y}_i - \overline{Y})^2$ , $SSR$ is equal to the sum of the squared differences between the predicted value of Y and $\overline{Y}$ , the average value of Y.

$SST = \sum_{i=1}^{n} (Y_i - \overline{Y})^2$ , $SST$ is equal to the sum of the squared difference between each observed Y value and $\overline{Y}$ , the average value of Y.

The area with tall and dense vegetation corresponds to a large vegetation angle; therefore the canopy volume and the local roughness of point clouds are also larger. Besides, LIDAR pulses were intercepted by dense vegetation producing a less dense set of ground returns. The larger the vegetation angle, the greater the mean distance

to the nearest LIDAR point is.

Table 4.5 shows the relationship between tangent of the vegetation angle and other vegetation information for H = 1800 m dataset. The tangent of the vegetation angle is exponentially related to the canopy volume (correlation coefficient of regression $r$ = 0.99, $p$-value 0.01 < 0.05 significance level). This angle is also significantly correlated with the local roughness of point clouds linearly ($r$ = 0.99, $r^2$ = 0.98, $p$-value 0.01 < 0.05 significance level). However, unlike the findings in H = 1100 m dataset, the mean distance to the nearest LIDAR point does not follow the ranking order of vegetation angle. After checking the multiple over-flights, it is found that the overlap of flight strips also affect the point spacing of the ground returns in H = 1800 m dataset. The density of LIDAR ground returns is related to the distance between LIDAR pulses, and land-cover type.

In Table 4.2 and 4.3, the average of the local roughness on all checkpoints located in the corresponding site is tabulated. The lowest average local roughness between both datasets is in the wet soil area, followed by the pavement area (roughness < 15 cm). In flat areas, the local roughness provides a measure to assess the internal accuracy of the LIDAR measurements. However, this index does not include the components from systematic errors. Smith *et al*. (2004) presented the quantification of DSM errors introduced during the interpolation process, and examined the spatial pattern of interpolation errors. They demonstrated the increase of errors over break-lines. In both datasets, the greatest values for local roughness of point clouds fall in the occlusion path area, which features a steep slope and high trees on both sides of the path. The local roughness of point clouds in area of occlusion path demonstrates the need for extra measurements to be made to improve surface modeling.

The local roughness of point clouds in each area of H = 1100 m dataset is lower

than that of H = 1800 m dataset, suggesting that more accurate or denser LIDAR measurements in H = 1100 m set yield lower local roughness of point clouds. Notably, the greatest difference of the local roughness of point clouds between two datasets, of up to 165%, is in the landslide rock area (with a slope of 25°). The denser dataset (H = 1100 m) corresponds to a better approximation of the steep terrain surface (i.e., in landslide rock area the local roughness of point clouds was 13.8 cm for H = 1100 m set, compared to 36.6 cm for H = 1800 m set).

Table 4.4 Relationship between vegetation information for H = 1100 m dataset

| | Vegetation angle | | | | | |
|---|---|---|---|---|---|---|
| | tan (0˚) – tan (10˚) | tan (10˚) – tan (20˚) | tan (20˚) – tan (30˚) | tan (30˚) – tan (90˚) | Mixed | *p*-value |
| Number of points | 191 | 353 | 158 | 79 | 781 | |
| Mean tangent of the elevation angle | 0.0994 | 0.2625 | 0.4445 | 0.9486 | 0.3288 | |
| Canopy volume ($m^3$/sq m) | 0.08 | 0.18 | 0.47 | 2.09 | 0.41 | <0.001 |
| Average local roughness (cm) | 11.25 | 12.76 | 20.65 | 90.66 | 21.87 | <0.001 |
| Mean distance to nearest LIDAR point (m) | 0.62 | 0.61 | 0.65 | 0.68 | 0.63 | 0.123 |

Table 4.5 Relationship between vegetation information for H = 1800 m dataset

| | Vegetation angle | | | | | |
|---|---|---|---|---|---|---|
| | tan (0˚) – tan (10˚) | tan (10˚) – tan (20˚) | tan (20˚) – tan (30˚) | tan (30˚) – tan (90˚) | Mixed | *p*-value |
| Number of points | 60 | 304 | 285 | 132 | 781 | |
| Mean tangent of the elevation angle | 0.1246 | 0.2844 | 0.4338 | 1.2357 | 0.4875 | |
| Canopy volume (m3/sq m) | 0.02 | 0.13 | 0.20 | 1.64 | 0.41 | <0.001 |
| Average local roughness (cm) | 13.5 | 29.3 | 29.4 | 69.7 | 35.0 | <0.001 |
| Mean distance to nearest LIDAR point (m) | 0.56 | 0.66 | 0.62 | 0.60 | 0.63 | 0.008 |

## 4.3 Analysis of point spacing of LIDAR ground returns

The distance between each ground checkpoint and its nearest LIDAR point is used in analyzing point spacing of LIDAR ground returns. For purposes of discussion, land-cover type (Tables 4.2 and 4.3) is further classified into two broad groups: bald areas, including pavement, landslide rock and wet soil; and vegetated areas, including orchard, sloped tea farm A, tea farm B, and occlusion path. For H = 1100 m dataset, the average mean distance to the nearest LIDAR point from the group of bald areas (0.45 cm) is significantly shorter than that from the vegetated areas (0.50 cm; *p*-value 0.001 < 0.05 significance level). For H = 1800 m dataset, the average mean distance to the nearest LIDAR point from the bald areas (0.60 cm) is significantly less than that from the group of vegetated areas (0.72 cm; *p*-value 0.001 < 0.05 significance level). The point spacing of ground returns in all areas of H = 1100 m dataset is shorter than those in H=1800m dataset.

## 4.4 Analysis of terrain slope

The steepest average slope was in the area of landslide rock, followed by the area of tea farm A, which has average slope of 22 degree. Notably, the slope derived from H = 1100 m dataset is almost larger than that from H = 1800 m dataset, except occlusion path area. The greatest difference (9.3°) of derived slope between two datasets, of up to 42%, is in the area of tea farm A. Observing from Figure 4.3, the process of vegetation removal has an impact on the slope error. As shown in the shaded relief map, Figure 4.3, H = 1100 m dataset includes the terrain details that allow the steps in the tea plantation to be clearly read. In contrast, an over-filtering

approach adopted for H = 1800 m dataset produces the result of smoothing a slope, and clipping small peaks. The coarse digital elevation model obtained by interpolating ground points from less dense H = 1800 m dataset will be underestimated. The density of LIDAR ground returns is related to the distance between LIDAR pulses, land-cover type, and vegetation removal approach.

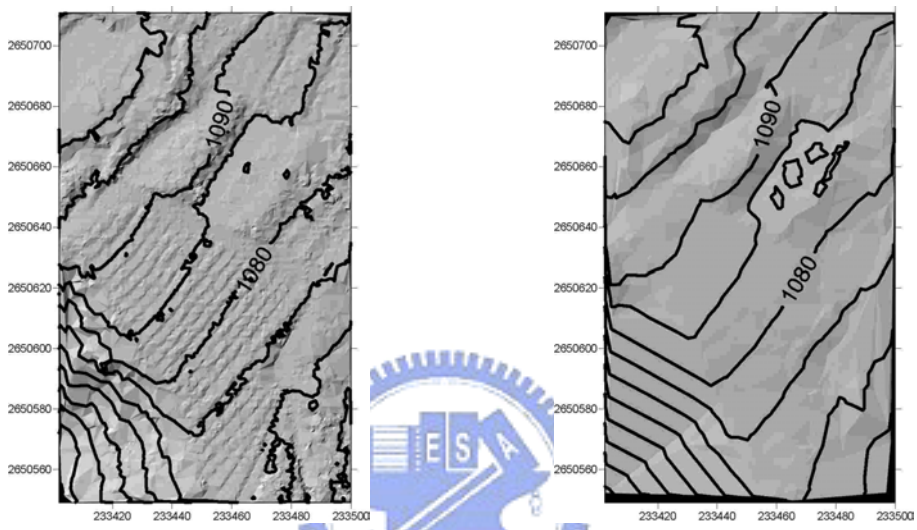


(a) H = 1100 m dataset (b) H = 1800 m dataset

Figure 4.3. Comparison of shaded relief maps for tea farm A.

(average slope 22 degree)

## 4.5 Verifying the distribution of checkpoints

An experimental strategy for arranging checkpoints is required in order to consider any possible interaction between the error factors. Table 4.6 presents the checkpoints distribution by slope class and vegetation angle. The sampling is designed to have sufficient number of checkpoints for each category, in order to avoid the influence of land-cover factor on the elevation accuracy assessment.

Table 4.6 Number of checkpoints by slope class and vegetation angle

| Vegetation angle | Slope | | | Total count |
|---|---|---|---|---|
| | 0° – 6° | 6° – 25° | > 25° | |
| 0° – 20° | 144 | 337 | 153 | 634 |
| 20° – 30° | 41 | 101 | 50 | 192 |
| > 30° | 28 | 41 | 11 | 80 |
| Total count | 213 | 479 | 214 | 906 |

## 4.6 Assessing errors using checkpoints

The 'difference' or elevation error for each checkpoint is computed by subtracting the surveyed elevation of the checkpoint from the filtered LIDAR dataset elevation interpolated at the x/y coordinate of the checkpoint. The interpolation method is the Delaunay triangulation with linear interpolation. LIDAR-derived elevation was converted into triangulated irregular networks. Differences were obtained by subtracting the reference elevation from the LIDAR elevation:

$$\text{Elevation Error}_{(i)} = \text{LIDAR-derived Elevation}_{(i)} - \text{Reference Elevation}_{(i)} \quad (4.6)$$

Positive values reveal overestimates of the actual surface height. The error analysis uses all checkpoint errors to compute the accuracy statistics. Because a large error (outlier) can skew RMSE calculations of checkpoints, the best 95 percent elevation errors were also used for the 95 percent statistics calculation. The procedure for error assessment in three steps:

(1) Checking whether the mean signed error from the expected central tendency is

zero. When the mean error is large, a bias or systematic error may be present;

(2) Checking whether the skewness exceeds ±0.5 to determine whether the errors follow a normal distribution. Skewness can also be detected by comparing the mean and median. When the mean is greater than median, the distribution is positively skewed;

(3) Analyzing the histogram of errors, particularly positive errors (overestimates) and checking whether the distribution has a bimodal phenomenon, to judge whether the filtering process retains un-cleaned artifacts.

This section evaluated the LIDAR-derived TINs using the Terrascan software for the automated filtering. The accuracy of LIDAR-derived TINs is summarized in Table 4.7 and Table 4.8. The best 95% of the checkpoint errors demonstrate that the overall mean signed error for H = 1100 m dataset is -0.3 cm, and that for H = 1800 m dataset is -5.9 cm. As expected, H = 1100 m dataset involving a lower flight height was associated with a lower overall 16.3 cm RMSE, while H = 1800 m dataset involving higher flight height had a larger 25.8 cm RMSE. Cross-reference of both datasets reveals a difference in RMSE of 27.6 cm and a mean signed error of +6.0 cm. The standard deviation of differences describes random error. The standard deviation of differences in each land-cover type for H = 1100 m dataset is considerably smaller than 15 cm, except in the area of sloped tea farm A (17.2 cm).

Table 4.7 Accuracy of terrain model for H = 1100 m dataset (error in cm)

| | Pavement | Occlusion path | Landslide rock | Wet soil | Orchard | Sloped tea farm A | Tea farm B | Total |
|---|---|---|---|---|---|---|---|---|
| 95% # of points | 130 | 78 | 330 | 82 | 119 | 44 | 78 | 861 |
| 95% RMSE | 8.2 | 19.4 | 15.5 | 13.9 | 15.2 | 31.3 | 15.9 | 16.3 |
| 95% MAE | 6.4 | 17.9 | 12.7 | 11.8 | 12.0 | 26.4 | 13.6 | 13.0 |
| 95% Mean error | -1.4 | ***-17.9*** | 11.3 | -10.2 | 4.4 | ***-26.3*** | -4.8 | -0.3 |
| 95% Median | -0.6 | -17.4 | 10.8 | -11.6 | 1.1 | -26.0 | -7.7 | 0.4 |
| 95% Skew | -0.310 | -0.299 | +0.069 | +0.272 | +0.477 | -0.253 | ***+0.871*** | -0.304 |
| 95% Std Dev | 8.1 | 7.5 | 10.7 | 9.5 | 14.6 | 17.2 | 15.2 | 16.3 |
| 95% Min | -20.1 | -34.6 | -17.5 | -26.2 | -19.3 | -59.8 | -32.3 | -59.8 |
| 95% Max | 14.1 | -4.2 | 36.5 | 9.9 | 36.4 | 1.4 | 34.5 | 36.5 |
| | | | | | | | | |
| 100% # of points | 137 | 82 | 348 | 86 | 125 | 46 | 82 | 906 |
| 100% RMSE | 9.2 | 20.2 | 17.7 | 14.5 | 16.4 | 32.7 | 19.9 | 18.0 |
| 100% MAE | 7.1 | 18.3 | 14.0 | 12.2 | 13.0 | 27.2 | 15.5 | 14.0 |
| 100% Mean error | -1.7 | ***-18.1*** | 11.1 | -10.2 | 4.5 | ***-26.5*** | -4.0 | +0.3 |
| 100% Skew | -0.428 | -0.330 | -0.451 | +0.173 | +0.437 | -0.303 | ***+1.516*** | -0.087 |
| 100% Std Dev | 9.1 | 9.0 | 13.8 | 10.4 | 15.9 | 19.4 | 19.6 | 17.8 |
| 100% Min | -28.4 | -45.1 | -66.5 | -36.3 | -25.9 | -75.9 | -43.5 | -75.9 |
| 100% Max | 14.8 | 8.7 | 54.8 | 11.6 | 40.7 | 15.2 | 85.1 | 85.1 |

Table 4.8 Accuracy of terrain model for H = 1800 m dataset (error in cm)

| | Pavement | Occlusion path | Landslide rock | Wet soil | Sloped tea farm A | Tea farm B | Total | H=1100m — H=1800m |
|---|---|---|---|---|---|---|---|---|
| 95% # of points | 130 | 78 | 330 | 82 | 44 | 78 | 742 | 742 |
| 95% RMSE | 11.7 | 18.3 | 25.8 | 20.3 | 37.6 | 40.0 | 25.8 | 27.6 |
| 95% MAE | 9.9 | 14.3 | 22.6 | 18.4 | 27.2 | 32.7 | 20.5 | 22.6 |
| 95% Mean error | -4.6 | -6.8 | ***-15.7*** | ***-18.4*** | ***25.8*** | ***29.3*** | -5.9 | 6.0 |
| 95% Median | -5.7 | -4.7 | -19.4 | -17.2 | 18.5 | 29.2 | -9.7 | 9.4 |
| 95% Skew | +0.119 | -0.140 | ***+0.650*** | -0.463 | ***+1.072*** | ***+0.555*** | ***+1.207*** | -0.457 |
| 95% Std Dev | 10.8 | 17.1 | 20.4 | 8.6 | 27.7 | 27.5 | 25.1 | 26.9 |
| 95% Min | -36.3 | -40.6 | -54.6 | -37.9 | -16.2 | -43.4 | -54.6 | -63.3 |
| 95% Max | 17.3 | 31.3 | 37.7 | -4.9 | 93.5 | 123.5 | 123.5 | 56.7 |
| | | | | | | | | |
| 100% # of points | 137 | 82 | 348 | 86 | 46 | 82 | 781 | 781 |
| 100% RMSE | 14.0 | 21.0 | 28.4 | 20.7 | 40.2 | 47.0 | 28.6 | 32.3 |
| 100% MAE | 11.2 | 16.0 | 24.4 | 18.5 | 29.0 | 36.7 | 22.1 | 25.4 |
| 100% Mean error | -5.3 | -6.3 | ***-15.1*** | ***-18.5*** | ***26.3*** | ***29.2*** | -5.7 | 5.4 |
| 100% Skew | ***+0.553*** | +0.339 | ***+0.804*** | -0.411 | ***+0.974*** | +0.179 | ***+1.183*** | ***-0.620*** |
| 100% Std Dev | 13.0 | 20.2 | 24.1 | 9.4 | 30.8 | 37.1 | 28.0 | 31.9 |
| 100% Min | -50.4 | -47.5 | -76.1 | -40.4 | -29.6 | -88.5 | -88.5 | -118.7 |
| 100% Max | 21.2 | 60.7 | 82.5 | 1.0 | 106.4 | 157.0 | 157.0 | 105.7 |

Table 4.9 presents mean signed errors of over ±15 cm in italics, including those of the occlusion path area and the tea farm A for H = 1100 m dataset. The mean signed errors of over ±15 cm were in the areas of landslide rock, wet soil, tea farm A, and tea farm B for H = 1800 m dataset.

Table 4.9 Mean signed error

| Evaluation area | Mean of signed error in cm | | | | | | |
|---|---|---|---|---|---|---|---|
| | Pavement | Landslide rock | Wet soil | Orchard | Tea farm A | Tea farm B | Occlusion path |
| H = 1100 m | -1.4 | +11.3 | -10.2 | +4.4 | ***-26.3*** | -4.8 | ***-17.9*** |
| H = 1800 m | -4.6 | ***-15.7*** | ***-18.4*** | No data | ***+25.8*** | ***+29.3*** | -6.8 |

The skewness exceeds ±0.5 in area of tea farm B for H = 1100 m dataset and areas of landslide rock, tea farm A and tea farm B for H = 1800 m dataset (Table 4.10).

Table 4.10 Checking the skewness

| Evaluation area | Skewness | | | | | | |
|---|---|---|---|---|---|---|---|
| | Pavement | Landslide rock | Wet soil | Orchard | Tea farm A | Tea farm B | Occlusion path |
| H = 1100 m | -0.310 | +0.069 | +0.272 | +0.477 | -0.253 | ***+0.871*** | -0.299 |
| H = 1800 m | +0.119 | ***+0.650*** | -0.463 | No data | ***+1.072*** | ***+0.555*** | -0.140 |

## 4.7 Elevation error and vegetation type

### 1. Elevation error and land-cover class

Table 4.11 summarizes the MAE for each land-cover class. For both datasets,

the mean absolute errors significantly differed ($p$-value 0.001 < 0.05 significance level) between land-cover types. Figure 4.4 shows the MAE for various land-cover types. The mean absolute errors of H = 1100 m dataset for each land-cover class, except area of occlusion path, are smaller than those of H = 1800 m. The MAE of H = 1100 m dataset is considerably smaller than 15 cm, except in areas of occlusion path and tea farm A. For H = 1100 m dataset, with the steep slope of 25 degree, the landslide rock site has elevation errors less than 15 cm. The heavily vegetated sites such as orchard and tea farm B are also within 15 cm.

Table 4.11 Elevation error by land-cover class (error in cm)

| | Evaluation area | | | | | | | | | |
|---|---|---|---|---|---|---|---|---|---|---|
| | Pavement | Occlusion path | Landslide rock | Wet soil | Orchard | Tea farm A | Tea farm B | Total | *F*-value | *p*-value |
| Count of H=1100m | 130 | 78 | 330 | 82 | 119 | 44 | 78 | 861 | | |
| MAE of H=1100m | 6.4 | 17.9 | 12.7 | 11.8 | 12.0 | 26.4 | 13.6 | 12.8 | 33.593 | <0.001 |
| Count of H=1800m | 130 | 78 | 330 | 82 | na | 44 | 78 | 742 | | |
| MAE of H=1800m | 9.9 | 14.3 | 22.6 | 18.4 | na | 27.2 | 32.7 | 20.4 | 33.964 | <0.001 |

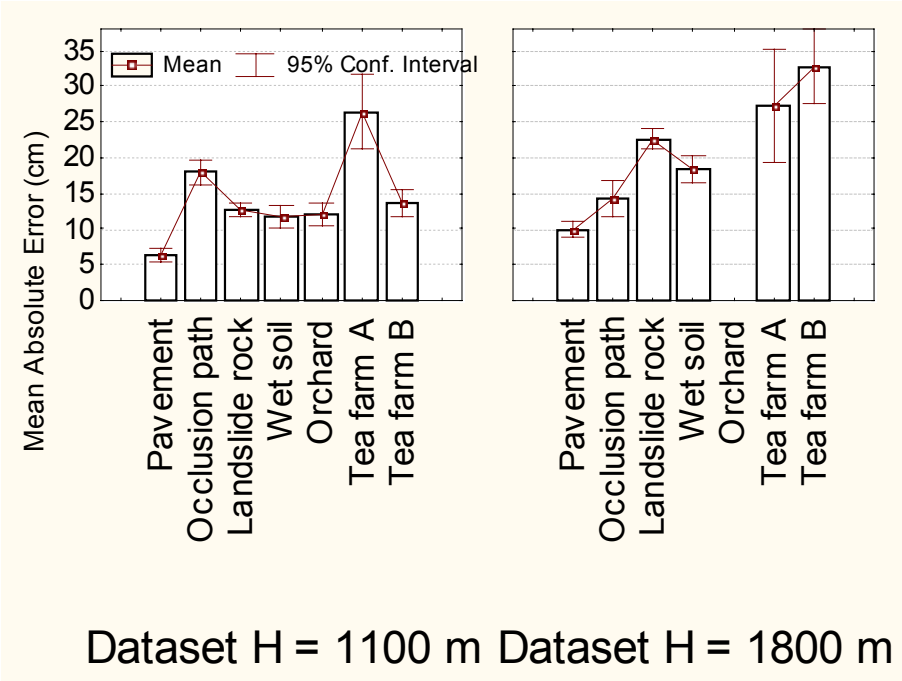


Figure 4.4. MAE error of both datasets, using various types of land-cover.

## 2. Elevation error and canopy volume

As previously discussed, the H = 1100 m dataset gives better results than H = 1800 m. The better dataset (H = 1100 m) was used to derive reference canopy volume and vegetation angle. Classes of different canopy volume and vegetation angle were generated. The canopy volume derived from H = 1100 m is used as a reference canopy volume to evaluate the effect of vegetation type on elevation error. For both datasets, the mean absolute errors significantly differed (both *p*-value 0.001 < 0.05 level of significance) between classes. The elevation errors vary with canopy volume. Figure 4.5 reveals that elevation error is positively correlated with canopy volume. A greater canopy volume implies a greater elevation error. For H = 1100 m, when the canopy volume was less than 0.2 ($m^3$/sq m), the MAE did not exceed 15 cm. For H = 1800 m dataset, the worst case (MAE 27.4 cm) was for canopy volume between 0.3 and 0.5 ($m^3$/sq m). However, the MAE of H = 1800 m dropped sharply

to 15.3 cm when the canopy volume exceeded 1.0 ($m^3$/sq m) because the filtering process in H = 1800 m dataset was cleaner when the trees were taller and the canopy volume exceeded 1.0 ($m^3$/sq m) (Table 4.12).

Table 4.12 Elevation error related to vegetation type by reference canopy volume

| | Canopy volume ($m^3$/sq m) | | | | | | | | |
|---|---|---|---|---|---|---|---|---|---|
| | 0-0.1 | 0.1-0.2 | 0.2-0.3 | 0.3-0.5 | 0.5-1.0 | >1.0 | Total | *F* | *p*-value |
| Count of H=1100m | 419 | 126 | 71 | 46 | 31 | 88 | 781 | | |
| Average ($m^3$/sq m) | 0.04 | 0.15 | 0.25 | 0.36 | 0.66 | 2.60 | 0.41 | | |
| MAE of H=1100m (cm) | 12.0 | 14.0 | 17.9 | 15.7 | 17.5 | 18.1 | 14.0 | 7.686 | <0.001 |
| MAE of H=1800m (cm) | 22.2 | 22.5 | 24.4 | 27.4 | 26.3 | 15.3 | 22.1 | 3.975 | <0.001 |

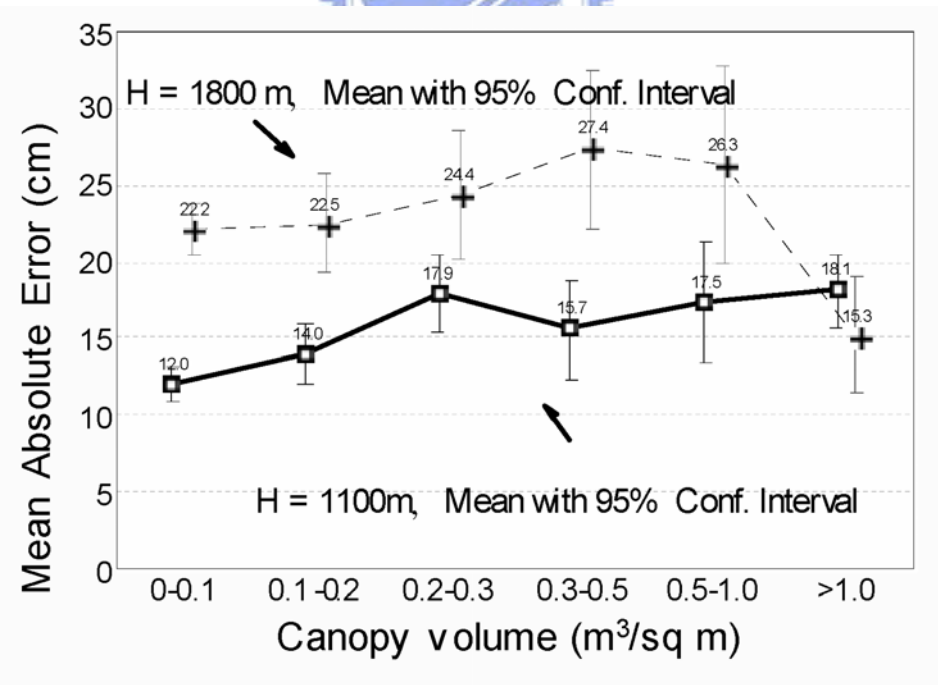


Figure 4.5. Elevation error as a function of canopy volume.

## 3. Elevation error and local roughness of point clouds

Table 4.13 presents the relationship between the elevation errors and the local roughness of point clouds. For both datasets, the MAE was significantly different ($p$-value < 0.05 significance level) between local roughness classes. This indicates that the elevation errors are associated with the local roughness of points. Figure 4.6 plots the relationship between elevation error and the local roughness. A larger local roughness indicates greater elevation error. For H = 1100 m dataset, when the local roughness was less than 25 cm, the MAE of the elevation did not exceed 15 cm.

Table 4.13 The elevation error and local roughness on checkpoints

| | Local roughness (cm) | | | | | | | | |
|---|---|---|---|---|---|---|---|---|---|
| | 0-10 | 10-15 | 15-20 | 20-25 | 25-35 | >35 | Total | *F* | *p*-value |
| Count of H = 1100 m | 364 | 121 | 85 | 61 | 61 | 89 | 781 | | |
| MAE of H=1100m (cm) | 13.0 | 13.1 | 13.2 | 14.4 | 17.0 | 17.7 | 14.0 | 3.703 | 0.003 |
| Count of H = 1800 m | 172 | 90 | 80 | 75 | 115 | 249 | 781 | | |
| MAE of H=1800m (cm) | 18.0 | 19.1 | 21.1 | 25.6 | 23.9 | 24.6 | 22.1 | 4.167 | 0.001 |

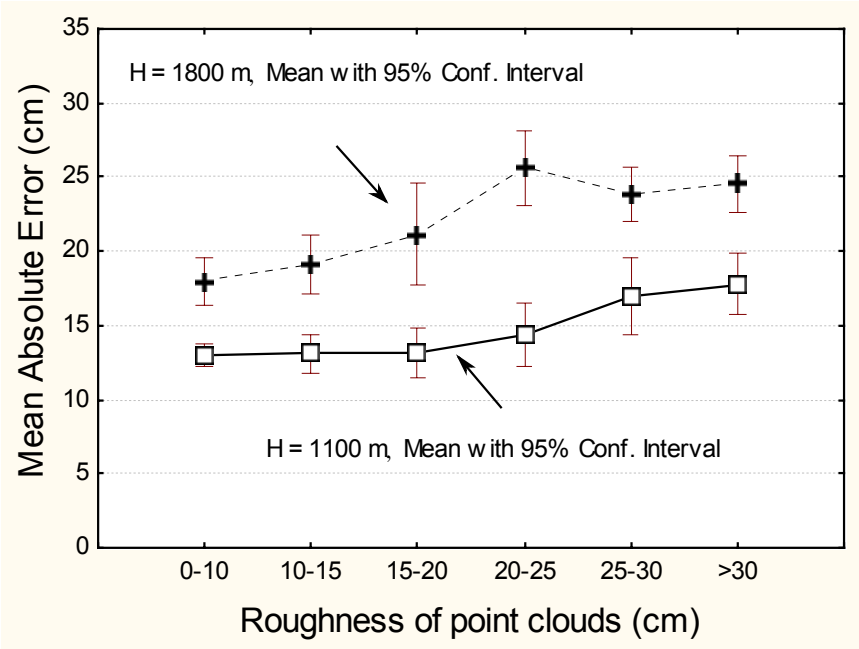


Figure 4.6. Elevation error as a function of local roughness on checkpoints.

## 4. Elevation error and vegetation angle

The vegetation angle obtained from H = 1100 m is used as a reference one to evaluate the impact of vegetation type on the elevation error. For H = 1100 m, the MAE was significantly different (*p*-value < 0.05 significance level) between vegetation angle classes (Table 4.14). For H = 1800 m dataset, the MAE was also

different significantly. Figure 4.7 shows a linear relationship between the vegetation angle and the MAE. The determination coefficient of regression $r^2$ is 0.95 for H = 1100 m (Table 4.15). A greater vegetation angle implies greater elevation error.

Table 4.14 Relationship between elevation error and vegetation angle

| | Vegetation angle (degree) | | | | | |
|---|---|---|---|---|---|---|
| | 0~20 | 20~30 | 30~90 | Total | $F$ | $p$-value |
| Count of H = 1100 m | 544 | 158 | 79 | 781 | | |
| Average (degree) | 11.5 | 23.9 | 40.8 | 73.0 | | |
| MAE of H = 1100 m (cm) | 11.7 | 18.0 | 21.9 | 14.0 | 45.107 | <0.001 |
| MAE of H = 1800 m (cm) | 21.2 | 24.2 | 24.6 | 22.1 | 2.536 | 0.080 |

Table 4.15 Regression of elevation error and vegetation angle

| Dataset | Intercept $\beta_0$ | Regression coefficient $\beta_1$ | Std. Err of $\beta_0$ | Std. Err of $\beta_1$ | $p$-value of $\beta_0$ | $p$-value of $\beta_1$ | Correlation Coefficient $r$ | Coefficient of Determination $r^2$ |
|---|---|---|---|---|---|---|---|---|
| H=1100m | 8.532 | 0.341 | 2.179 | 0.078 | 0.159 | 0.142 | 0.975 | 0.951 |
| H=1800m | 20.523 | 0.111 | 1.715 | 0.061 | 0.053 | 0.321 | 0.876 | 0.767 |

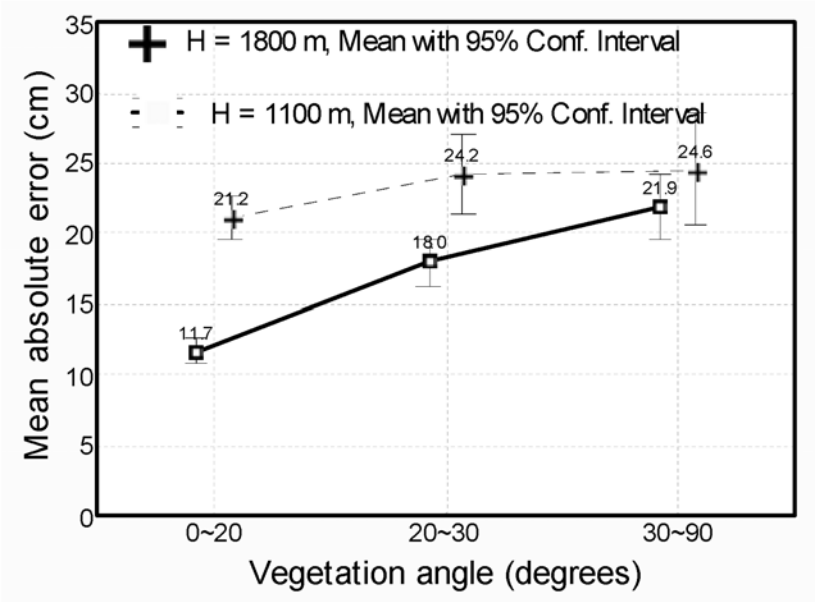


Figure 4.7. Elevation error as a function of vegetation angle.

## 4.8 Elevation error and point spacing of LIDAR ground returns

Table 4.16 shows the effect of point spacing of LIDAR ground returns on elevation error for the two datasets. The MAE was significantly different for both datasets ($p$-value < 0.05 significance level) between the classes of the mean distance to the nearest LIDAR point.

Figure 4.8 reveals that the elevation errors of H = 1100 m are lower than those of H = 1800 m in all classes. The mean distance to the nearest LIDAR point is linearly correlated to the elevation error. The determination coefficients of regression $r^2$ exceed 0.9 for both plots (Table 4.17). A larger mean distance to the nearest LIDAR point implies greater elevation error.

Table 4.16 Elevation error and mean distance to the nearest LIDAR point

| | Mean distance to nearest LIDAR point | | | | | |
|---|---|---|---|---|---|---|
| | 0-0.4 m | 0.4-0.8 m | >0.8 m | Total | *F* | *p*-value |
| Count of H = 1100 m | 319 | 417 | 45 | 781 | | |
| Average (m) | 0.27 | 0.56 | 0.90 | 0.46 | | |
| MAE of H = 1100 m (cm) | 12.7 | 14.5 | 18.6 | 14.0 | 6.417 | 0.002 |
| Count of H = 1800 m | 160 | 412 | 209 | 781 | | |
| Average (m) | 0.30 | 0.60 | 0.95 | 0.63 | | |
| MAE of H = 1800 m (cm) | 16.3 | 22.7 | 25.5 | 22.1 | 12.468 | <0.001 |

Table 4.17 Regression of elevation error and mean distance to the nearest LIDAR point

| | Intercept $\beta_0$ | Regression coefficient $\beta_1$ | Std. Err of $\beta_0$ | Std. Err of $\beta_1$ | *p*-value of $\beta_0$ | *p* -value of $\beta_1$ | Correlation Coefficient *r* | Coefficient of Determination $r^2$ |
|---|---|---|---|---|---|---|---|---|
| H=1100m | 9.74 | 9.51 | 0.697 | 1.175 | 0.005 | 0.015 | 0.985 | 0.970 |
| H=1800m | 12.97 | 14.00 | 1.822 | 2.755 | 0.019 | 0.037 | 0.963 | 0.928 |

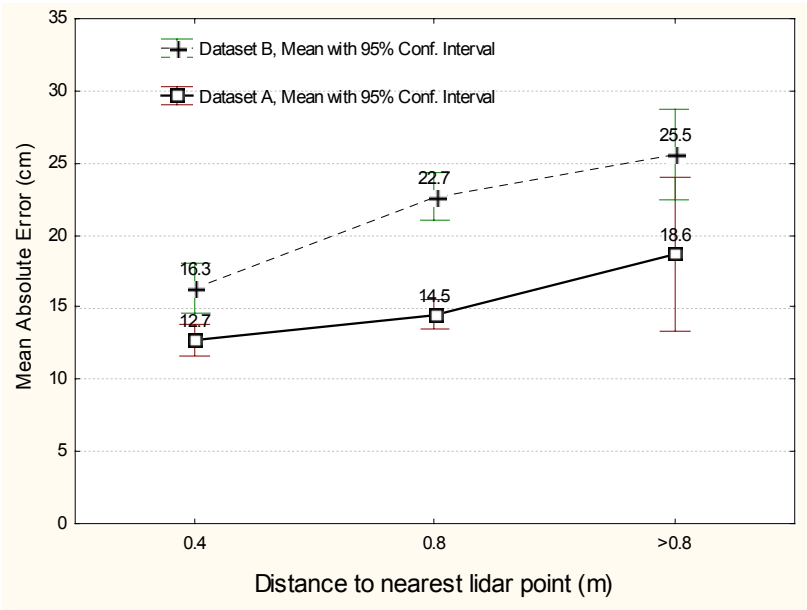


Figure 4.8. Elevation error as a function of the mean distance to the nearest LIDAR point.

## 4.9 The combination effect of vegetation angle and point spacing

As noted previously, Figure 4.7 plots the relationship between the vegetation angle and elevation error. Notably, the two lines of the two datasets are not parallel (Figure 4.7). The different dataset and the magnitude of vegetation angle have a profound impact on the elevation error.

This section considers the interaction effect between the elevation angle and the point spacing of the ground returns. Table 4.18 shows that, according to the product of the mean distance to the nearest LIDAR point and the tangent of the vegetation angle, MAE significantly differed (both $p$-value < 0.05 significance level). As shown in Figure 4.9, the two lines of the linear regression are approximately parallel, indicating an absence of interaction effect for the combined factors. The determination coefficients of regression $r^2$ exceed 0.9 for both datasets (Table 4.19).

The elevation error is a function of the combination of vegetation angle and the

point spacing of the ground returns. The point spacing of the ground returns compensates the effect of the vegetation type (vegetation angle) on the elevation error.

Table 4.18 Relationship between elevation error and the product of distance to nearest LIDAR point and the tangent of the elevation angle

| | Nearest distance × tan (vegetation angle) | | | | | |
|---|---|---|---|---|---|---|
| | 0-0.146 | 0.146-0.291 | >0.291 | Total | *F* | *p*-value |
| Count of H = 1100 m | 506 | 193 | 82 | 781 | | |
| Average | 0.0773 | 0.2035 | 0.5289 | 0.1559 | | |
| MAE of H=1100m (cm) | 11.7 | 16.8 | 21.8 | 14.0 | 39.695 | <0.001 |
| Count of H = 1800 m | 423 | 216 | 142 | 781 | | |
| Average | 0.0725 | 0.2073 | 0.5827 | 0.2025 | | |
| MAE of H=1800m (cm) | 19.2 | 21.9 | 30.5 | 22.1 | 21.089 | <0.001 |

Table 4.19 Regression of elevation error and the product of distance to nearest LIDAR point and the tangent of the elevation angle

| Dataset | Intercept $\beta_0$ | Regression coefficient $\beta_1$ | Std. Err of $\beta_0$ | Std. Err of $\beta_1$ | *p*-value of $\beta_0$ | *p*-value of $\beta_1$ | Correlation Coefficient $r$ | Coefficient of Determination $r^2$ |
|---|---|---|---|---|---|---|---|---|
| H=1100m | 11.11 | 20.97 | 1.81 | 5.47 | 0.103 | 0.162 | 0.968 | 0.936 |
| H=1800m | 17.45 | 22.31 | 0.22 | 0.60 | 0.008 | 0.017 | 0.999 | 0.999 |

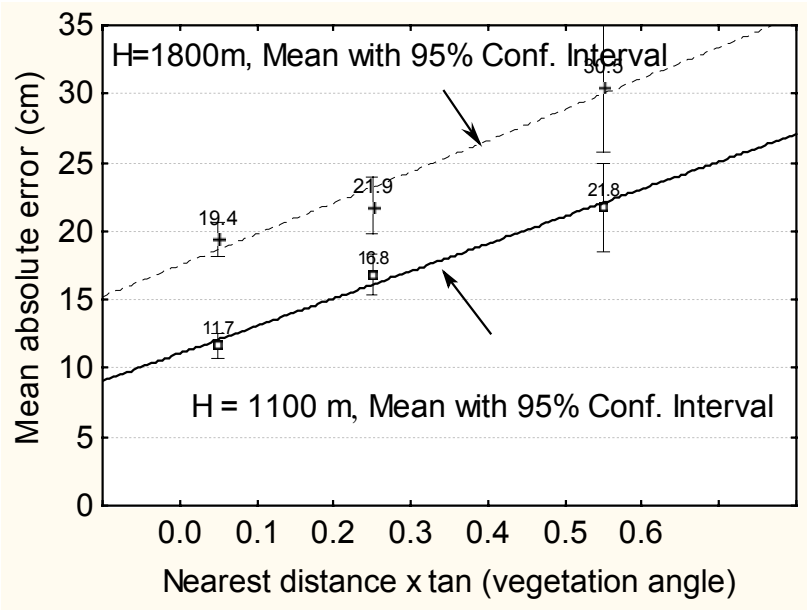


Figure 4.9. Elevation error as a function of the product of the mean distance to nearest LIDAR point and the tangent of the vegetation angle.

## 4.10 Elevation error and terrain form

### 1. Elevation error and slope

The slope derived from H = 1100 m is used as the reference slope to evaluate the impact of terrain slope on elevation error. The MAE was significantly different for both datasets (both $p$-value < 0.05 significance level) between slope classes (Table 4.20). Figure 4.10 demonstrates that the slope is linearly correlated to the elevation error. The determination coefficients of regression $r^2$ exceed 0.9 for both plots (Table 4.21). The mean absolute error increases with the terrain slope. For H = 1100 m, when the slope was less than 25°, the MAE did not exceed 15 cm.

Table 4.20 Elevation error by reference slope

| | Slope (in degrees) | | | | | |
|---|---|---|---|---|---|---|
| | 0-6 | 6-25 | >25 | Total | $F$ | $p$ -value |
| Count of H = 1100 m | 159 | 411 | 211 | 781 | | |
| Average slope of H = 1100 m | 3.78 | 14.79 | 31.84 | 17.15 | | |
| MAE of H = 1100 m (cm) | 12.2 | 13.5 | 16.3 | 14.0 | 6.720 | 0.001 |
| MAE of H = 1800 m (cm) | 16.6 | 22.1 | 26.4 | 22.1 | 14.046 | <0.001 |

Table 4.21 Regression of elevation error and slope

| Dataset | Intercept $\beta_0$ | Regression coefficient $\beta_1$ | Std. Err of $\beta_0$ | Std. Err of $\beta_1$ | $p$-value of $\beta_0$ | $p$-value of $\beta_1$ | Correlation Coefficient $r$ | Coefficient of Determination $r^2$ |
|---|---|---|---|---|---|---|---|---|
| H=1100m | 11.519 | 0.148 | 0.255 | 0.013 | 0.014 | 0.053 | 0.996 | 0.993 |
| H=1800m | 15.971 | 0.341 | 1.367 | 0.067 | 0.054 | 0.124 | 0.981 | 0.963 |

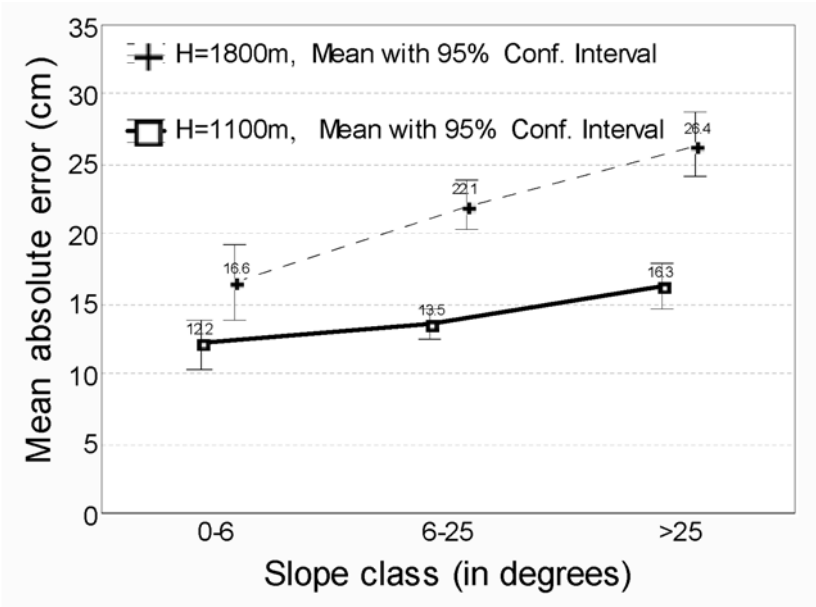


Figure 4.10. Elevation error as a function of slope.

## 2. Elevation error and the combination of slope and point spacing

This section considers the interaction effect between the slope and point spacing of ground returns. Table 4.22 shows that, the product between the mean distance to the nearest LIDAR point and the tangent of slope demonstrates that MAE significantly differs for both datasets (both $p$-value < 0.05 significance level).

As shown in Figure 4.11, the two lines of the linear regression are approximately parallel, indicating an absence of interaction effect for the combined factors. The determination coefficient of regression $r^2$ is 0.98 for H = 1100 m (Table 4.23). The elevation error is a function of the combination of slope and the point spacing of the ground returns. The point spacing of ground returns compensates the effect of the terrain slope on the elevation error.

Table 4.22 Relationship between elevation error and the product of the mean distance to the nearest LIDAR point and the tangent of the slope

| | Nearest distance × tan(slope) | | | | | Total | $F$ | $p$-value |
|---|---|---|---|---|---|---|---|---|
| | 0~ 0.042 | 0.042~ 0.084 | 0.084~ 0.187 | 0.187~ 0.373 | >0.373 | | | |
| Count of H = 1100 m | 161 | 141 | 235 | 194 | 50 | 781 | | |
| Average | 0.024 | 0.061 | 0.128 | 0.254 | 0.465 | 0.147 | | |
| MAE of H=1100m (cm) | 11.2 | 12.2 | 13.6 | 15.7 | 23.3 | 14.0 | 13.674 | <0.001 |
| Count of H = 1800 m | 165 | 124 | 159 | 246 | 87 | 781 | | |
| Average | 0.022 | 0.059 | 0.134 | 0.272 | 0.498 | 0.183 | | |
| MAE of H=1800m (cm) | 16.5 | 16.0 | 22.0 | 26.8 | 28.8 | 22.1 | 15.715 | <0.001 |

Table 4.23 Regression of elevation error and the product of the mean distance to the nearest LIDAR point and the tangent of the slope

| Dataset | Intercept $\beta_0$ | Regression coefficient $\beta_1$ | Std. Err of $\beta_0$ | Std. Err of $\beta_1$ | $p$-value of $\beta_0$ | $p$-value of $\beta_1$ | Correlation Coefficient $r$ | Coefficient of Determination $r^2$ |
|---|---|---|---|---|---|---|---|---|
| H=1100m | 10.22 | 26.70 | 0.61 | 2.49 | <0.001 | 0.002 | 0.987 | 0.975 |
| H=1800m | 16.50 | 28.01 | 1.66 | 6.32 | 0.002 | 0.021 | 0.931 | 0.867 |

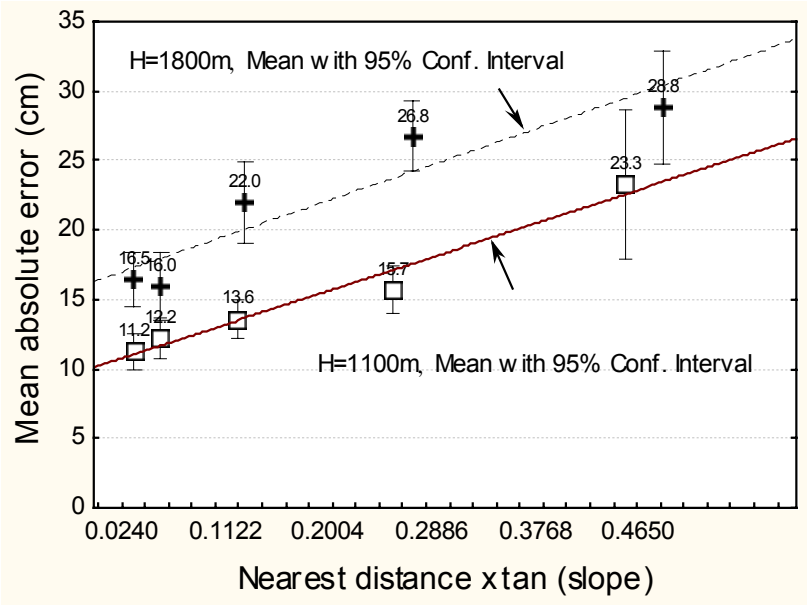


Figure 4.11. Elevation error as a function of product of the mean distance to the nearest LIDAR point and the tangent of the slope.

## 3. Elevation error and aspect

The terrain aspect obtained from the better dataset (H = 1100 m) is used as the reference terrain aspect in evaluating the elevation error. For H = 1800 m dataset, the MAE was significantly different ($p$-value < 0.05 significance level) between aspect classes. For H = 1100 m without cross-flight data, the MAE was significantly different ($p$-value < 0.05 significance level). Notably, for H = 1100 m with cross-flight data, MAE was not significantly different ($p$-value of 0.607, Table 4.24, Figure 4.12). As a consequence of the characteristics of sampling pattern and viewing direction, H = 1100 m dataset with extra cross-flight data may reduce the effect of terrain aspect on the elevation accuracy.

Table 4.24 Elevation error by aspect class

| | Aspect | | | | | | | | | | |
|---|---|---|---|---|---|---|---|---|---|---|---|
| | N | NE | E | SE | S | SW | W | NW | Total | *F* | *p*-value |
| Count of H = 1100 m | 33 | 90 | 190 | 280 | 90 | 46 | 25 | 27 | 781 | | |
| MAE of H = 1100 m (cm) with cross-flight data | 11.7 | 12.9 | 14.0 | 14.3 | 15.0 | 14.9 | 11.0 | 15.3 | 14.0 | 0.777 | 0.607 |
| MAE of H = 1100 m (cm) without cross-flight data | 12.0 | 13.9 | 17.5 | 17.6 | 14.1 | 14.7 | 12.9 | 17.5 | 16.2 | 2.454 | 0.017 |
| MAE of H = 1800 m (cm) | 16.9 | 23.8 | 19.2 | 23.2 | 21.0 | 26.6 | 16.4 | 34.6 | 22.1 | 12.325 | <0.001 |

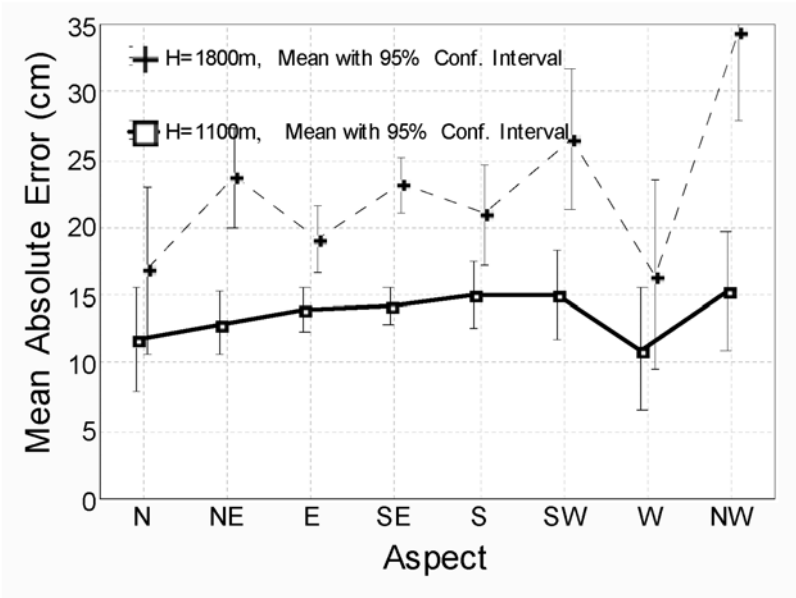


(a) H = 1100 m with cross-flight data, H = 1800 m without cross-flight data

Figure 4.12. Mean absolute error as a function of terrain aspect, comparing H = 1800 m with H = 1100 m

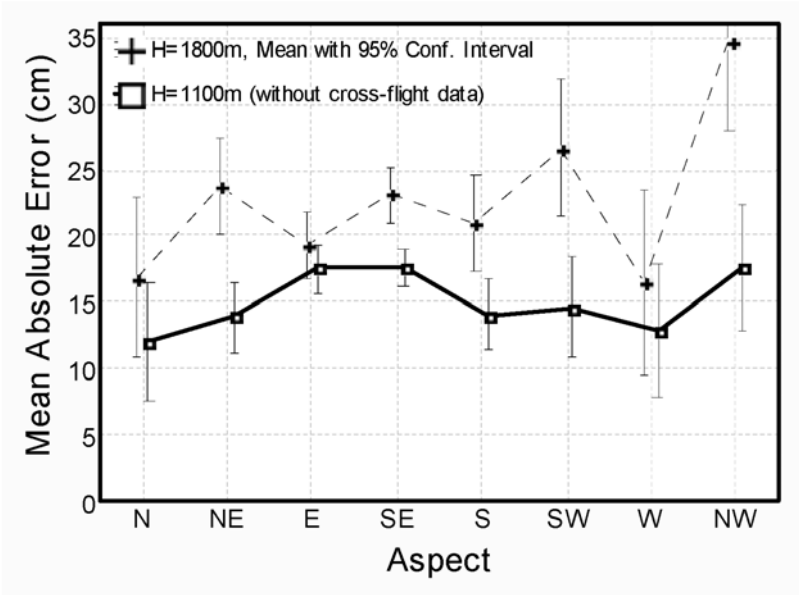


(b) Without cross-flight data

Figure 4.12. Mean absolute error as a function of terrain aspect, comparing H = 1800 m with H = 1100 m

## 4.11 Comparisons between photogrammetry and LIDAR

In order to assure the quality of LIDAR-derived elevation data, a global comparison was conducted by evaluating the consistency of LIDAR- and photogrammetry-derived digital elevation data. The differences in data acquisition by photogrammetry and by laser scanning are as follows:

* Stereo-image-based photogrammetric techniques require that points be visible in two overlapping aerial photos during data acquisition. However, Airborne LIDAR technology merely requires one-directional laser signal with reflected

return to measure topographic elevation.

* In some forested areas, some laser pulses of LIDAR are able to penetrate forests to measure ground surface. On the other hand, only a small number of the rays of aerial photography reach the terrain in a forest where the ground is covered with very dark shadows. With aerial cameras, typically a wide-angle lens (75° FOV) is used, while the operation of laser scanning is more flexible, as the scan angle can be changed depending on the collection plan. Typically a 20–40° scan angle is used. In addition, the typical FOV of laser scanning is smaller than that of aerial cameras, with the result that laser scanning is less restricted by occlusions than photogrammetric techniques in forested areas.
* Aerial photography is influenced by weather conditions, sunlight, misty atmosphere, and so on. However, laser scanning is less restricted by weather conditions and, in principle, allows data collection during daytime and nighttime.
* Aerial photography obtains images and 3D elevation data at the same time. However, laser scanning generally generates digital elevation data. Laser signals do not reflect on water surface. Therefore, it is more appropriate to apply photogrammetric techniques to determine the water boundaries.

***1. Aerial Photography***

The aerial photographs were taken on September 2002, using a Zeiss RMK aerial camera with a 153.594 mm lens. The flying altitude for the photography was 800 m above the ground, resulting in a photo scale of 1:5000. The photographs were scanned at 12.5 $\mu$m resolution. The photogrammetric processing was conducted using the SOCET SET package. The bundle adjustment with standard deviation for the photo coordinates was $\pm$ 8.28 $\mu$m.

***2. Visual analysis***

Figure 4.13 displays the shaded relief map of three sets of DSM and DTM for visual comparisons in an area of occlusion path. Figure 4.13 (a) depicts the 1-meter spacing DSM derived by the automatic matching method. Figure 4.13 (c) and (e) depict the 1-meter spacing DSMs of H = 1100 m and H = 1800 respectively. The LIDAR DSM demonstrates fine texture and clearer terrain features. Roads and forest can be distinctly recognized in the shaded relief map of LIDAR data. On the other hand, the shaded relief map of photogrammetry-derived data is more obscure. The visual comparison of DTM (Figure 4.13b, d, f) between the two methods also reveals that the shaded relief map of LIDAR-derived DTM demonstrates richer fine texture than that of photogrammetry-derived DTM. Figure 4.13 (d) and (f) delineate details of terrain feature such as mountain ridges, drainages and small paths in forest, etc.

(a) Photogrammetry derived DSM

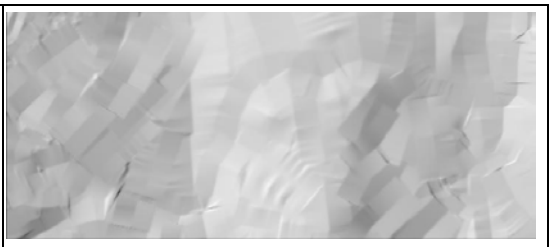

(b) Photogrammetry derived DEM

(c) DSM of H = 1100 m

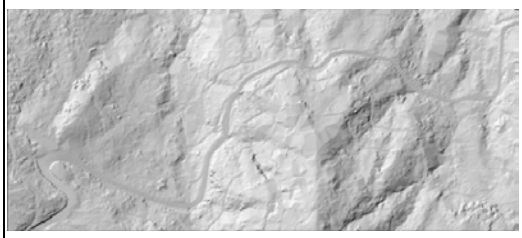

(d) DEM of H = 1100 m

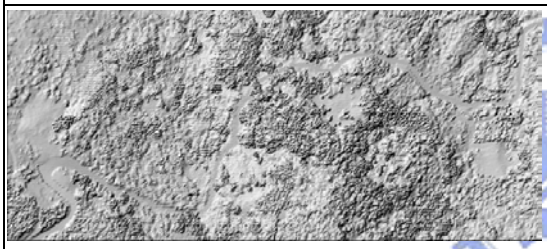

(e) DSM of H = 1800 m

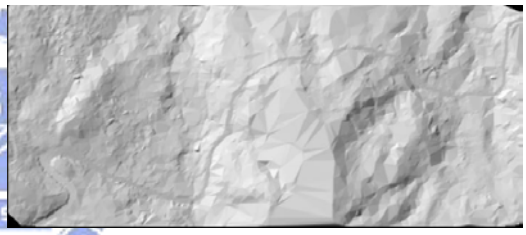

(f) DEM of H = 1800 m

Figure 4.13. Visual comparisons of shaded relief maps.

### *3. Contour analysis*

The contour maps were generated from DTM. Figure 4.14 displays the contour lines derived from photogrammetry and LIDAR data. Contour lines generated from photogrammetry DTM are smoother, while LIDAR-derived contour lines have sliver polygons and undesirable isolations.

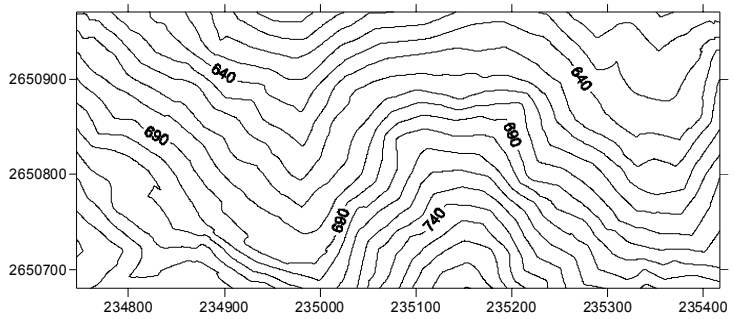


(a) Photogrammetry derived contour

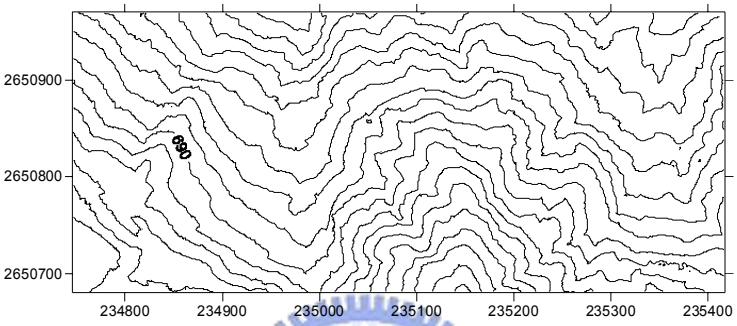


(b) H = 1100 m dataset

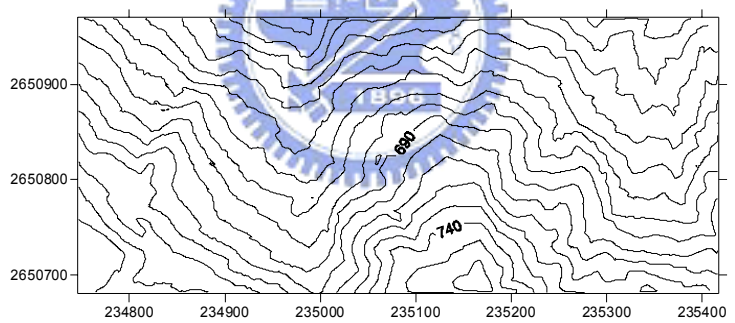


(c) H = 1800 m dataset

Figure 4.14. The comparisons of contours.

### *4. Quantitative comparison*

The 'difference' or elevation error for each checkpoint is computed by subtracting the surveyed elevation of the checkpoint from the photogrammetric DTM.

$$\text{Difference}_{(i)} = \text{photogrammetry-derived Elevation}_{(i)} - \text{Reference Elevation}_{(i)} \quad (4.7)$$

Photogrammetric DTM was automated by manual editing after matching and reduction of the DSM. The artifacts in photogrammetric DTM production method resulted from three sources: (1) manual editing, (2) automatic correlation, (3) interpolation induced elevation errors.

The artifacts to digital Photogrammetric approaches are the poor results of stereo matching in the area of dense vegetation resulting in inaccurate elevation values. We focus on the vegetation free area of landslide rock. The area of landslide rock is one of 25° slopes, without coverage of vegetation. It can be expected that due to little coverage of non-ground objects, DSM and DTM should be highly similar. The comparison of three sets of DSM is shown in Table 4.25. The difference between DSM of H = 1100 m and H = 1800 m results in MAE of 24.7 cm. The difference between DSM of photogrammetry and LIDAR data is greater in MAE of 30.8 cm.

To assess the additional amount of interpolation error introduced into photogrammetry-derived DTM, the elevation value at each ground checkpoint was measured by manual in stereo model and compared with elevation of ground checkpoint, as illustrated in Table 4.26. Not surprisingly, the highest MAE observed from the photogrammetry were over the area of sloped tea farm A (79.2 cm). The error of photogrammetric manual measuring is expected to have a significant impact on the observed elevations in steeper terrain and dense vegetation.

The accuracies for automated digital photogrammetry-derived DTMs are shown in Table 4.27. The pavement area was suitable for assessing the observed accuracy after an interpolation process on open terrain. The interpolation process resulted in increasing elevation error in the pavement area [increasing from 20.2 cm (in Table 4.26) to 21.4 cm (in Table 4.27) MAE].

The elevation error of DTM increasing from 25.7 cm (Table 4.26, manual

measurement) to 31.5 cm (Table 4.27, automated digital) in the landslide rock resulted from three sources: (1) manual editing, (2) automatic correlation, (3) interpolation induced elevation errors.

Figure 4.15 displays the comparisons of DTMs from LIDAR-derived (Table 3.7 to Table 3.10) vs. photogrammety-derived (Table 4.26). Figure 4.15 compares five DTM results: (1) LIDAR data of the H = 1100 m filtered from multiple-filtering technique, (2) LIDAR data of the H = 1100 m filtered from automatic processing with manual edits, (3) LIDAR data of the H = 1800 m filtered from multiple-filtering technique, (4) LIDAR data of the H = 1800 m filtered from automatic processing, (5) aerial photography with manual measurements in photogrammetric workstation.

Table 4.25 The differences of DSM in landslide rock (discrepancies between photogrammetry and LIDAR)

| DSM | MAE (cm) | Mean (cm) | Median (cm) | Std.Dev (cm) | Count | Min (cm) | Max (cm) |
|---|---|---|---|---|---|---|---|
| H=1100m – H=1800m | 24.7 | 13.6 | 15.1 | 27.2 | 8777100 | -68.1 | 79.2 |
| H=1100m – Photo | 30.8 | -24.5 | -21.5 | 31.9 | 8777100 | -136.4 | 52.1 |
| H=1800m – Photo | 44.1 | -38.2 | -37.9 | 37.1 | 8777100 | -151.2 | 64.6 |

Table 4.26 The accuracy of DTM by manual measurement in stereo-mode environment

| | 95% # of Points | 95% RMSE (cm) | 95% MAE (cm) | 95% Average (cm) | 95% Median (cm) | 95% Skew | 95% Std Dev (cm) | 95% Min (cm) | 95% Max (cm) | 100% # of Points | 100% RMSE (cm) | 100% MAE (cm) | 100% Min (cm) | 100% Max (cm) |
|---|---|---|---|---|---|---|---|---|---|---|---|---|---|---|
| Pavement | 130 | 24.3 | 20.2 | 16.8 | 17.6 | -0.056 | 17.6 | -17.9 | 56.3 | 137 | 25.7 | 21.2 | -32.2 | 63.5 |
| Occlusion path | 78 | 25.8 | 21.4 | 10.4 | 13.3 | -0.383 | 23.8 | -48.2 | 58.5 | 82 | 30.2 | 24.0 | -80.4 | 89.1 |
| Landslide rock | 330 | 30.0 | 25.7 | 24.7 | 24.5 | 0.010 | 17.0 | -14.3 | 63.4 | 348 | 32.0 | 26.9 | -41.9 | 91.0 |
| Wet soil | 82 | 39.6 | 37.5 | 37.5 | 37.6 | -0.191 | 12.8 | 9.0 | 61.5 | 86 | 40.4 | 37.7 | -5.9 | 84.4 |
| Orchard | 119 | 36.7 | 32.9 | -32.8 | -32.5 | -0.233 | 16.4 | -72.4 | 2.9 | 125 | 40.0 | 34.4 | -126.8 | 22.3 |
| Sloped tea farm | 44 | 99.1 | 79.2 | 6.3 | -35.4 | 1.013 | 100.0 | -122.9 | 240.9 | 46 | 107.9 | 85.0 | -129.6 | 294.5 |
| Tea farm | 78 | 24.3 | 19.2 | -16.5 | -15.8 | 0.033 | 17.9 | -66.7 | 47.6 | 82 | 51.5 | 26.9 | -71.5 | 304.3 |

Table 4.27 The accuracy of DTM using automated digital photogrammetry

| | 95% # of Points | 95% RMSE (cm) | 95% MAE (cm) | 95% Average (cm) | 95% Median (cm) | 95% Skew | 95% Std Dev (cm) | 95% Min (cm) | 95% Max (cm) | 100% # of Points | 100% RMSE (cm) | 100% MAE (cm) | 100% Min (cm) | 100% Max (cm) |
|---|---|---|---|---|---|---|---|---|---|---|---|---|---|---|
| Pavement | 109 | 27.0 | 21.4 | 17.6 | 16.6 | 0.254 | 20.6 | -26.6 | 69.4 | 104 | 28.6 | 22.6 | -32.4 | 76.3 |
| Landslide rock | 330 | 36.9 | 31.9 | 31.5 | 31.6 | 0.012 | 19.2 | -9.2 | 73.0 | 348 | 38.5 | 33.1 | -57.6 | 88.8 |

difference = elevation from photogrammetry — elevation of checkpoint

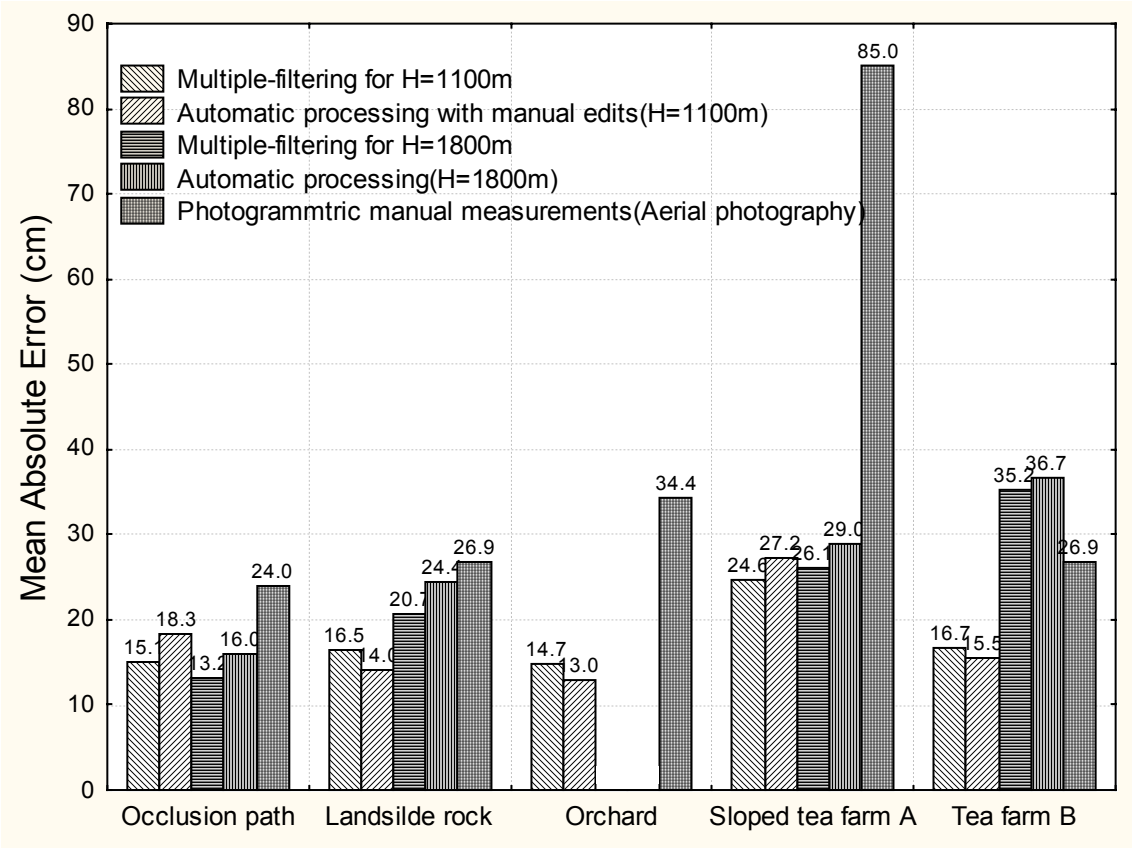


Figure 4.15. The comparisons of DTMs from LIDAR-derived vs. photogrammetry-derived.

# CHAPTER FIVE: CONCLUSIONS AND RECOMMENDATIONS

In this research, a collection of algorithms for automatically extracting DTMs was developed. Chapter 3 gives the framework of the proposed multiple-filtering processes.

The proposed method involves the combination of multiple developed filters. In the first stage, an adaptive elevation-difference filter is used to remove larger objects such as buildings. In the second stage, an adaptive steepest-descent filter removes medium objects such as dense trees. In the final stage, a directional steepest-descent filter removes small objects such as cars and single trees. Experimental results show that the proposed filtering procedures are capable of accurate and effective extraction of DTMs in the steep slopes, large variability areas, and urban areas. It is difficult to process with fixed parameters in areas of different topography. This study proposed that the best parameter of search radius for each object point could be determined automatically. The research also proposed adaptive techniques to overcome the influence of terrain relief on filtering performance. The proposed adaptive techniques achieved a better result (MAE of 22.2 cm) compared to traditional automated processing (MAE of 25.4 cm) in a random sample of 558 measurements with steep slopes and large variability.

This research developed a framework to evaluate the impact of terrain slope, terrain aspect, and land-cover type on elevation accuracy. Methods to extract land-cover types from LIDAR measurements were presented in order to characterize the vegetation information. They analyze LIDAR-derived tree height, canopy

volume, local roughness, and vegetation angle. These methods measure the same land-cover phenomenon for both datasets. In addition, the average distance from the ground checkpoints to the nearest LIDAR point may determine the point spacing of LIDAR ground returns. The results show that the lower flying altitude (H = 1100 m) gives better results (RMSE of 16.3 cm) than the higher altitude H = 1800 m (RMSE of 25.8 cm). The better dataset (H = 1100 m) was used to derive reference slope, aspect, and vegetation angle. Classes of different slopes, aspects, and vegetation angles were generated. For each class, the LIDAR-derived elevation was compared with in situ measurements to compute the elevation accuracy.

The results show that the LIDAR-derived elevation is almost correlated with terrain slope, vegetation angle, canopy volume, local roughness of point clouds, and mean distance to the nearest LIDAR point. There is an interaction effect between the point spacing of ground returns and vegetation angle. The results show a significant linear relationship between the elevation accuracy and the combination with point spacing of ground returns and vegetation angle (determination coefficient of regression $r^2 > 0.9$). The product of point spacing of ground returns and the tangent of the vegetation angle can determine the effect of land-cover class on elevation accuracy. Additionally, there is an interaction effect between the point spacing of ground returns and terrain slope. The elevation accuracy is significantly linearly correlated with the combination of point spacing of ground returns and slope ($r^2$ towards 0.9).

Finally, a significant effect of the terrain aspect was also found with the elevation error for H = 1800 m and for H = 1100 m without the cross-flight data (at the 0.05 significance level). On the other hand, there was no specific influence of terrain aspect on elevation error for dataset H = 1100 m with extra cross-flight data. As a consequence of the characteristics of sampling pattern and viewing direction,

dataset H = 1100 m with extra cross-flight data may reduce the effect of terrain aspect on the elevation accuracy.

The multiple-filtering processes require the selections of threshold parameters, and these have a great impact on the filtering results. The selection process is normally done by trial and error, but it can be improved and fully automated.

To process large datasets, a solution can be improved to divide the whole scene into multiple overlapping sections automatically so that each section is a scene with homogenous terrain and is processed individually. Then different parameters are used for different subsets and subsets can be improved to merge automatically.

# REFERENCES


Ackermanm, F., 1999. Airborne laser scanning - present status and future expectations. *ISPRS Journal of Photogrammetry and Remote Sensing*, 54: 64–67.

Adams, J. C., and J. H. Chandler, 2002. Evaluation of LIDAR and medium scale photogrammetry for detecting soft-cliff coastal change. *Photogrammetric Record*, 17(99):405–418.

Ahokas, E., H. Kaartinen, and J. Hyyppä, 2003. A quality assessment of airborne laser scanner data. *International Archives of Photogrammetry and Remote Sensing*, part 3/W13, 34:7p.

Axelsson, P., 1999. Processing of laser scanner data — algorithms and applications. *ISPRS Journal of Photogrammetry and Remote Sensing*, 54: 138–147.

Axelsson, P., 2000. DEM generation from laser scanner data using adaptive TIN models. *International Archives of Photogrammetry and Remote Sensing*, part B4, 33:110–117.

Baltsavias, E. P., 1999a. Airborne laser scanning: existing systems and firms and other resources. *ISPRS Journal of Photogrammetry and Remote Sensing*, 54: 164-198.

Baltsavias, E. P., 1999b. Airborne laser scanning: basic relations and formulas. *ISPRS Journal of Photogrammetry and Remote Sensing*, 54: 199–214.

Baltsavias, E. P., 1999c. A comparison between photogrammetry and laser scanning. *ISPRS Journal of Photogrammetry and Remote Sensing*, 54: 83–94.

Behan, A., 2000. On the matching accuracy of rasterized scanning laser altimeter data. *International Archives of Photogrammetry and Remote Sensing*, part B2, 33:75–82.

Berenson, M. L., D. M. Levine, and T. C. Krehbiel, 2004. *Basic business statistics: concepts and applications*. 9th edition, Pearson Education, 831 p.

Brenner, C., 2000. Toward fully automatic generation of city models, *International Archives of Photogrammetry and Remote Sensing*, part B3, 33:85–92.

Briese, C., N. Pfeifer, and P. Dorninger, 2002. Applications of the robust interpolation for DTM determination. *International Archives of Photogrammetry and Remote Sensing*, part 3A, 34:55–61.

Brovelli, M. A., M. Cannata, and U. M. Longoni, 2002. Managing and processing LIDAR data within GRASS. *Proceedings of the Open source GIS - GRASS users conference*, 11-13 September, Trento, Italy, 29p.

Brovelli, M. A., M. Cannata, and U. M. Longoni, 2004. LIDAR Data Filtering and DTM Interpolation Within GRASS. *Transactions in GIS*, 8(2):155–174.

Burman, H., 2000. Adjustment of laserscanner data for correction of orientation errors. *International Archives of Photogrammetry and Remote Sensing*, part B3, 33:125–132.

Crombaghs, M., R. Brügelmann, and E. de Min, 2000. On the adjustment of overlapping strips of laseraltimeter heigh data, *International Archives of Photogrammetry and Remote Sensing*, part 3A, 33:230–237.

Crombaghs, M., S. O. Elberink, R. Brügelmann, and E. de Min, 2002. Assessing height precision of laser altimetry DEMs. *International Archives of Photogrammetry and Remote Sensing*, part 3A, 34:85–90.

Elmqvist, M., 2001. Ground surface estimation from airborne laser scanner data using active shape models, *Proceedings of the OEEPE Workshop on Airborne Laserscanning and Interferometric SAR for Detailed Digital Elevation Models* (K. Torlegard nad J. Nelson, editors), Stockholm, Sweden, 73–80.

Flood, M., 2001. Laser altimetry: from science to commercial LIDAR mapping.

*Photogrammetric Engineering & Remote Sensing*. 67(11):1209–1218.

Gomes Pereira, L. M, and L. L. F. Janssen, 1999. Suitability of laser data for DTM generation: a case study in the context of road planning and design. *ISPRS Journal of Photogrammetry and Remote Sensing*, 54:244–253.

Haala, N., C. Brenner, and K. H. Anders, 1998. 3-D urban GIS from laser altimeter and 2-D map data. *International Archives of Photogrammetry and Remote Sensing*, 32:339–346.

Haala, N., and C. Brenner, 1999. Extraction of buildings and trees in urban environments. *ISPRS Journal of Photogrammetry and Remote Sensing*, 54: 130-137.

Hodgson, M. E., J. R. Jensen, L. Schmidt, S. Schill, and B. Davis, 2003. An evaluation of LIDAR- and IFSAR-derived digital elevation models in leaf-on conditions with USGS Level 1 and Level 2 DEMs. *Remote Sensing of Environment*, 84:295–308.

Hodgson, M. E., and P. Bresnahan, 2004. Accuracy of airborne Lidar-derived elevation: empirical assessment and error budget. *Photogrammetric Engineering & Remote Sensing*. 70(3):331–339.

Hu, Y., 2003. Automated extraction of digital terrain models, roads and buildings using airborne LIDAR data. PhD dissertation, Department of Geomatics Engineering, University of Calgary, 206 p.

Huising, E. J., and L. M. Gomes Pereira, 1998. Errors and accuracy estimates of laser data acquired by various laser scanning systems for topographic applications. *ISPRS Journal of Photogrammetry and Remote Sensing*, 53:245–261.

Hyyppä, J., O. Kelle, M. Lehikoinen, and M. Inkinen, 2001. A segmentation-based method to retrieve stem volume estimates from 3-D tree height models produced by laser scanners. *IEEE Trans. on Geoscience and Remote Sensing.*

39(5):969–975.

Kilian, J., N. Haala, and M. Englich, 1996. Capturing and vealuation of airborne laser scanner data, *International Archives of Photogrammetry and Remote Sensing*, part B3, 32:383–388.

Kraus, K., and N. Pfeifer, 1998. Determination of terrain models in wooded areas with airborne laser scanner data. *ISPRS Journal of Photogrammetry and Remote Sensing*, 53:193–203.

Kraus, K., and N. Pfeifer, 2001. Advanced DTM generation from lidar data. *International Archives of Photogrammetry and Remote Sensing*, part 3/W4, 34:23–30.

Latypov, D., 2002. Estimating relative lidar accuracy information from overlapping flight lines, *ISPRS Journal of Photogrammetry and Remote Sensing*, 56:236–245.

Lee, H. S., and N. H. Younan, 2003. DTM extraction of LIDAR returns via adaptive processing. *IEEE Trans. on Geoscience and Remote Sensing*. 41(9):2063–2069.

Liu, J.K., 2005. On the systematic error handling of airborne laser scanning: from system calibration to data Adjustment. PhD dissertation, Department of Civil Engineering, National Chiao Tung University, Taiwan, R.O.C., 115 p.

Lloyd, C. D., and P. M. Atkinson, 2002. Deriving DSMs from LIDAR data with kriging. *International Journal of Remote Sensing*. 23(12):2519–2524.

Lohmann, P., A. Koch, and M. Schaeffer, 2000. Approaches to the filtering of laser scanner data. *International Archives of Photogrammetry and Remote Sensing*, part B3, 33:540–547.

Maas, H.-G., and G. Vosselman, 1999. Two algorithms for extracting building models from raw altimetry data. *ISPRS Journal of Photogrammetry and Remote Sensing*, 54: 153-63.

Maas, H.-G., 2002. Methods for measuring height and planimetry discrepancies in

airborne laserscanner data. *Photogrammetric Engineering & Remote Sensing*. 68(9):933–940.

Maune, D. (editor), 2001. *Digital elevation model technologies and applications: The DEM users manual*. Bethesda, Maryland, American Society for Photogrammetry and Remote Sensing. 539 p.

Means, J.E., S. A. Acker, B. J. Fitt, M. Renslow, L. Emerson, and C. J. Hendrix, 2000. Predicting forest stand characteristics with airborne scanning Lidar. *Photogrammetric Engineering & Remote Sensing*. 66(11):1367–1371.

Næsset, E., 1997a. Determination of mean tree height of forest stands using airborne laser scanner data. *ISPRS Journal of Photogrammetry and Remote Sensing*, 52(2):49–56.

Næsset, E., 1997b. Estimating timber volume of forest stands using airborne laser scanner data. *Remote Sensing of Environment*, 61(2):246–253.

Peng, M. H., and T. Y. Shih, 2002. A quality assurance approach for land subsidence. *Survey Review*, 36(286):568–581.

Peng, M. H., and T. Y. Shih, Error assessment in LIDAR-derived TIN dataset. *Photogrammetric Engineering & Remote Sensing*. (accepted).

Petzold, B., P. Reiss, and W. Stössel, 1999. Laser scanning — surveying and mapping agencies are using a new technique for the derivation of digital terrain models. *ISPRS Journal of Photogrammetry and Remote Sensing*, 54:95–104.

Pfeifer, N., T. Reiter, C. Briese, and W. Rieger, 1999. Interpolation of high quality ground models from laser scanner data in forested areas. *International Archives of Photogrammetry and Remote Sensing*, part 3/W14, 32:31–36.

Pfeifer, N., P. Stadler, and C. Briese, 2001. Derivation of digital terrain models in the SCOP++ environment. *Proceedings of the OEEPE Workshop on Airborne Laserscanning and Interferometric SAR for Detailed Digital Elevation Models* (K.

Torlegard nad J. Nelson, editors), Stockholm, Sweden, 49–61.

Raber, G. T., J. R. Jensen, S. R. Schill, and K. Schuckman, 2002. Creation of digital terrain models using an adaptive lidar vegetation point removal process. *Photogrammetric Engineering & Remote Sensing*, 68(12):1307–1315.

Sithole, G., 2001. Filtering of laser altimetry data using a slope adaptive filter. *International Archives of Photogrammetry and Remote Sensing*, part 3/W4, 34:203–210.

Sithole, G., and G. Vosselman, 2003. Report: ISPRS Comparision of filters. *Proceedings of ISPRS Commission III/WG3 3D Reconstruction from Airborne laser Scanner and InSAR Data*, URL: http://www.geo.tudelft.nl/frs/isprs/filtertest/, (last date accessed: 2 April 2005).

Sithole, G., and G. Vosselman, 2004. Experimental comparison of filter algorithms for bare-Earth extraction airborne laser scanning point clouds. *ISPRS Journal of Photogrammetry and Remote Sensing*, 59:85–101.

Smith, S. L., D. A. Holland, and P. A. Longley, 2004. The importance of understanding error in LIDAR digital elevation models. *Proceedings of the XX$^{th}$ ISPRS Congress*, 12-23 July, Istanbul, Turkey, part B4, 34:996–1001.

Sohn, G., and I. Dowman, 2002. Terrain surface reconstruction by the use of tetrahedron model with the MDL criterion. *International Archives of Photogrammetry and Remote Sensing*, part 3A, 34:336–344.

Vosselman, G., 2000. Slope based filtering of laser altimetry data. *International Archives of Photogrammetry and Remote Sensing*, part B3, 33:935–942.

Vosselman, G., and S. Dijkman, 2001. 3D building model reconstruction from point clouds and ground plans. *International Archives of Photogrammetry and Remote Sensing*, part 3/W4, 34:37–44.

Vosselman, G., and H.-G. Maas, 2001. Adjustment and filtering of raw laser altimetry

data. *Proceedings of the OEEPE Workshop on Airborne Laserscanning and Interferometric SAR for Detailed Digital Elevation Models* (K. Torlegard and J. Nelson, editors), Stockholm, Sweden, 62–72.

Wack, R., and A. Wimmer, 2002. Digital terrain models from airborne laser scanner data — a grid based approach. *International Archives of Photogrammetry and Remote Sensing*, part 3B, 34:293–296.

Wehr, A., and U. Lohr, , 1999. Airborne laser scanning—an introduction and overview. *ISPRS Journal of Photogrammetry and Remote Sensing*, 54:68–82.

Yokoyama, R., M. Shirasawa, and R. J. Pike, 2002. Visualizing topography by openness: a new application of image processing to digital elevation models. *Photogrammetric Engineering & Remote Sensing*, 68(3):257–265.

Zhang, K., S. C. Chen, D. Whitman, M. L. Shyu, J. Yan, and C. Zhang, 2003. A progressive morphological filter for removing nonground measurements from airborne LIDAR data. *IEEE Trans. on Geoscience and Remote Sensing.* 41(4):872–882.

Zhang, K. and D. Whitman, 2005. Comparison of three algorithms for filtering airborne LIDAR data. *Photogrammetric Engineering & Remote Sensing*, 71(3):313–324.